# FLUID-SHALE-PROPPANT INTERACTIONS AND THE DEGRADATION OF HYDRAULIC FRACTURE CONDUCTIVITY IN THE NIOBRARA FORMATION

by

Jessica G. Iriarte

A thesis submitted to the Faculty and the Board of Trustees of the Colorado School of Mines in partial fulfillment of the requirements for the degree of Master Of Science (Petroleum Engineering).

Golden, Colorado

Date _____

Signed: _____
Jessica G. Iriarte

Signed: _____
Dr. Azra N. Tutuncu
Thesis Advisor

Golden, Colorado

Date _____

Signed: _____
Dr. Erdal Ozkan
Professor and Department Head
Department of Petroleum Engineering

# ABSTRACT

Conductivity is a major design goal in hydraulic fractures since it is a measurement of the fracture's flow capacity. Placing the proper proppant type with the right fluid type is critical due to the different interactions taking place within the formation and proppant agent. However, fluid and proppant selection is usually based on economical and practical considerations. The majority of the research studies investigate the rock-fluid interactions related to clays, even though most shale plays don't have high clay content. This study aims to understand the fluid, rock, and proppant chemical and mechanical interactions taking place in the Niobrara shale, a calcium carbonate rich formation, during hydraulic fracturing treatments. For this, coupled fluid chemical interactions, static and dynamic mechanical properties, and fracture conductivity of the Niobrara Formation were investigated under reservoir stress and atmospheric conditions.

The Niobrara samples used in this study were characterized using X-ray Diffraction (XRD), and X-ray Fluorescence (XRF), Field-Emission Scanning Electron Microscopy (FE-SEM), and Helical Computed Tomography Scan (CT-Scan). Three sets of experiments were conducted: (1) fluid chemical interactions with crushed rock and proppant, (2) geomechanical variations in intact core samples, and (3) chemical and mechanical monitoring under triaxial stress conditions. By studying these elements both individually and in combination, it is possible to understand the impact of fluid selection on geochemical and geomechanical changes in the rock. For the first set of experiments the associated changes in the composition of the solution were monitored as a function of time. For the second one, the variations of dynamic and static mechanical properties were examined in intact core plugs before and after they were saturated with different fluids. The last set of experiments was performed on a fractured and propped core under triaxial stress conditions. The special design implemented allows for the simultaneous acquisition of coupled stress, strain, ultrasonic compressional

and shear wave velocities, flow data and fluid.

The results from this study show that each fluid interacts with the elements present in the rock in a different way. Some fluids dilute elements related to the strength of the rock, while others dilute elements related to undesired precipitation or organic matter. Comparison of dynamic and static elastic moduli and fluid chemistry data pre- and post- treatment indicate that there is a correlation between the formation softening and the chemical interactions taking place between the fluids used in this study and the Niobrara Formation. Moreover, conductivity damage effects vary not only with mineralogy of the rock, but also with the mineral distribution and where the fracture is located within the formation.

Effective well performance in tight reservoirs can be accomplished through the integration of multidisciplinary data collection. This study integrates detailed geomechanical and geochemical analyses to capture the associated changes in the rock, proppant, and fluid when they interact with each other. A correlation between the mineralogy and mechanical properties of the core is introduced and a method to improve fluid selection in hydraulic fracturing operations is proposed.

TABLE OF CONTENTS

LIST OF FIGURES

LIST OF TABLES

# LIST OF SYMBOLS

Aluminum . . . . . $Al^{3+}$

Axial force . . . . . $F_a$

Axial stress applied . . . . . $\sigma_a$

Barium . . . . . $Ba^{2+}$

Biot's coefficient . . . . . $\alpha$

Calcium . . . . . $Ca^{2+}$

Calcium chloride . . . . . $CaCl_2$

Calcium sulfate . . . . . $CaSO_4$

Centipoise . . . . . cp

Change in concentration . . . . . $C_{change}$

Chloride . . . . . $Cl^-$

Closure pressure . . . . . $P_c$

Compressional wave velocity . . . . . $V_p$

Copper . . . . . Cu

Cross-sectional area of the piston . . . . . $A_s$

Cubic centimeter per minute . . . . . $cm^3/min$

Darcy . . . . . D

Density . . . . . $\rho$

Effective stress . . . . . $\sigma_{v,eff}(\sigma_e)$

Ferrous . . . . . $Fe^{2+}$

Final concentration . . . . . $C_{after}$

Flow area . . . . . A

Fracture conductivity . . . . . $C_f$

Fracture permeability . . . . . $k_f$

Fracture width . . . . . $w_f$

Forchheimer term . . . . . $\beta$

Height . . . . . h

Hydron . . . . . $H^+$

Initial concentration . . . . . $C_{initial}$

Inlet pore pressure . . . . . $P_{p\text{-}in}$

Kilometer per second . . . . . km/s

KiloNewton . . . . . kN

Length . . . . . dl (l)

Magnesium . . . . . $Mg^{2+}$

Magnesium chloride . . . . . $MgCl_2$

MilliDarcy . . . . . mD

Milliliter per minute . . . . . mm/min

Minimum horizontal stress . . . . . $\sigma_{h,min}$

Maximum horizontal stress . . . . . $\sigma_{H,max}$

Minimum horizontal stress . . . . . $\sigma_{h,eff}$

Nickel . . . . . Ni

Outlet pore pressure . . . . . $P_{p\text{-}out}$

Overburden stress . . . . . $\sigma_v$

Parts per billion . . . . . ppb

Parts per million . . . . . ppm

Percentage by weight . . . . . %wt.

Permeability . . . . . k

Poisson's ratio . . . . . $\nu$

Potassium . . . . . $K^+$

Potassium chloride . . . . . KCl

Pounds per square inch . . . . . psi

Pounds per square inch gauge . . . . . psig

Pore pressure . . . . . $P_p$

Pressure gradient . . . . . dp (p)

Pump axial pressure . . . . . $P_a$

Pump confining pressure . . . . . $P_c$

Pyrite . . . . . $FeS_2$

Rate . . . . . q

Regional tectonic strain . . . . . E

Regional tectonic stress . . . . . $\sigma_t$

Shear wave velocity . . . . . $V_s$

Silicon . . . . . $Si^+$

Sodium . . . . . $Na^+$

Sodium chloride . . . . . NaCl

Strain . . . . . $\varepsilon$

Stress . . . . . $\sigma$

Strontium . . . . . $Sr^{2+}$

Sulfate . . . . . $SO_4^{-2}$

Surface area of the larger section of the piston . . . . . $A_c$

Viscosity . . . . . $\mu$

Water . . . . . $H_2O$

Young's modulus . . . . . E

# LIST OF ABBREVIATIONS

| | |
|---|---|
| Backscattered Electron | BSE |
| Computed Tomography Scan | CT Scan |
| Coupled-Plasma-Atomic Emission Spectrometer | ICP-AES |
| Denver-Julesberg | DJ |
| Differential Pressure Transducers | DPT |
| Distilled Water | DI |
| Energy-dispersive X-ray spectroscopy | EDS |
| Field-Emission Scanning Electron Microscopy | FE-SEM |
| High Strength Proppants | HSP |
| Intermediate Strength Proppants | ISP |
| International Organization for Standardization | ISO |
| Light Weight Ceramics | LWC |
| Linear Variable Differential Transformer | LVDT |
| Resin Coated Proppant | RCP |
| Resin Coated Sand | RCS |
| Secondary Electron | SE |
| Total Organic Content | TOC |
| X-ray Diffraction | XRD |
| X-ray Fluorescence | XRF |

# ACKNOWLEDGMENTS

I would like to express my deepest gratitude to my advisor Dr. Azra Tutuncu for her dedicated guidance and continuous support in every step during my masters. I would also like to thank my committee members Dr. Jennifer Miskimins and Dr. Hazim Abass for always having an open door and offering me their insight and knowledge throughout this journey.

Dr. Daisuke Katsuki was essential to the success of this work. Thanks for teaching me, helping me and for being such a dedicated mentor for my experimental research. I truly appreciate all your patience and dedication to share your wisdom and to answer my never-ending questions. I am grateful to the Unconventional Natural Gas and Oil Institute (UNGI) sponsors for funding this study. Special thanks to Dr. Ali I. Mese for donating the triaxial cell to our geomechanics laboratory.

Thanks to all my UNGI mates, especially to my lab partners Dina Hegazy, Bekdar Baizahov and Wale Adekunle. The long working days in the lab would not have been the same without you. I am immeasurably thankful for all the work and modifications to the cell Dina did before me and for her incredible supportive friendship. I will not forget those late nights working in the lab, listening to some blues and having our usual deep and very political conversations.

I am surely grateful to have Sepideh, my friend and roommate, for her unconditional support throughout my tough times during this journey. I am also grateful for having Angela Dang and the Venezuelan and Colombian community as friends.

I very much appreciate the various help I received from Joe Chen, Cesar Mapeli, Dr. James Ranville, Dr. Katharina Paff and Dr. Manika Prasad. I would also like to thank Denise Winn-Bower, for extending her hand and helping me even before I got here. Thanks also to the Well Data Labs team, for being so flexible and understanding to my schedule.

Finally, I would like to thank my family for always supporting me and motivating me to embrace new endeavors. Also, thanks to the add-on family members Jorge, Pocha, and Gabriel for always encouraging me to stay true to myself and to pursue my career goals.

For my parents Graciela and Rogelio for their unconditional love and support.

For my sister Erica for being an inspiration, and for my brother Matias for showing me to embrace new adventures.

For Pocha and Gabriel, for their incredible encouragement.

# CHAPTER 1

# INTRODUCTION

Unconventional reservoirs are characterized by their very low permeability. Therefore, increasing the formation face contact area with a highly conductive path is essential to increase their production capacity. For this reason, hydraulic fracturing has become an essential procedure for any commercial hydrocarbons production in unconventional resources.

The conductivity of a fracture is determined in the lab by measuring the pressure drop of a fluid through a uniformly distributed proppant bed in a core with fixed length and height. Conductivity is a major design goal in hydraulic fractures since it is a measurement of the capacity of a fracture to flow fluid. Therefore, placing the proper proppant type with the right fluid is critical. However, the fluid and proppant selection is typically based on economical and practical considerations.

The impact of water and solute through the reservoir shale has been one of the key research areas studied at the Unconventional Natural Gas and Oil Institute (UNGI) to determine the similarities and differences in mechanical, acoustic and transport behavior in seal and reservoir shales. In this research study, fracture conductivity, mechanical and acoustic properties of Niobrara shale under reservoir stress conditions have been investigated. The measurements have been conducted coupling geomechanics and fluid chemistry pre- and post- treatment after the Niobrara core samples were exposed to various fluid compositions.

## 1.1 Motivation of Study

As hydraulic fracturing challenges continue to evolve in the current industry setting, treatments are required to be more efficient. Choosing the right fluid and proppant type for a particular job can be intricate, considering the different reactions taking place in the reservoir. However, when designing hydraulic fracturing treatments, proppant and fluid selection is based on economical and practical considerations.

The majority of the research studies investigate the rock-fluid interactions related to clays, even though most shale plays are fine-grained clastics and not necessarily shales (Britt and Schoeffler 2009). In fact, the Niobrara Formation, investigated in this study, is rich in calcium carbonate. Its low porosity and permeability make this play classified as a tight and unconventional reservoir. Therefore, fluid selection for this type of reservoir should be different than clay-rich or quartz-rich formations.

A variety of experimental studies conducted to determine proppant performance by various researchers reveals damage to conductivity and dissolution-mediated compaction. These studies lead to the conclusion that different geochemical reactions are taking place within the formation and the proppant when they are subjected to fracturing fluid saturation and high mechanical stress (Alramahi and Sundberg 2012; Freeman et al. 2009; Ghosh et al. 2014; LaFollette and Carman 2011; Lee et al. 2009; Osholake et al. 2011; Raysoni and Weaver 2012; Reinicke 2010; Weaver et al. 2007; Zhang et al. 2014). This research study investigates the geomechanical and geochemical changes related to rock-fluid-proppant interactions in the Niobrara Formation. By studying these elements both individually and in combination, it is possible to understand the impact of fluid selection on the degradation of the fracture conductivity. A correlation between the mineralogy and mechanical properties of the core is introduced and a method to improve fluid selection in hydraulic fracturing operations is proposed.

## 1.2 Objectives

The primary objective of this study is to evaluate the degradation of the fracture conductivity due to geochemical and geomechanical changes related to rock-fluid-proppant interactions in the Niobrara Formation. The specific objectives can be summarized as follows:

- Evaluate the chemical variations taking place when fluids interact with rock and proppant.

- Evaluate the effect of fluid-rock interactions on the geomechanical properties of the Niobrara Formation.
- Monitor the fluid, rock, and proppant chemical and mechanical interactions under triaxial stress conditions.
- Find a relationship between the chemical and mechanical changes taking place in the rock and their effect on fracture conductivity in the Niobrara shale samples.

### 1.3 Niobrara Formation Overview

The Niobrara shale is an organic-rich source rock in the Denver-Julesberg (DJ) basin. It is an Upper Cretaceous formation in the Rockies region that consists of a combination of chalk and marl layers, as presented in Figure 1.1. It is divided into two units, the Fort Hays Limestone Member and the Smoky Hill Member. The Fort Hays Limestone is characterized by a small, sandy section at the base mainly composed of carbonate sediments (Finn and Johnson 2005). The Smoky Hill Member has been divided into discrete intervals based on variability in the chalk and shale content (Finn and Johnson 2005). The organic-rich marls within the Niobrara Formation act as source rocks, while the chalks and clay-rich limestones act as the reservoir formations (ElGhonimy 2015; Finn and Johnson 2005). Therefore, this formation represents a self-sourced petroleum system.

This formation is mainly composed of calcium carbonate. Porosity in the chalks and clay-rich limestones is typically less than 10% and permeability is typically around 0.0001-0.0007 mD, which classifies it as tight and unconventional. Since the Niobrara Formation was deposited, the ground has been uplifted, depressed, uplifted again, and tilted resulting in fractures, faults, and folding (Matthews 2011). Production in the Niobrara relies on the presence of these natural fractures that are mineralized and contain calcite, quartz, or gypsum (Ritzma 1955; Vincelette and Foster 1992).

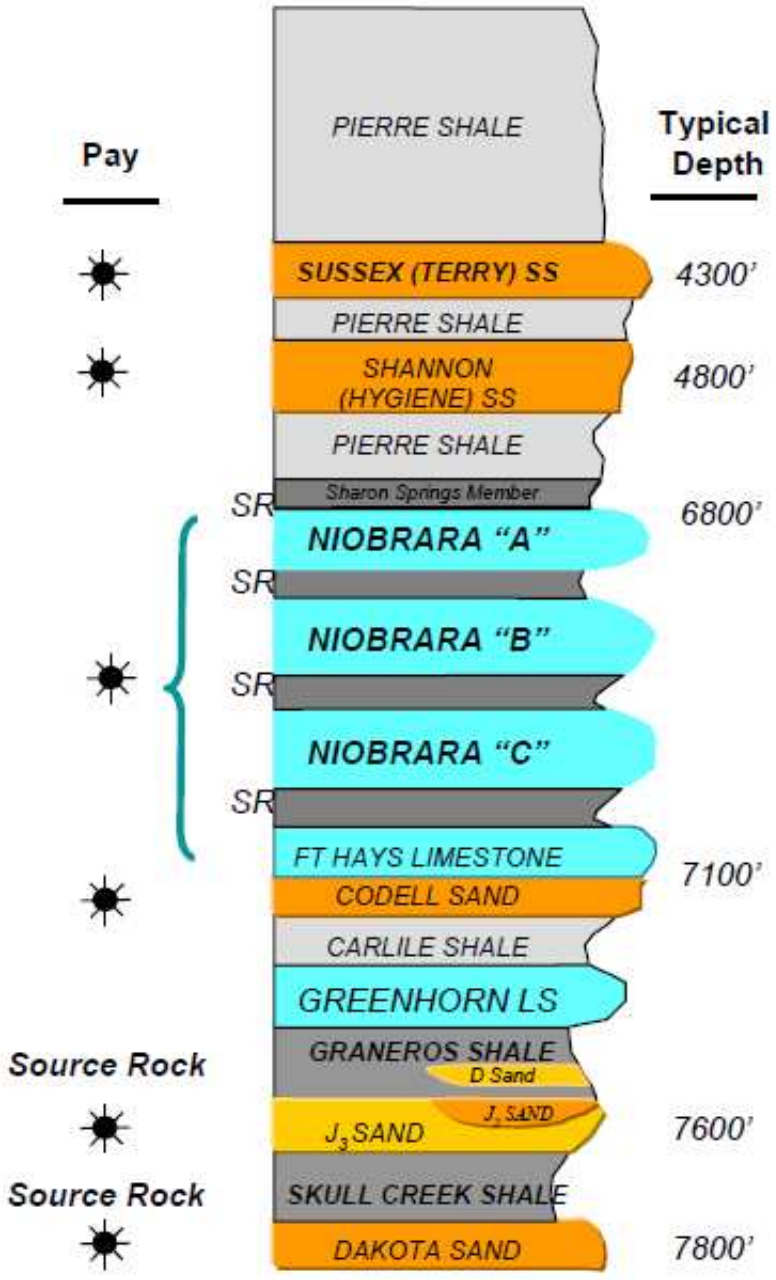


Figure 1.1: Stratigraphic column for the Niobrara shale (Sonnenberg 2012)

### 1.3.1 Field Area Location

The cores used in this study are Niobrara outcrops taken from the CEMEX cement quarry located along the Colorado Front Range between Boulder and Lyons. The field sites are approximately five to ten miles north of Boulder Colorado on the east side of the Southern Rockies as shown in Figure 1.2 (Collin 2012).

### 1.3.2 The Denver Basin

The Denver Basin, also called Denver-Julesburg Basin (or DJ Basin), is one of the largest basins in the Rocky Mountain region. This Basin has historically been the most significant producer, followed by the Sand Wash Basin, Piceance Basin, Douglas Creek Arch (not shown), and North Park Basin (Figure 1.3) (Matthews 2011). Within the basin, a complex tectonic history resulted in NE trending wrench faults and extensive normal faulting, which has also resulted in folding and displacing some of the stratigraphic units within the basin (ElGhonimy 2015).

### 1.3.3 Niobrara Outcrops Description

The Niobrara outcrops taken from the Niobrara "B", which is the most actively produced layer in the unit. The outcrops are mainly composed of calcite, quartz, mica/illite, and dolomite. Collin (2012) described the source rocks of the Niobrara Formation at the CEMEX Limestone Quarry as thermally mature Type II kerogens that are in the peak to post peak oil generation window and are charging the reservoirs of the chalk units. The author also reported that the thermal maturity and total organic content (TOC) have a direct relationship with clay content and an inverse relationship with the amount of calcite present within the formation, implying that the higher percentage of calcite in the formation indicates the lower percentage of TOC wt. %.

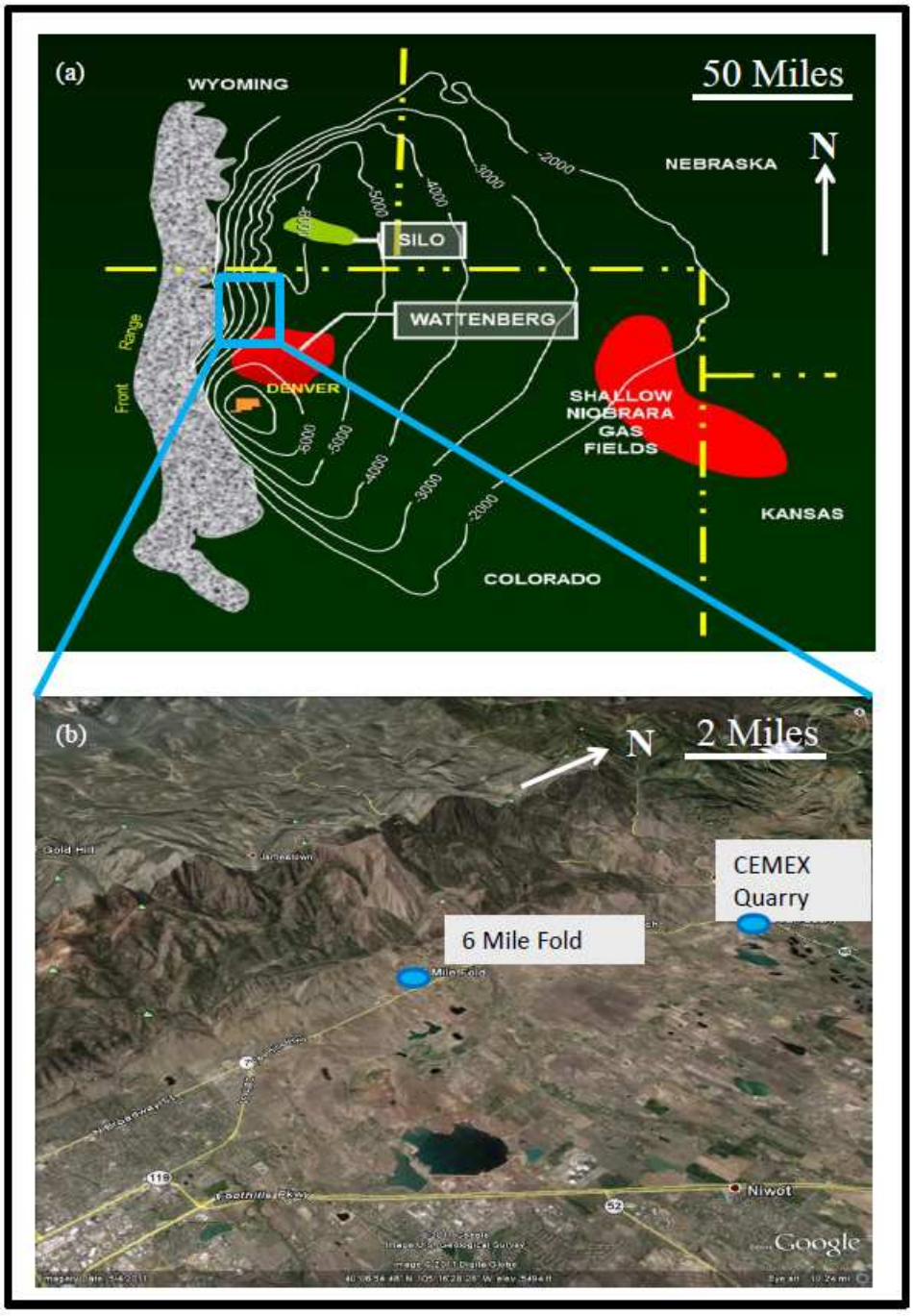


Figure 1.2: Location of study area: (a) Denver Basin regional map with locations of major fields; (b) close-up of outcrop location along the Colorado Front Range (Collin 2012).


Figure 1.3: Basins (dark blue) with known shale oil potential overlaid on paleogeographic map of Late Cretaceous (Matthews 2011).

# CHAPTER 2
# LITERATURE REVIEW

In this chapter, a review of the hydraulic fracturing fundamentals, geomechanics, rock-fluid interactions and prior experimental studies are introduced.

## 2.1 Hydraulic Fracturing

Hydraulic fracturing has become an essential processes for any commercial hydrocarbon production in unconventional resources, due to their low permeability. During the last decade of gas shale development, projected recovery of shale gas-in-place has increased from about 2% to estimates of about 50%; mainly through the development and adaptation of technologies to fit shale gas developments (King 2010).

A fracture generated during a hydraulic fracturing treatment is a fluid conduit and has a conductivity, which is responsible for the difference in the pre- and post- fracturing well productivity (Weaver et al. 2007). During this treatment, fluids are injected into the well at high pressures in order to overcome the breakdown and propagation pressure causing tensile and shear failure of the surrounding rock (Hyne 2012). The highly conductive path would close when the pressure is released, unless a proppant agent (generally sand or ceramic proppant) is placed in the channel to support the fracture walls and keep it open. Fracture performance depends on the propped fracture geometry and fracture conductivity.

### 2.1.1 Hydraulic Fracturing Geomechanics

Fundamentals of applied geomechanics are essential to understanding the respond of rocks to a hydraulic fracturing treatment. Geomechanics governs fracture initiation, orientation, and growth in any particular reservoir.

#### 2.1.1.1 Principal Stresses

Stress is defined as the external force applied to a defined cross-sectional area. Application of stress will usually result in deformation of the material or strain. The stress state in a reservoir and the applied load will dominate the initiation and propagation of a hydraulic fracture. The principal stresses are three unequal principal in-situ compressive stresses, mutually perpendicular (Figure 2.1). Fractures grow perpendicular to the minimum in-situ principal stress.

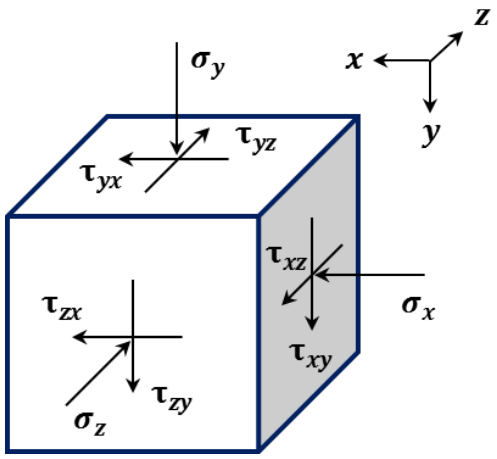


Figure 2.1: Stress tensor in a Cartesian coordinate system.

Zoback (2010) defines stress as a tensor which describes the density of forces acting on all surfaces passing through a given point as shown in Equation 2.1. Normal stress acts perpendicular to a specific surface, while shear stress acts parallel to it. The stress acting on each plane of the body will have one normal and two shear components producing a body that has three normal stresses and six shear stresses as shown in Equation 2.2.

$$S = \begin{bmatrix} s_{11} & s_{12} & s_{13} \\ s_{21} & s_{22} & s_{23} \\ s_{31} & s_{32} & s_{33} \end{bmatrix} \tag{2.1}$$

$$S = \begin{bmatrix} \sigma_{xx} & \tau_{xy} & \tau_{xz} \\ \tau_{yx} & \sigma_{yy} & \tau_{yz} \\ \tau_{zx} & s_{32} & \sigma_{zz} \end{bmatrix} \tag{2.2}$$

The subscripts refer to the direction of the force. The first subscript identifies the axis normal to the actual surface, while the second one identifies the direction of the force (Fjar et al. 2008). Then, the principal stress values are defined by the diagonal of the stress tensor as shown in Equation 2.3.

$$S = \begin{bmatrix} \sigma_{xx} & 0 & 0 \\ 0 & \sigma_{yy} & 0 \\ 0 & 0 & \sigma_{zz} \end{bmatrix} \tag{2.3}$$

The overburden stress is the vertical stress defined by the weight of the reservoir rock overlaying above the formation. Typically, a pressure gradient of 1.0 - 1.1 psi/ft is used as overburden stress gradient. The horizontal stresses are primarily a result of the overburden stress, the reservoir pressure, and the tectonic forces. They are known as minimum horizontal stress ($\sigma_{h,min}$) and maximum horizontal stress ($\sigma_{H,max}$). These total stresses are the externally applied load carried by the pore fluid and the rock matrix. Terzaghi's effective stress law, presented in Equation 2.4, defines the applied load carried by the rock matrix only.

$$\sigma_{v,eff} = \sigma_v - \alpha p_p \tag{2.4}$$

In isotropic stress conditions, the minimum horizontal stress and effective overburden stress relationship is shown in Equation 2.5.

$$\sigma_{h,eff} = \frac{v}{1-v}\sigma_{v,eff} \tag{2.5}$$

In-situ stresses control the fracture initiation, orientation, and propagation in any reservoir formation. Hydraulic fractures open in the direction perpendicular to the least principal stress and propagate in the direction of the greatest principal stress. To open a fracture, the applied pressure to the rock must be greater than the closure pressure ($p_c$), as presented in Equation 2.6. The difference between the applied pressure and the closure pressure is known as net pressure ($p_{net}$).

$$p_c = \frac{v}{1-v}(\sigma_v - \alpha_v p_p) + \alpha_h p_p + E\varepsilon + \sigma_t \tag{2.6}$$

#### 2.1.1.2 Rock Deformation and Failure Characteristics

Each formation has a unique lithology and mechanical properties; therefore, they react differently to the applied forces. When shales and sands are subjected to the same overburden stress they react differently. In any case, when the rock is subjected to stresses beyond its strength, it will fail. To understand the failure characteristics of any formation under various normal and shear stress state, one of the industry preferred methodologies is to conduct Mohr-Coulomb graphical analysis to determine a failure envelope.

Mohr's circles are used to map the values of normal and shear stresses at failure (Davis et al. 1996), failure being the loss of cohesion of a material when the differential stress ($s_1 - s_3$) exceeds a critical value that varies with different types of formations. The failure is expected to occur when the Mohr's circle "touches" the failure envelope as shown in Figure 2.2.

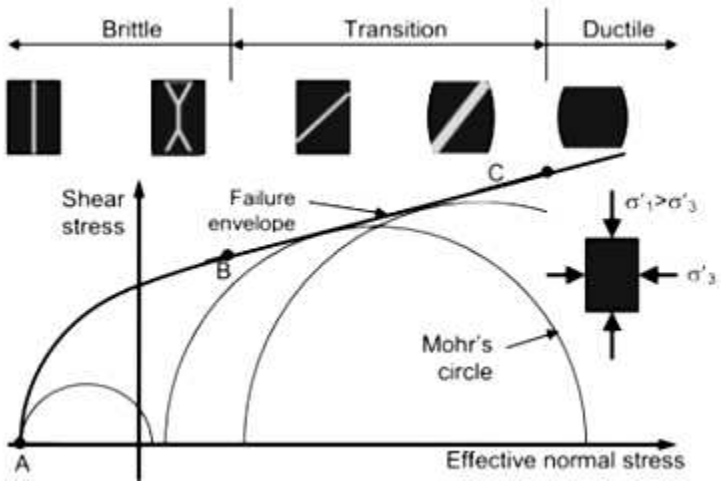


Figure 2.2: Graphical representation of Mohr's circle with the illustration of the typical stress dependency of shearing response of rock materials (Katsuki et al. 2014).

Rocks break either in tension or compression. The geometry of the created crack depends upon the surrounding medium and the applied loads. The fundamental modes of loading that can be defined for a crack are shown in Figure 2.33. Mode I or opening mode, corresponds to a normal tension in front of the crack, Mode II or sliding mode, associated with a transverse shear, and Mode III or tearing mode for a longitudinal shear.

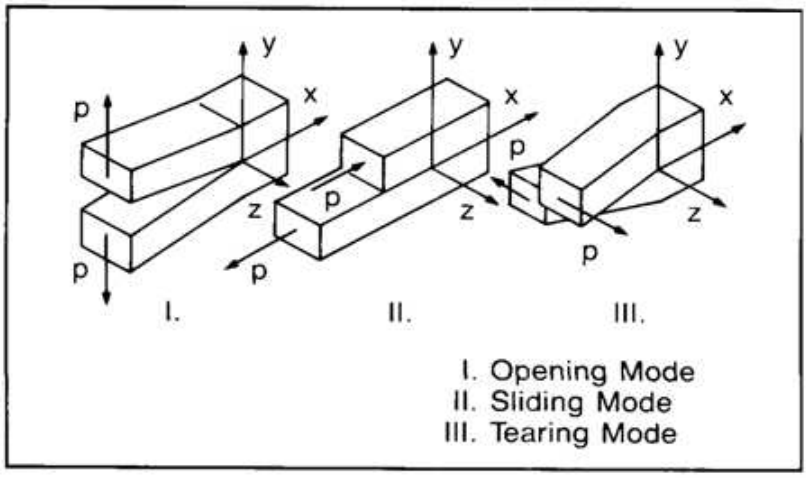


Figure 2.3: Fundamental modes of loading that can be defined for a crack (Ewalds and Wanhill 1984).

#### 2.1.1.3 Fluid flow in Porous Media

The basic physics of fluid flow can be described by the equations of mass and momentum conservation. Fracture permeability is generally defined with the assumption of steady-state flow under a uniform macroscopic pressure gradient (van Golf-Racht 1982). Darcy's law presented in Equation 2.7 to define the steady-state unidirectional flow for a uniform sand column.

$$\frac{dp}{dl} = \frac{\mu q}{k} \tag{2.7}$$

Darcy's equation is only valid for linear flow; therefore it does not describe accurately flow at high-rate. When the flow reaches a high rate, or high Reynolds number, for instance in the gas flow in the near-wellbore region, inertial effects can also become significant (Mustapha et al. 2015). To account for non-linearity between flow rate and pressure gradient at high fluid rate, Forchheimer (1914) presented an empirical equation that includes an inertial term as shown in Equation 2.8.

$$\frac{dp}{dl} = \frac{\mu q}{k} + \beta \rho q^2 \tag{2.8}$$

### 2.1.2 Fracture Conductivity

One of the main goes for hydraulic fracturing design is to have sufficient fracture conductivity, which is a measure of the capacity of a fracture to carry fluid flow. It is described by the width of the fracture times the permeability of the proppant, as presented in Equation 2.9. In order to maximize the flow of hydrocarbons, restrictions in the system must be minimized. This is achieved by selecting the proper proppant and a compatible fracturing fluid, which are critical to determining the quality of the treatment, as it will dominate the final conductivity of the fracture. Likewise, the fluid pressure and applied stresses on the fracture, as well as the temperature of the reservoir, play an important role in the propped fracture. Increasing the value of these variables will increase the probability of proppant failure, which could affect the fracture flow capacity.

$$C_f = k_f w_f \tag{2.9}$$

- Fracture permeability ($k_f$): is the ability of the fracture to allow the fluids to flow through the proppant pack. This is a function of the proppant type, in-situ stress, damage from the residual gel, proppant crushing, and fines migration and deposition.

- Propped width ($w_f$): is the distance between the walls of the fracture that has been filled with proppant. This property is dependent on proppant selection as well as proppant concentration and can be reduced by the closure and cyclic stress, gel filter cake, proppant crushing and embedment into the rock.

#### 2.1.2.1 Conductivity Test

In the lab, the conductivity of a fracture is determined by measuring the pressure drop of a fluid flowing through a uniformly distributed proppant bed in a core with fixed length and height. The ISO 13503-5 conductivity test (International Organization for Standardization) is performed by flowing 2% KCl at low rate (2 ml/min) through a 2 lb/ft$^2$ proppant pack placed between two Ohio Sandstone cores, under closure stress that is maintained for 50

hours.

During the test, the differential pressure and flow rate are measured and the viscosity of the fluid is known. Then, the conductivity of the fracture is calculated using these values and applying Darcy's Law, as displayed in Equation 2.10.

$$k_f w_f = 26.78 \frac{\mu q}{\Delta P} \tag{2.10}$$

#### 2.1.2.2 Mechanisms Affecting Proppant Conductivity

Loss of conductivity in the fracture affects the well productivity. Barree et al. (2003) concluded that reference conductivity data are optimistic and the actual fracture conductivity is much lower than expected. Hence, the proppant conductivity should be defined considering all the damaging effects under downhole conditions:

- **Proppant Quality**

Proppant in the fracture will deform elastically or non-elastically in response to the closure stress depending on the type, which affects both permeability and width of the proppant pack (Sookprasong 2010). Proppant placed within hydraulic fractures is also subject to an evolving stress field and changes in chemical composition of the fluids residing in the pore space (Lee et al. 2009). Placing the proper type of proppant is critical to determine the quality of the treatment since this will dominate the final conductivity of the fracture.

1. Type: Different types of proppant agents are used to maintain the fracture open after injection stops. The main proppant types include: natural sands, light weight ceramics (LWC), intermediate strength proppants (ISP), high strength proppants (HSP), and resin coated sand (RCS) or proppants (RCP) (Figure 2.4). Natural sand (quartz sand) is the most commonly used proppant due to its availability and economics.

2. Strength: The proppant grains must be strong enough to withstand the closure stress or minimum horizontal stress, which is the pressure that the formation exerts on the proppant presented in Equation 2.6. If the proppant strength is inadequate, the closure

stress crushes the proppant, creating fines that reduce the permeability and conductivity of the proppant pack (Smith and Shlyapobersky 2000). Therefore, better-retained conductivity at closure pressure will be achieved with higher proppant strength. Figure 2.5 shows some strength comparisons between the most commonly used commercial proppants.

3. Size and Size Distribution: Proppants come in a variety of sizes ranging between 6 and 140-mesh (3.36 mm and 106 µm) (Al-Sadhan 2014). In general, proppants with larger grain size provide more permeability, yielding better conductivity; however, they tend to be weaker and easily crushed, because they support larger load due to their greater contact area with the fracture. Smaller grains have less permeability, although they tend to be stronger and more resistant to crushing and to invasion of the fines. Minimizing the mesh range will help achieving a constant proppant grain size that results in better permeability.

4. Roundness and Sphericity: Roundness is the measure of the smoothness of the edges and sphericity is how close the shape of the grains looks like a sphere. The more round or spherical the proppant grain is, the better the proppant-pack porosity will be. Similar sized grains that are round and spherical result in higher strength as stresses are evenly distributed.

- **Proppant Pack Damage**

1. Closure Stress Effect: As a response to closure stress, proppant in the fracture will deform elastically or non-elastically based on its type, affecting both permeability and width of the proppant pack (Sookprasong 2010). When two quartz grains are brought into contact, and a high mechanical stress is applied, the solubility at the contact points is greatly increased because of the strain placed on the molecular bonds (Weaver et al. 2007). This results in the removal of material from between the grains, which flattens

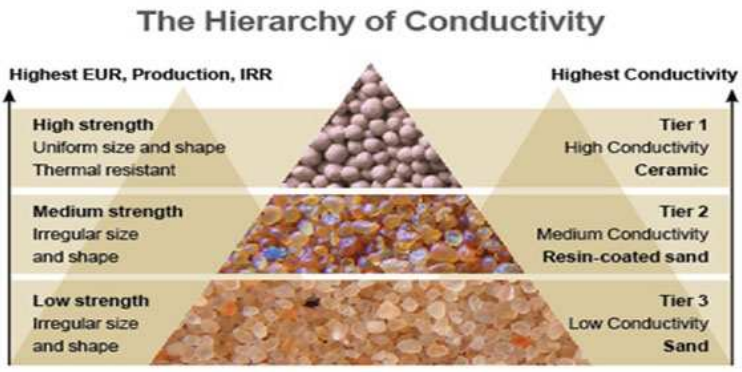


Figure 2.4: Different proppant types and their classification according to their strength and conductivity (Kullman 2011).

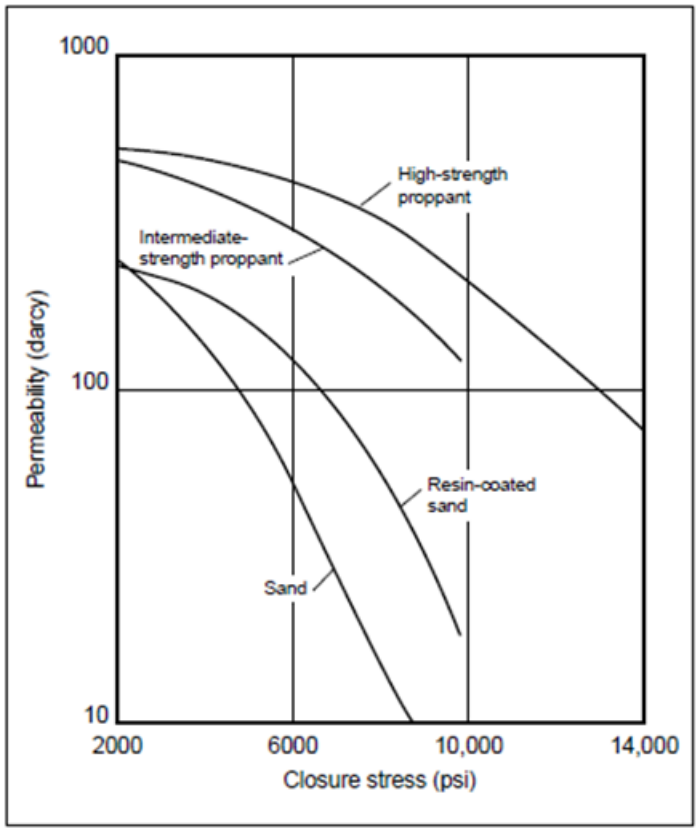


Figure 2.5: Strength comparison of various types of proppants (Smith and Shlyapobersky 2000).

the surface between them and leads to compaction, causing a loss of fracture width (Weaver et al. 2007).

2. Proppant Embedment: When proppants embed into the fracture walls, the conductivity is reduced due to the loss of width in the proppant pack, as shown in Figure 2.6. In addition, as a result of embedment, spalling will occur where fine particles will be generated by the failure of the reservoir rock. The smaller the proppant typically the less embedment will be observed due to the better load distribution.

3. Proppant Crushing: the major source for crushing is formation closure, particularly where the proppant is not well distributed. Generally, crushing is most prevalent at the interface and less toward the center of the pack. The potential for maximum crushing can occur during flowback and testing operations, when the flowing pressure at the perforations may be low, or initially in the production of a well because of the fracture gradient is at its maximum (Smith and Shlyapobersky 2000).

4. Fines Migration: Fines are very small particles that can reduce the proppant pack permeability. There are two main sources for fines: the proppant and the reservoir rock. Proppant fines are produced from proppant crushing and grain dissolution. Formation fines can be produced due to fines migration or spalling.

5. Cyclic Stress: The pressure pulse created every time the bottomhole flowing pressure is changed during production or workover operations can affect the proppant pack arrangement and proppant crushing. As a result of compaction and relaxation on the proppant packing, micro-fractures can lose all of the proppant particles causing them to close (Terracina et al. 2010).

6. Residual Gel: Incomplete clean-up process after fracture generation can lead to a considerable polymer concentration in the proppant pack (Reinicke 2010). This residual gel will plug the proppant pack permeability, reducing the fracture conductivity.

7. Proppant Pack Diagenesis: The term diagenesis has now been applied to proppants to describe laboratory observations in which crystalline precipitation has been observed (Duenckel et al. 2011). Diagenesis process involves the action of three serial processes: dissolution at grain-grain contact, diffusion at the interfacial water film separating the grains, and precipitation on the pore walls (Lee et al. 2009; Osholake et al. 2011). Porosity loss from proppant dissolution and subsequent re-mineralization in the pack leads directly to the loss of pack permeability (Raysoni and Weaver 2012; Weaver et al. 2007)

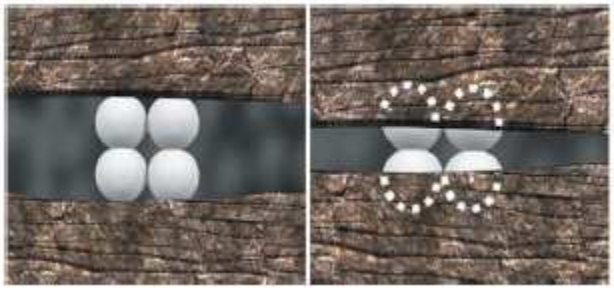

Figure 2.6: Graphic representation of proppant embedment into the formation (Terracina et al. 2010).

- **Formation Damage Effects**

1. Rock-fluid interactions: The fluid-rock physicochemical interactions could cause formation minerals dissolution and Young's modulus reduction. Moreover, the dissolution of minerals might cause a subsequent re-mineralization in the pack that could lead to loss of pack permeability.

2. Proppant Embedment: When the rock nature is soft (low Young's modulus, high Poisson's ratio), the proppant might be stronger and cause an indentation of the grain into the fracture wall. Embedment can be significant when static Young's modulus values are less than about 2 million psi or when core hardness values are less than about 20 kg/mm$^2$ (Lacy et al. 1998). This phenomenon can be worsened by rock-fluid

interaction, where the rock hardness decreases when the injected fluid saturates the formation.

3. Non-Darcy Flow: Darcy's law assumes laminar flow. Velocity distribution in the fracture can affect the apparent fracture conductivity (Forchheimer flow and turbulent flow) (Reinicke 2010). Most propped fractures have high velocities with the pressure drop being dominated by the square of the velocity (Al-Sadhan 2014).

### 2.1.3 Geomechanical and Geochemical Properties

During hydraulic fracturing, large amounts of fluid contact the formation rock and physical and chemical interactions occur. The treatment fluid disrupts the chemical equilibrium of the rock, hydrocarbon, and connate water system – leading to a physically and chemically altered zone of rock immediately adjacent to the fracture face (Pagels 2014). Fracture-face permeability can be influenced by many factors, including water retention, rock softening, proppant embedment, and chemical scale formation (Pagels 2014).

- **Rock-Fluid Interactions**

Matrix bulk mineralogy and mineral distribution in the formation play a critical role in water-surface interactions and thus on transport mechanisms (Padín 2016). Lessenger et al. (2016) compared SEM images of minerals in pores before and after fluid placement and identified calcite dissolution and fines migration as the cause of permeability reduction. Fine grains of multiple minerals migrated due to structural instability cause by authigenic calcite dissolution. Chemical processes that involve dissolution and precipitation of calcite minerals can further weld the rock reducing the initial porosity and permeability (Matthews 2011).

Pressure drop can be a major cause of calcium sulfate scale in producing wells and near the wellbore can create scale back in the formation as well as in the piping (Moghadasi et al. 2008). The chemical reaction taking place in this process is shown in 2.11.

$$CaSO_4 + H_2O \rightleftarrows Ca^{+2} + SO_4^{-2} + H_2O \tag{2.11}$$

LaFollette and Carman (2011)observed that the rock surface lost a large percentage of calcium and magnesium when Haynesville Shale samples were exposed to fracture fluids (Figure 2.7).

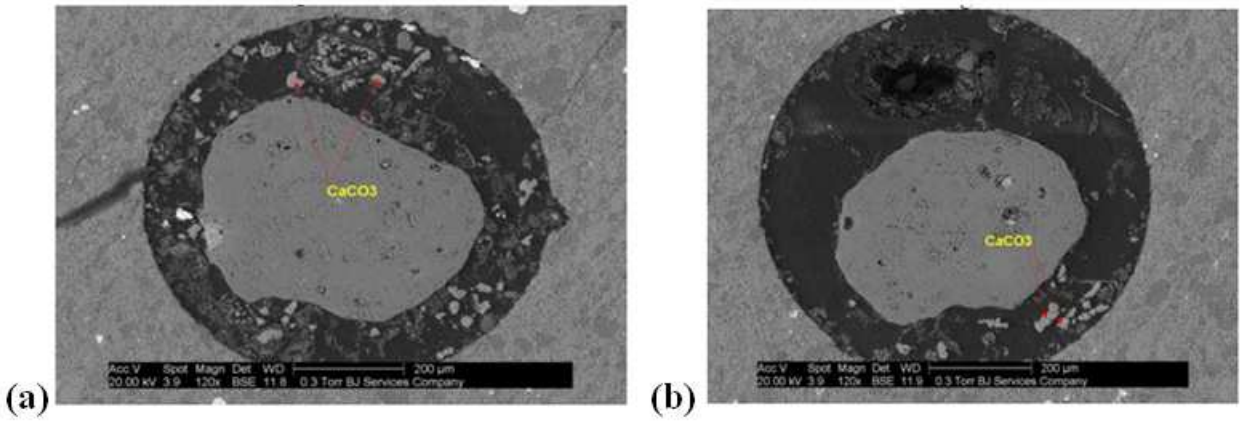


Figure 2.7: (a) Single 40/80 LWC grain embedded in shale after 90 days. (b) Single 2% RC 40/80 LWC grain embedded in shale after 90 days (LaFollette and Carman 2011).

- **Rock Composition and Geomechanics**

Dong et al. (2007)studied the impact of rock composition on geomechanical properties of the shale formation. They indicate that Young's modulus, brittleness, and hardness generally increase as clay minerals decrease or as carbonate minerals increase (Figure 2.8). They also demonstrate that a high fraction of carbonate minerals results in increased brittleness, whereas biogenic quartz enhances brittleness. Moreover, they suggest that TOC content has only a minor effect on the geomechanical properties of high thermal maturity shales.

Akrad et al. (2011) and Corapcioglu et al. (2014)found that the calcite present in the studied samples was thought to be partially dissolving due to the response of fracturing fluids (Figure 2.9). They related this mineral reaction as the main cause for Young's modulus reduction in their samples, which could allow additional proppant embedment to take place.

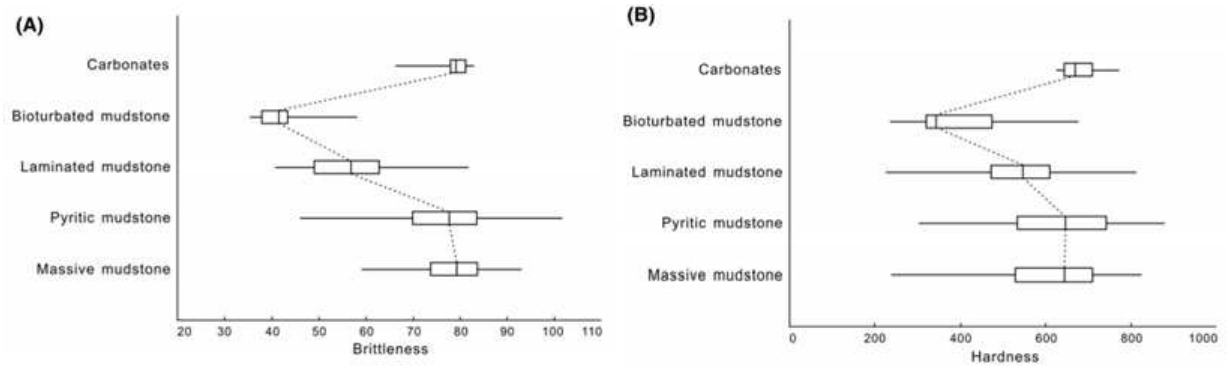


Figure 2.8: Box-and-whisker plots showing (A) brittleness and (B) hardness for shale samples differentiated by lithofacies. From left to right, different segments of the box and line represent minimum, quartile = 0.25, median, quartile = 0.75, and maximum values, respectively (Dong et al. 2007).

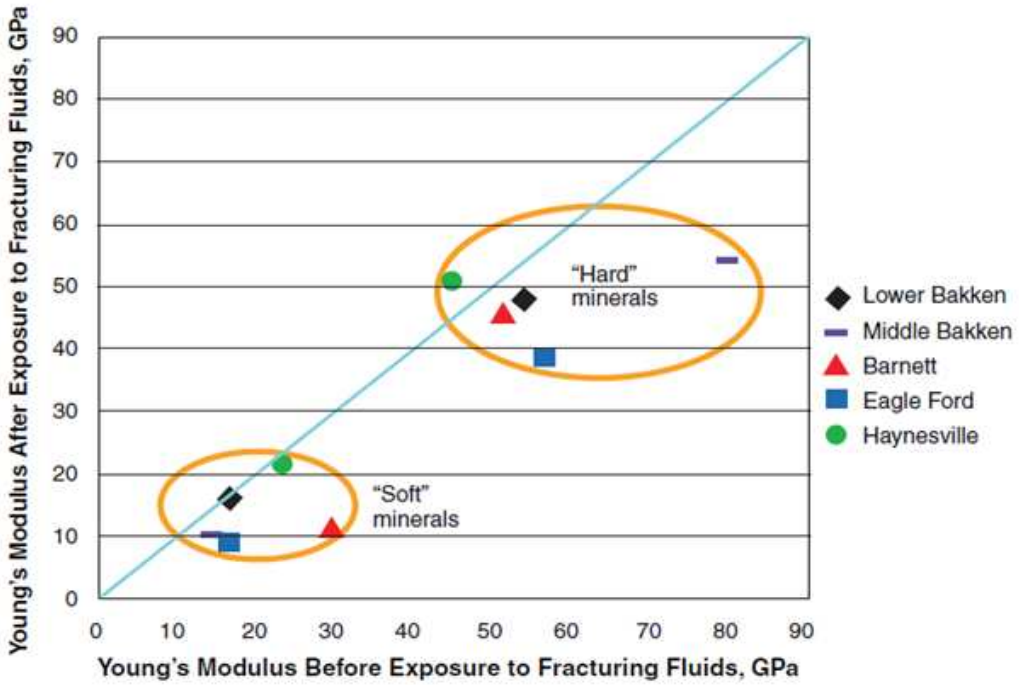


Figure 2.9: Average Young's modulus measurements for the different shale samples. The x-axis represents the initial Young's modulus before any exposure to fracturing fluids while the y-axis shows the Young's modulus for the samples after heating with fracturing fluids (Akrad et al. 2011).

- **Rock, Fluid, and Proppant Interactions**

Formation minerals dissolution and subsequent re-mineralization in the pack could lead to loss of pack permeability. When proppants are transported into the hydraulic fracture, exposure to high temperature and stress conditions promote geochemical reactions that can lead to the formation of porosity-filling minerals and result in reduction of the proppant packs' porosity as shown in Figure 2.10 (Osholake et al. 2011; Raysoni and Weaver 2012; Weaver et al. 2007; Weaver and Rickman 2010). When all three parameters -formation, fluid, and proppant- are combined, there is a possibility of unfavorable effects on the proppant pack and/or the formation during production (LaFollette and Carman 2011).

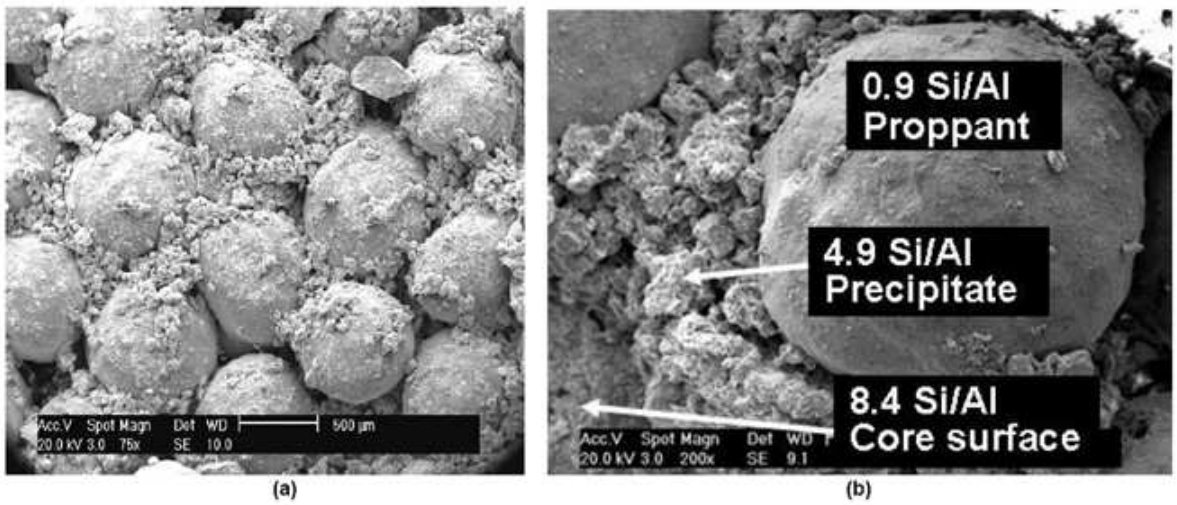


Figure 2.10: (a) Ceramic proppant after exposure to 10,000 psi closure stress and 275 °F in 2% KCl water. (b) A ceramic proppant grain embedded in Ohio sandstone after exposure to 10,000 psi closure stress at 250 °F in 2% KCl solution under static flow condition (Weaver et al. 2007).

The shear weakening in carbonates due to fluid saturation affects proppant embedment (Sharma et al. 2006). (LaFollette and Carman 2011) investigated the degree of softening in mudstones when exposed to different fracturing fluid compositional pH. The softening of the Haynesville Shale increased proppant embedment and decreased proppant pack conductivity. As stated by Penny (1987), the embedment of propping agents into the fracture face is a

function of both rock and proppant hardness. Embedment can be significant when static Young's modulus values are less than about 2 million psi or when core hardness values are less than about 20 kg/mm$^2$(Lacy et al. 1998). Moreover, the results presented by LaFollette and Carman (2010) imply that there is a particular period of exposure time in this specific rock-mineral-pore system during which the potential for proppant embedment will be most severe.

When proppants embed into the fracture walls, the width of the proppant pack is reduced as well as the conductivity of the fracture (Figure 2.11). Volk et al. (1981) conclude that when the proppant coverage drops below 50% of a monolayer in shale formations, the fracture will close due to embedment. In addition, as a result of embedment, spalling will occur where fine particles will be generated by the failure of the reservoir rock.

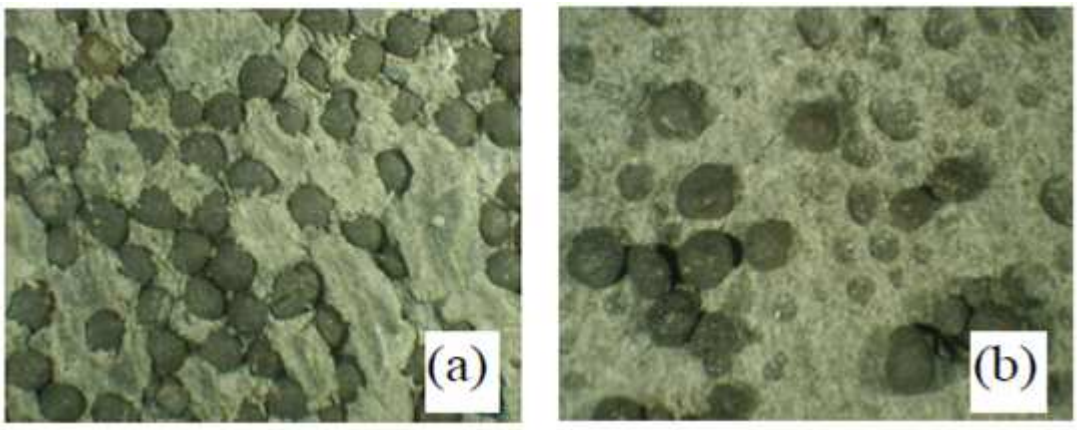


Figure 2.11: Post-test pictures of two shale samples showing (a) high proppant embedment in low stiffness sample, (b) low proppant embedment in high stiffness sample (Alramahi and Sundberg 2012).

# CHAPTER 3

# MATERIALS AND METHODS

In this section, a description of the experimental setup used for this study is presented. Three sets of experiments were conducted: (1) rock and proppant chemical interactions with fluid, (2) geomechanical variations in intact core samples, and (3) geochemical and geomechanical monitoring under triaxial stress conditions. By studying these elements both individually and in combination, it is possible to understand the impact of fluid selection on geochemical and geomechanical changes in the rock, specifically during the fracturing and production stages of the operations.

## 3.1 Sample Analysis and Characterization

The Niobrara shale samples were obtained from the outcrop format at the CEMEX quarry. The samples were characterized using X-ray Diffraction (XRD), and X-ray Fluorescence (XRF) analysis, Field-Emission Scanning Electron Microscopy (FE-SEM) imaging and Helical Computed Tomography Scan (CT-Scan).

### 3.1.1 X-Ray Diffraction (XRD) and X-Ray Fluorescence (XRF)

Standard X-ray diffraction (XRD) and X-ray fluorescence (XRF) were required to understand the mineral composition of the cores. These tests were performed by The Mineral Lab using crushed samples. The XRD provides a direct measurement of the mineralogical weight percentages, while the XRF provides an analysis of the major and trace elements present in the sample. The values are reported in weight percentage (%wt.) for major elements and parts per million (ppm) for the trace elements. Duplicate analyses were carried to check the measurement repeatability.

### 3.1.2 Field-Emission Scanning Electron Microscopy (FE-SEM)

FE-SEM is a non-destructive technique that produces images of a sample after scanning it with a focused beam of electrons. This provides the ability to visualize the microscopic changes in the rock pre and post-treatment. The images were obtained using the "TESCAN MIRA3 LMH Schottky" at the FE-SEM laboratory in the Department of Geology and Geological Engineering. This instrument provides topographical and elemental information at magnifications of 10x to over 300,000x at a spatial resolution down to the nanometer scale.

The equipment allows generating Secondary Electron (SE) and Backscattered electron (BSE) imaging, as well as Energy-dispersive X-ray spectroscopy (EDS). An SE image provides information about the topography of the sample surface. BSE images reveal detail information about the elements in the sample and their distribution. The EDS system detects X-rays emitted from the sample and provides a quantitative spectrum of chemical elements present in the surface of the sample. The samples were coated with gold to obtain a high image resolution.

### 3.1.3 Computed Tomography Scanning (CT-SCAN)

A Helical CT-Scan from Weatherford Labs was used to characterize the internal features of the cores. CT Scanners use an x-ray source and a detector. The x-ray passes through the object being scanned and generates an image. This test provides information about the heterogeneity of the rock and the fracture intensity present in the samples. This information will help in understanding the anisotropy and interpretation of the wave propagation through the ultrasonic wave velocities collected.

## 3.2 Rock and Proppant Chemical Interactions with Fluid

The purpose of this experiment is to evaluate the chemical reactions taking place when crushed formation and proppant samples are individually exposed to various fluid mixtures. The associated changes in the composition of the solution were monitored as a function of

time during the testing period.

### 3.2.1 Sample Preparation

The Niobrara outcrop samples were crushed and sieved up to 40-mesh. Following this process, the crushed rock and proppant samples were mixed with different water-based fluids in beakers, as shown in Figure 3.1. Two samples were mixed for each fluid type, to add repeatability to the experiment. The fluids used were distilled water (DI), 2% and 6% potassium chloride (KCl), and 2% and 6% magnesium chloride ($MgCl_2$). The fluids were chosen to have one with low ions concentration, one with a monovalent cation (alkali metal) and one a divalent cation salt (alkaline earth metal). Chemical reactions are dependent not only on the salinity of the fluid but also on the monovalent cation type and proportion of divalent cations (Lessenger et al. 2016; Scheuerman and Bergersen 1990). The concentrations were chosen based on field experience. The volume ratio (%wt.) was kept constant for all the samples: 20 ml of solid and 80 ml of fluid (1:4). They were sealed, kept at atmospheric pressure and at a temperature of $40^0$C. To improve the contact area between the solids and the solution, the samples were agitated every day.

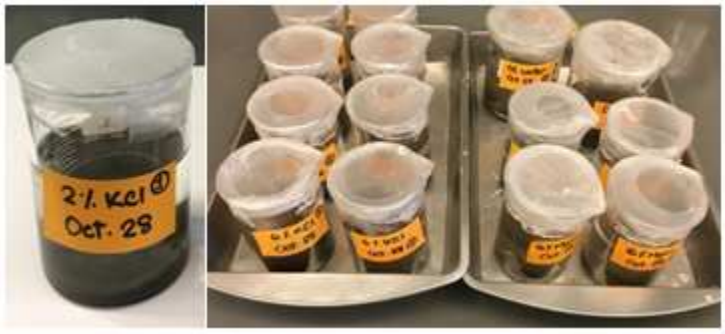


Figure 3.1: Crushed rock and proppant samples mixed with different fluids in beakers.

To monitor chemical elements present in the fluids and the changes in their concentration as a function of time, the fluid samples were taken at the initial state (before mixing) and after two and four weeks of mixing with the solid material (Figure 3.2). Then, the fluid samples were filtered to remove any solids that might have been caught in the sample. This

was completed using a decanter centrifuge. Afterward, the samples containing magnesium and potassium chloride were diluted. The high concentration of ions ($K^+$, $Mg^{2+}$, $Cl^-$) in solution affects the reading of the water analysis; therefore, the 2% brines were diluted 10 times while the 6% brines were diluted 40 times.

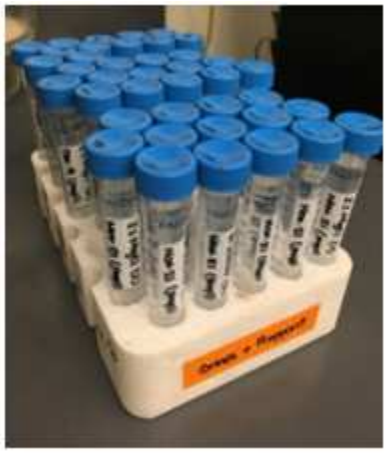

Figure 3.2: Fluid samples after preparation to be analyzed via Inductively-Coupled-Plasma-Atomic Emission Spectrometer (ICP-AES).

### 3.2.2 ICP-AES Analysis

The fluid samples were analyzed using a "Perkin-Elmer Optima 5300 DV" Inductively-Coupled-Plasma-Atomic Emission Spectrometer (ICP-AES). This equipment provides a rapid and precise trace detection of multiple elements in a single sample at parts per billion (ppb) level concentrations. ICP-AES is an atomic emission technique, where the inductively coupled plasma (ICP) serves as a means of exciting atoms and ions so that they emit characteristic wavelengths of energy (Gong 2008). The intensity of the energy emitted at the chosen wavelength is proportional to the amount (concentration) of that element in the analyzed sample (Murray et al. 2000). Thus, each emits a characteristic photon of energy at specific wavelengths that help identify the elements present and quantifying their concentrations.

To check the quality of the data generated by the ICP-AES, a calibration reading is made after a few samples are run. Calibration curves (functions) are created by measuring

emissions for standard solutions and a blank (Boss and Fredeen 2004). After calibration, a report is generated with standard readings for all the elements. If any of the parameters are wrong, then the machine is not calibrated and the data is not reliable.

## 3.3 Geomechanics Variations in Intact Core Samples

This set of experiments was conducted to evaluate the geomechanical changes in intact core samples when they were exposed to different fluids. The dynamic Young's modulus and Poisson's ratio of the core samples were measured before and after they are saturated with the fluids.

### 3.3.1 Sample Preparation

The Niobrara core plugs were drilled parallel to the bedding plane, using a 0.75-inch diameter bit and air to prevent any fluid damage prior to the experiments. Although drilling the cores perpendicular to the bedding plane would be a more accurate representation of the reservoir, in reality proved challenging due to fragility of the rock, breaking and shattering along the bedding plane. The samples were then cut using a diamond saw to obtain 1 inch length plugs with a flat surface.To obtain smooth and even surface, the end of the core plugs were ground using a precision surface grinder ($\pm$0.01 mm).The samples were clamped using a clamped Starrett V-Block, which is placed on a magnetic X-Y table under the sanding disk. The table rotates to sand the core surface until a flat surface is obtained. Finally, the samples were polished using fine sand paper (1000 grit) (Figure 3.3).

### 3.3.2 Saturation Cell

The core plugs were placed into the saturation cell (Figure 3.4) and subjected to vacuum pressure for 24 hours to remove all the air from the sample pore space and fractures and the entire cell system. After that, the saturation fluid was degassed and injected into the cell and the pressure was increased progressively until reaching 2000 psi. The fluids used were distilled water, potassium chloride (2% and 6%) and magnesium chloride (2% and 6%). The

Figure 3.3: Niobrara outcrop core plugs used for the geomechanical variations test

saturation process proceeded at room temperature for 30 days.

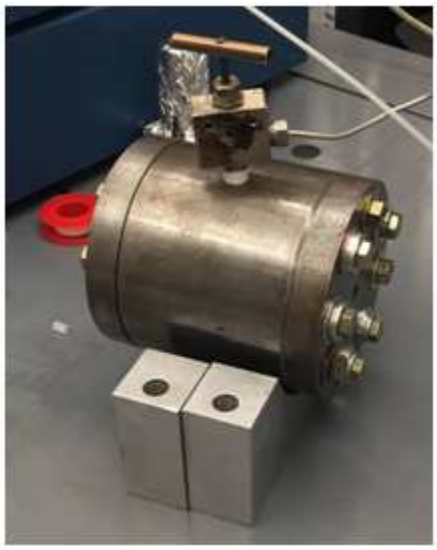

Figure 3.4: High pressure saturation cell

### 3.3.3 Acoustic Wave Velocities

Compressional or longitudinal and shear velocities of acoustic waves traveling through the samples were measured in the laboratory. Compressional waves (P) particle motion is parallel to the direction of wave propagation while in shear waves (S), the motion is perpendicular to the direction of wave propagation (Figure 3.5).

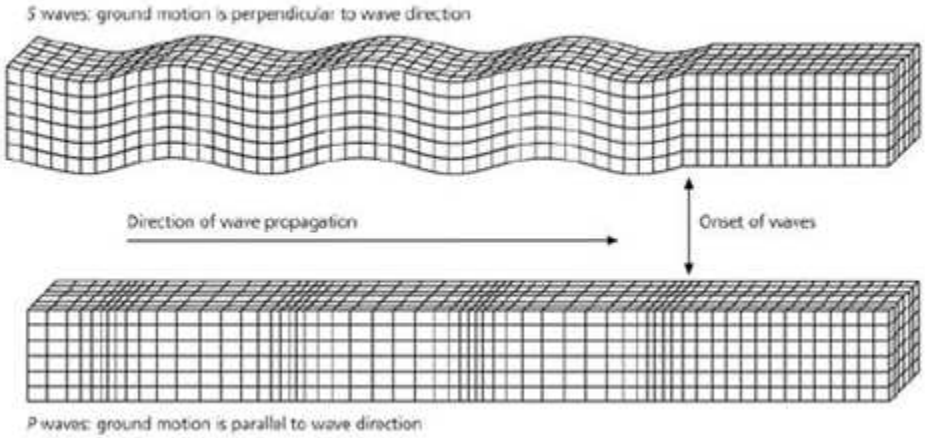


Figure 3.5: Illustration of the S- and P-wave direction with reference to thedirection particle propagation (Stein and Wysession 2003).

Room temperature ultrasonic measurements were performed through the cores before and after saturation using "Olympus Model 5058PR" piezoelectric transducers of 1 MHz central frequency. An ultrasonic pulse is generated by one of the transducers, travels through the core and finally read by the second transducer used as the receiver. The receiving transducer transforms the wave into an electric signal that transmits through P- and S-wave cables to a digital oscilloscope connected to the pulser/receiver. The output from the pulser/receiver is also connected to a computer for data acquisition. The piezoelectric transducer is shown in Figure 3.6 and the entire setting (digital oscilloscope, pulser/receiver and RF switch) is shown in Figure 3.7.

### 3.3.4 Uniaxial Stress Test

The uniaxial test was performed to measure the deformation of the samples at different stress conditions and with this obtain the static mechanical properties of the samples. The highly reliable, highly precise load and motion control servo-hydraulic uniaxial load frame made by MTS was used to perform the test (Figure 3.8). This frame can apply compression and tensile forces up to 250 kN. All the operation commands of servo-system can be handled by a software that provides real time data plots of displacement versus applied stress. The

resolution of the data is of ±0.1 second. The system could be used to test rock samples for indirect tensile strength, uniaxial compression strength, triaxial compression strength, and creep behavior.

The axial force and the loading frame displacement were recorded during the test of each sample before and after saturation. The pressure applied was then calculated by multiplying the axial force applied by the sample cross-sectional area.

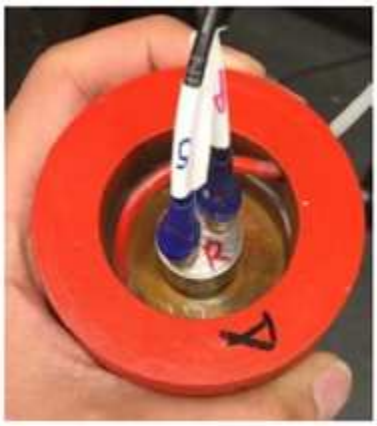

Figure 3.6: One of the piezoelectric transducers used to measure elastic wave velocity through sample.

### 3.3.5 Mechanical Property Determination

The mechanical properties measured in this study are Young's modulus and Poisson's ration. The Young's modulus is the ratio of the applied stress to the resultant strain and it represents the stiffness of the formation. The Poisson's ratio is the relation between axial and lateral deformation and is associated with how easily the rock will deform.

The dynamic mechanical properties were calculated from the measured elastic compressional and shear wave velocities and the density. The waves were measured parallel and perpendicular polarization to the bedding plane to understand the anisotropy of the samples. The wave velocity was calculated by dividing the length of the core by the arrival time of the wave (Figure 3.9). Then, the dynamic Young's modulus and Poisson's ratio were calculated using Equations 3.1 and 3.2.

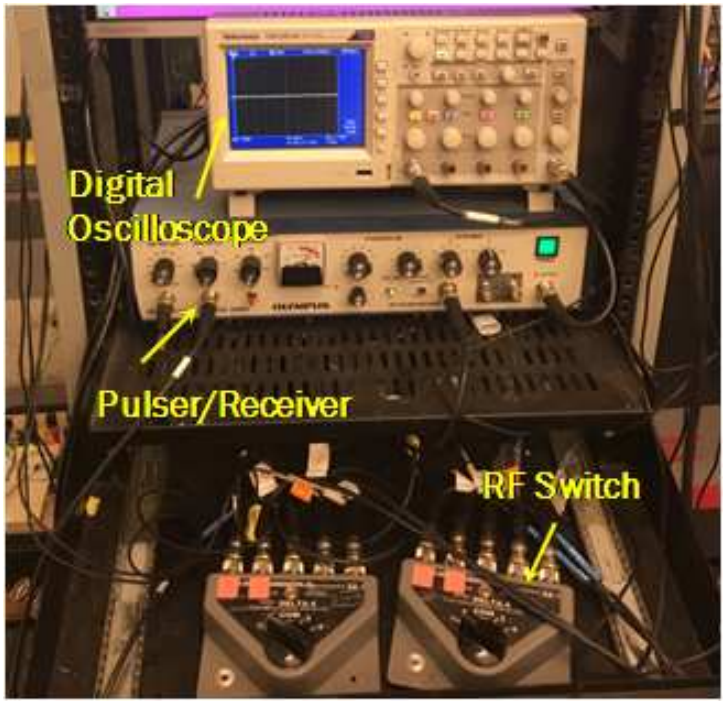


Figure 3.7: Digital oscilloscope, pulser/receiver and RF switch for selecting the measurement of P- and S-wave velocity.


Figure 3.8: MTS load apparatus used for uniaxial testing.

$$E = \frac{\rho V_s^2 \left(3V_p^2 - 4V_s^2\right)}{V_p^2 - V_s^2} \tag{3.1}$$

$$\nu = \frac{V_p^2 - 2V_s^2}{2\left(V_p^2 - V_s^2\right)} \tag{3.2}$$

The static Young's modulus was calculated using the applied stress and resultant strain measured through the uniaxial stress test. Then the Young's modulus was calculated using Equation 3.3. The radial deformation of the samples was not measured; therefore, the static Poisson's ratio will not be calculated.

$$E = \frac{\sigma}{\varepsilon} \tag{3.3}$$


Figure 3.9: Graphical representation of the P- and S-wave arrival times.

## 3.4 Geochemical and Geomechanical Monitoring under Triaxial Stress Conditions

This experiment was performed to monitor the chemical and mechanical changes in the formation, proppant, and fluid under reservoir conditions using a triaxial stress test assembly. This setup has been used for the simultaneous acquisition of coupled stress, strain, ultrasonic compressional and shear wave velocities, flow data and fluid sampling.

### 3.4.1 Sample Preparation

The samples used for this test have a calcite-filled fracture (Figure 3.10). The Niobrara core plugs (Nio-2.1 and Nio-3.1) were drilled with a 1-inch diameter bit and air. The preparation of these samples followed the same procedure showed in 3.3.1. Then, they were

fractured using Brazilian tensile tests to obtain a rough fracture, as shown in Figure 3.11. The fracture was created along the natural fracture filled with calcite present in the core, which was identified as the weaker plane in the outcrop cores during the drilling process (Figure 3.12).

Figure 3.10: Niobrara outcrop core plug containing a thick calcite-filled fracture (Nio-2.1) used for the triaxial stress test.

Figure 3.11: Brazilian tensile tests conducted to obtain naturally rough fracture surfaces for the triaxial stress state measurements.

### 3.4.2 Proppant in Fracture

The proppant agents used in the tests is a ceramic proppant of a 40-mesh size supplied by CoorsTek. The desired size was sieved out of the 20/40-mesh proppant using a 40-mesh

Figure 3.12: Niobrara outcrop block failed in the main calcite-filled fracture (weakest plane in the sample) and the presence of microfractures.

sieve and a dental vibrator to make sure a uniform size proppant is obtained for the tests (Figure 3.13).

Consequently, the fractures were filled with a proppant monolayer using heavy syrup to keep the proppant in place and tweezers to ensure a full packing shown in Figure 3.14. The syrup is soluble in water that will not cause blocking of the flow lines as fluids flow through the system. After the proppant was placed, the two halves of the core were brought together and wrapped with tape around the circumference to keep it together, as shown in Figure 3.15.

### 3.4.3 UNGI Laboratory Triaxial Test Assembly

The fractured core samples were tested in the Triaxial Test Assembly in the UNGI Geomechanics Laboratory. The experimental apparatus used in the study was originally designed and built by Dr. Ali I. Mese and donated to UNGI Geomechanics laboratory. Padin et al. (2016) used the cell to study osmosis in organic-rich shale samples. Hegazy (2016) then made some minor modifications to the setting and used it to measure fracture conductivity

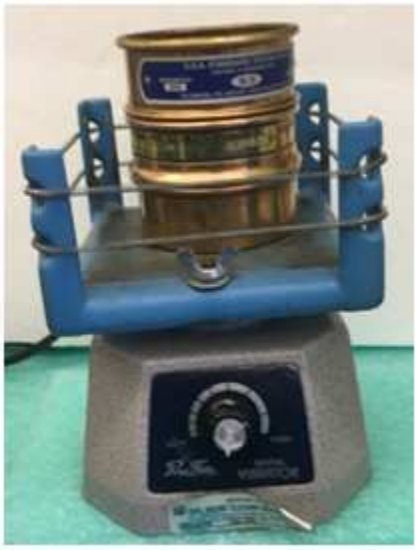

Figure 3.13: Proppant sieve on a dental vibrator to separate the 40-mesh grains size.

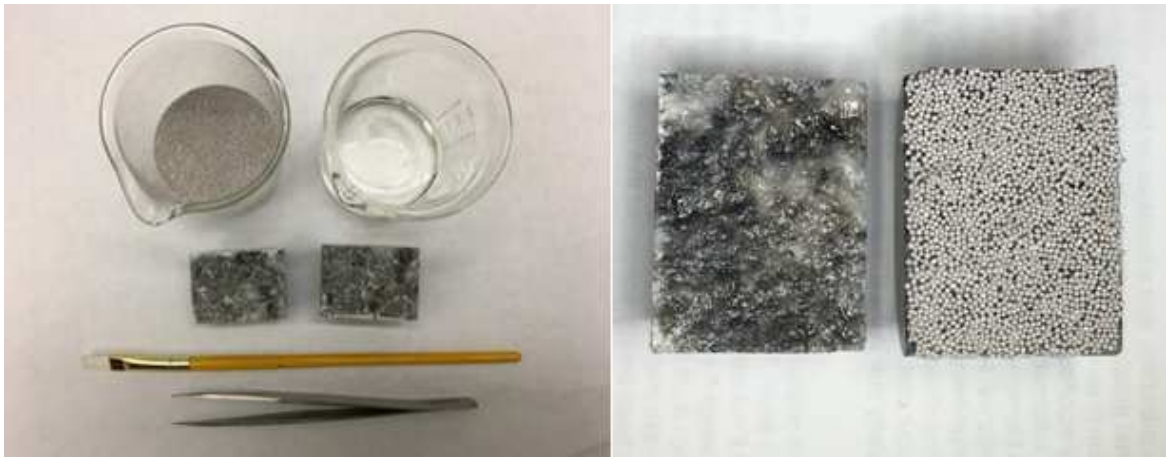

Figure 3.14: Materials used for placing the proppant in the fracture (left) and proppant monolayer in the fracture face of one-half of the core and rough fracture face in the other half of the core (right).

Figure 3.15: Fracture core filled with a proppant monolayer and wrapped with tape around the circumference.

at different stress conditions.

The special design implemented in the experiments provides continuous measurement of elevated in-situ pore pressure on the samples while fluids are circulated and ultrasonic compressional and shear wave velocities are simultaneously acquired. The test in the triaxial cell differs from the test in the conductivity cell mainly in two aspects: the way the stress is applied and distributed and the fracture face roughness. The conductivity cell only applies stress in a uniaxial direction (perpendicular to the fracture) while the triaxial cell applies pressure in the axial and confining direction, reflecting more realistic in-situ stress reservoir conditions. The triaxial test also uses core samples that have a rough surface rather than a smooth fracture surface, as in the conductivity cell test.

### 3.4.4 System Setting

The system consists of several components allowing coupled measurements to be carried out displayed in Figure 3.16. These components are: a triaxial load cell (1), a pore fluid injection system (2), a back pressure system (3), an axial and confining pressure system (4), a vacuum system (5) and a temperature control system (6).

The triaxial cell is a high-pressure vessel made of thick stainless steel allowing the simultaneous application of axial stress (simulating the overburden stress) and confining pressure (representing isotropic horizontal stress conditions). The pressure can be increased up to 10,000 psi (limited with the current pump capacity) using hydraulic oil pressure generated by ISCO syringe pumps.

#### 3.4.4.1 Triaxial Cell

The cell consists of two 1.5-inch pistons (upper and lower) used to apply the axial pressure and a cylinder chamber used to apply the radial pressure (Figure 3.17). The axial piston is driven downward to create axial stress on the sample by pressurizing an upper axial chamber. The confining stress is applied simply by pressurizing the area surrounding the core sample with hydraulic mineral oil. Separation of axial and confining fluids is achieved by means of a triple O-ring matching the inner diameter of the cell (Hegazy 2016). The pistons have inner lines where the pressure and acoustic wave cables pass through to collect the data. Pore fluid lines also pass through the pistons. The core sample sits between the two axial pistons and it's held in the radial direction by a flexible rubber sleeve (neoprene) that isolates the core plug from the radial stress chamber. A Solidworks design that describes the cell configuration in more detail is presented in Figure 3.18.

The original design by Padin et al. (2016) had porous filters placed on the top and bottom side of the core to prevent solids migrating to the circulating lines. However, this setting was not suitable for fracture conductivity experiments. Hegazy (2016) observed in her experiments that the real fractured sample permeability was masked by the presence of the porous filters. The holes in the pistons are located at the edge of piston end surface while the fracture is located in the center of the sample. Therefore, the assembly was modified for the fracture test by machining two disks grooved into the center across nearly their whole diameter and drilled holes matching the pore pressure holes in the upper and lower pistons. To prevent the proppant from escaping to the flow lines, manually made filters were glued to the grooves (Figure 3.19).


Figure 3.16: 3D view of the components of the triaxial stress experimental setup (Padín 2016).

#### 3.4.4.2 Pumping System

Four independent pumping systems control the axial, confining and pore pressure (inlet and back pressure). A general schematic of the system setup is shown in Figure 3.20. The axial and confining stress pumps (D) use mineral oil to transmit the pressure. Both injection (B) and back pressure (C) systems are made of syringe pumps, which generate fluid (pore) pressure (Padín 2016). The pore pressure pumps are isolated from the pore fluid by driving a piston cylinder placed in between the pump and the cell. This is to prevent any damage in the syringe pumps from the salts or solids present in the pore fluid. Additionally, a vacuum pump (E) is connected to enable the removal of all the air in the system prior to starting the test. To ensure the integrity of the system, HiP and Swagelok high-pressure joints, unions, connections, pipe work, and valves are utilized due to the high standards of manufacturing and pressure ratings (Hegazy 2016). For the purpose of this experiment, the system was modified adding a fluid sampler between the outlet pore pressure lines and the back-pressure cylinder (connected through $V_{15}$).

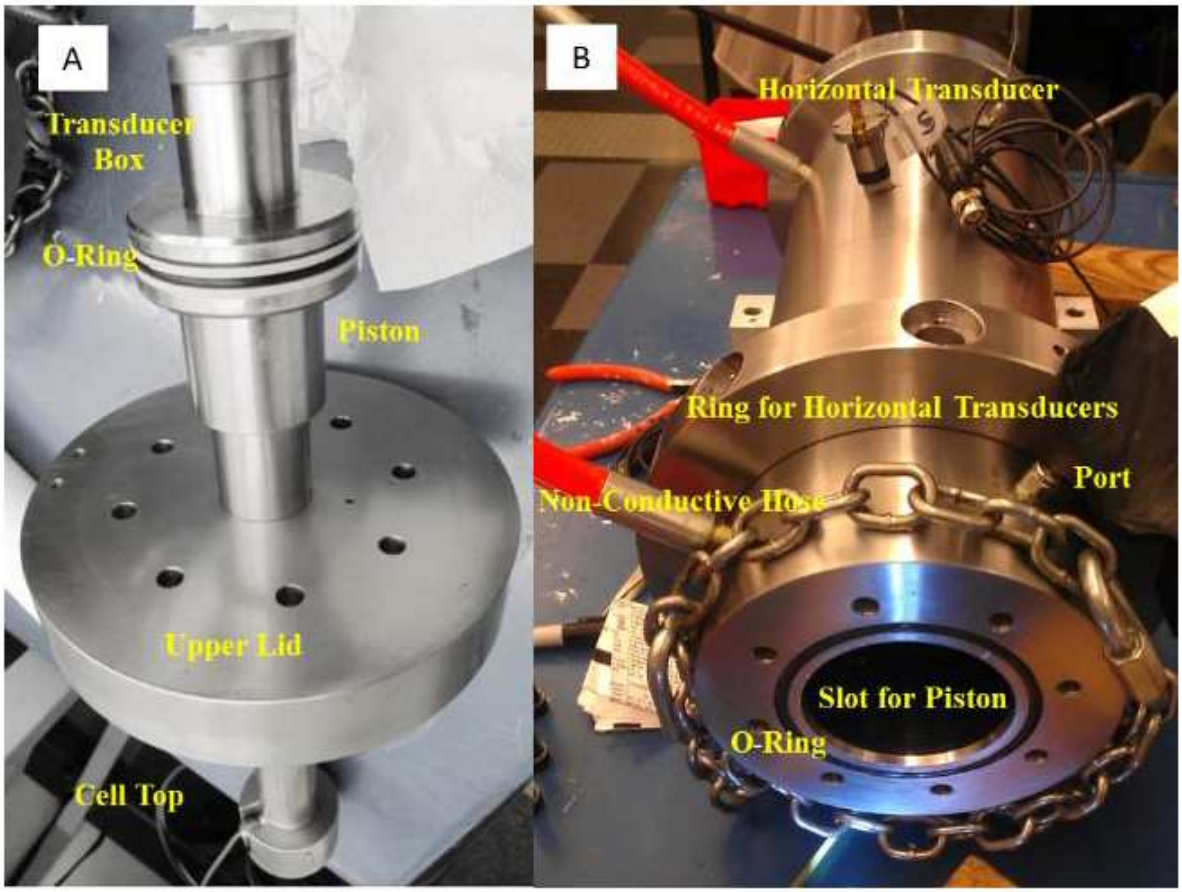


Figure 3.17: (A) Internal top piston and (B) the cell sample holder of the triaxial stress test assembly (Padín 2016).

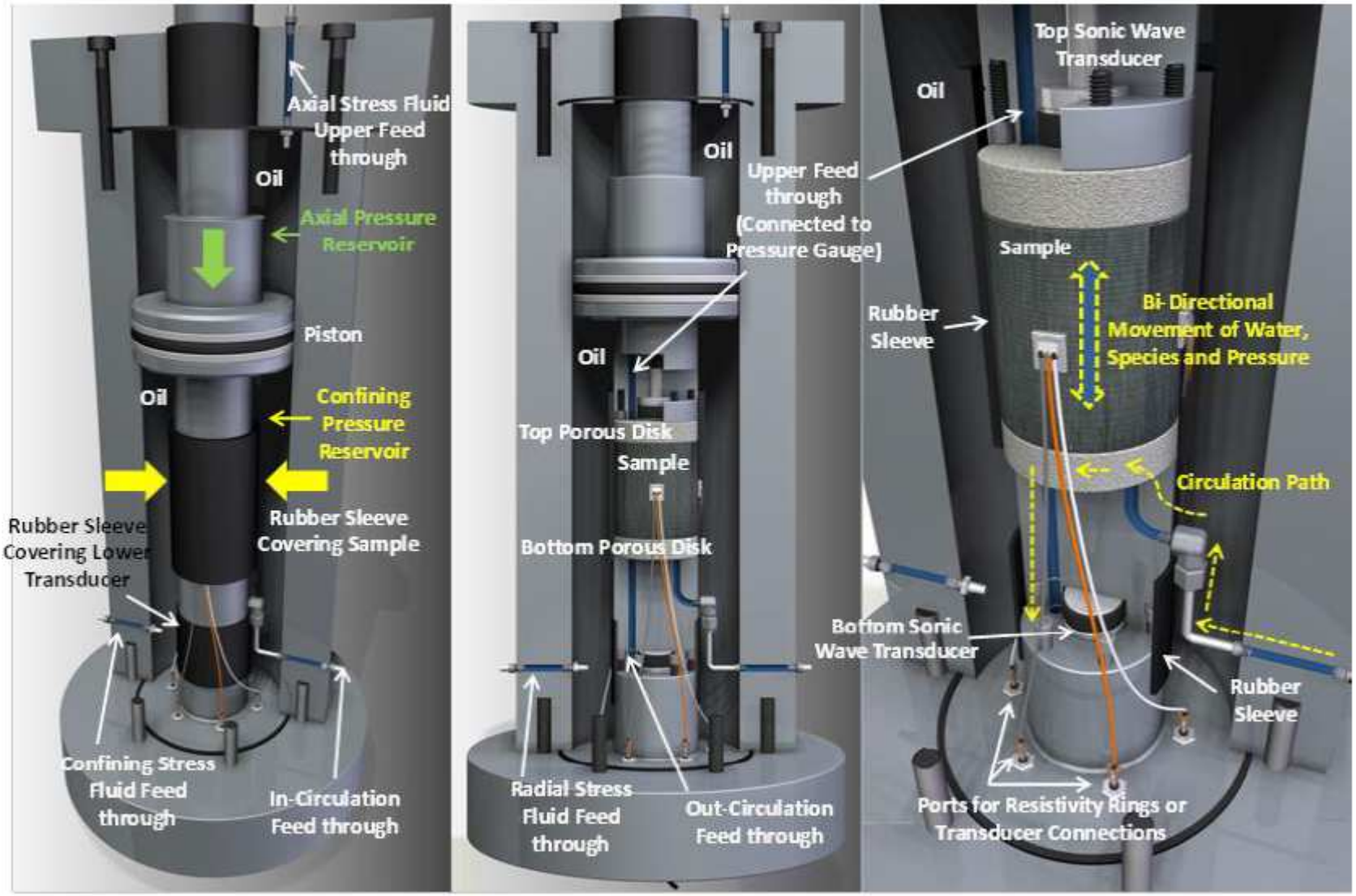


Figure 3.18: Cross-section of the cell where the sample is contained, designed using Solidworks® (Padín 2016).

#### 3.4.4.3 Cell Calibration

The reservoir is under anisotropic in-situ stress conditions present in the field. Therefore, the initial objective was to test the core under anisotropic stress conditions. Several trials were performed with metal core plugs to look at the stability of triaxial cell under different stress conditions with different confining stress to axial stress ratios. However, the first six calibration trials failed due to pressure instability in the system that caused the axial piston to move up uncontrollably with the rubber jacket. The piston movement pulls the rubber jacket with it making a path for the oil to leak into the core plug and contaminate the sample and the pore pressure lines.

Figure 3.19: New porous filter to accommodate the low-pressure drop through the fractured core samples.

For this reason, it was decided to modify the test to fit isotropic stress conditions. Isotropic stress conditions are achieved by determining the required applied pressures using Equation 3.4. $F_a$ represents the axial force, $p_a$ is the pump axial pressure; $p_c$ is the pump confining pressure; $A_c$ is the surface area of the larger section of the piston; and $A_s$ is the cross-sectional area of the piston. The representation of the forces and areas implemented are shown in Figure 3.21. Finally, the axial stress applied ($\sigma_a$) is calculated with Equation 3.5.

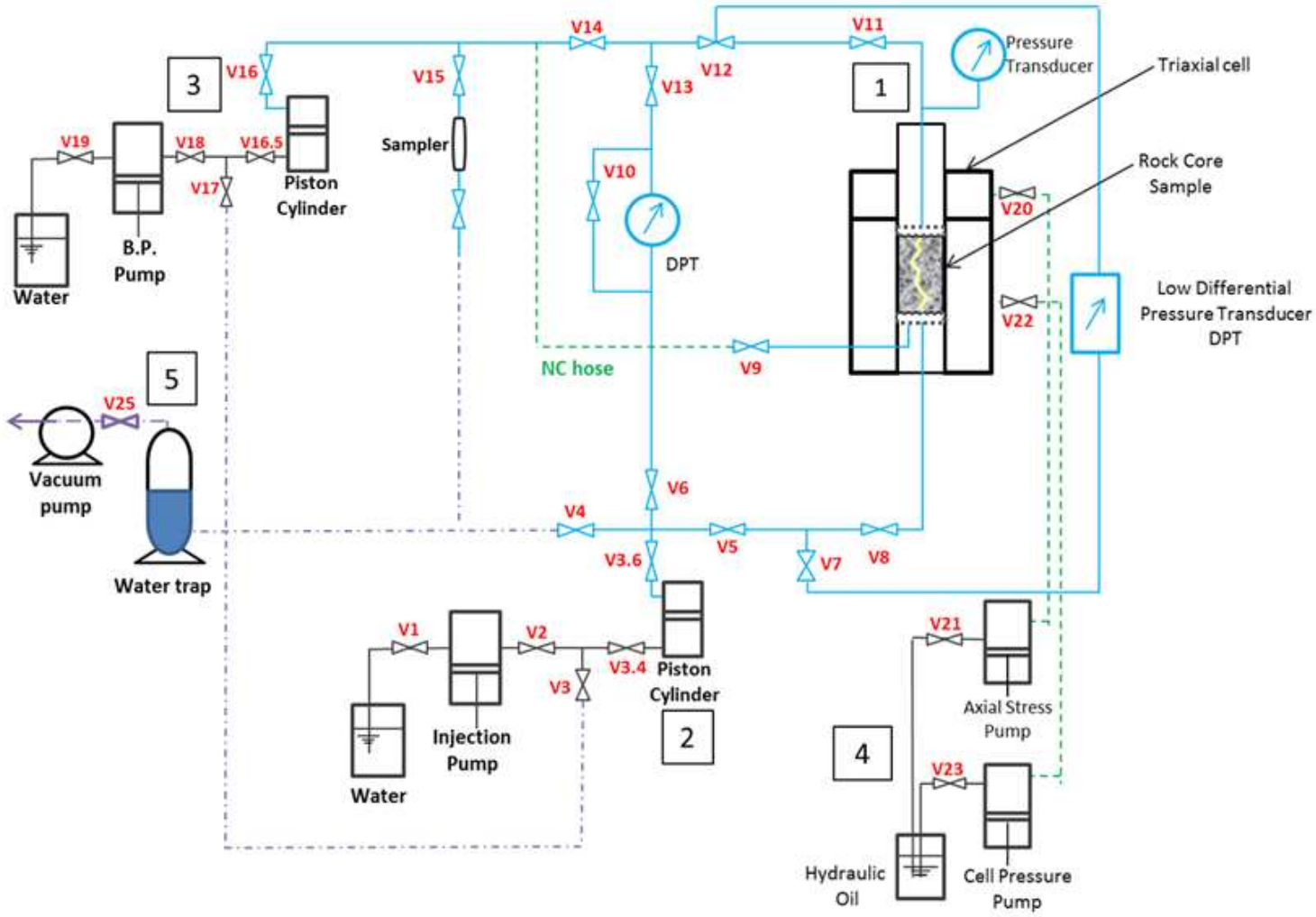


Figure 3.20: General diagram of the testing setup. In blue, stainless steel high-pressure lines; in green, non-conductive high-pressure lines; in purple, low-pressure lines used for vacuuming in the assembly (Modified from Padin et al. 2016).

$$F_a = P_a\,(A_c - A_s) - P_c\,(A_c - A_s) \tag{3.4}$$

$$\sigma_a = P_a A_s \tag{3.5}$$

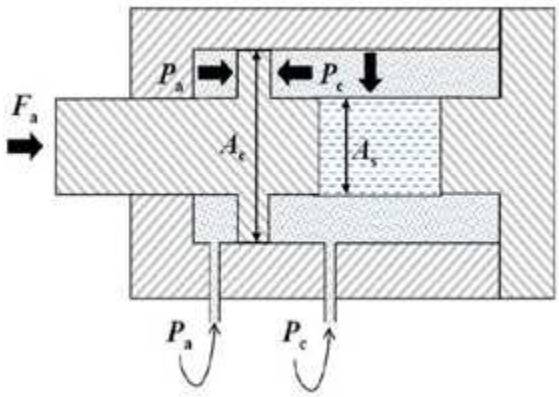


Figure 3.21: Representation of the forces applied to the core holder to create axial and confining stresses (Padín 2016).

Finally, the effective stress ($\sigma_e$) is determined using Equation 3.6, where the poroelastic or Biot's coefficient ($\alpha$) is assumed to be equal to 1.

$$\sigma_e = \sigma_a - \alpha P_p \tag{3.6}$$

#### 3.4.4.4 Temperature Control

The temperature affects the behavior of the pressure in the system. The entire triaxial test assembly is placed within an insulation cabinet made of polycarbonate sheets (Figure 3.16 (6)). The temperature in the system is kept constant at 40°C by flowing hot air with ±0.01°C resolution. The temperature is measured by two gauges connected to heater and fan controllers.

#### 3.4.4.5 Data Acquisition

The data is collected from the different components of the assembly through a data acquisition system, including the ISCO syringe pump controllers, vertical strain through a Linear Variable Differential Transformer (LVDT) (Figure 3.22), two differential pressure

transducers (DPT) at the lower and upper side of the cell, vertical compressional and shear wave velocity, and flow measurements. The data is collected and stored utilizing Labview.

The DPT measurement at the top of the sample is obtained using a high precision bidirectional Omegadyne pressure transducer (Figure 3.23). To measure the pressure difference between the inlet and outlet of the sample, the Veris PWLX05S Wet Pressure Differential Transducer is used. This transducer captures accurately even the small differential pressure changes due to its low differential pressure ranges (0-250 psig) (Figure 3.24).

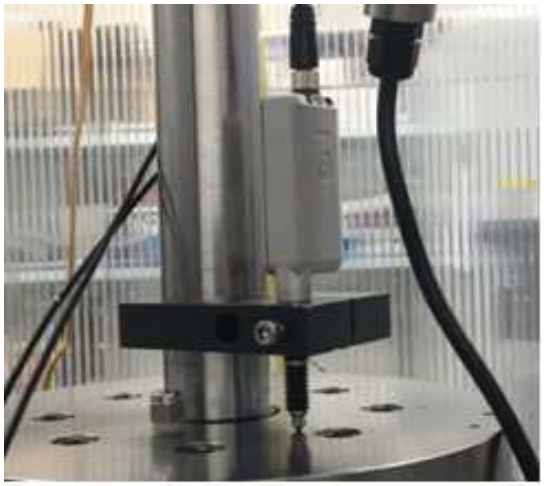

Figure 3.22: Linear Variable Differential Transformer (LVDT) used in the strain measurements.

#### 3.4.4.6 Fracture Conductivity and Fluid Sampling

During this test, constant monitoring of the fracture permeability and regular fluid sampling provided data that captures any chemical interactions between the injected fluids, the formation and the proppants used.

The initial step in this test was to flow the system to remove the syrup used to place the proppant in the fracture. Once the effluent fluid showed an electrical conductivity similar to the injected fluid, we assumed the syrup was removed. Then, the saturation of the core with distilled water was initiated. During this process, the pressure in the system was increased maintaining the effective stress constant at 100 psi. The exception was the first pressure

Figure 3.23: Omegadyne pressure transducer used for downstream pressure measurement.

Figure 3.24: Veris PWLX05S wet Pressure Differential Transducer.

step, where the effective stress was 50 psi and the rock was still dry since the pore pressure wasn't introduced yet. The pressure at each step was maintained until the volume change in the system was negligible.

After saturation was reached, the fracture permeability was monitored during the test and fluid samples were collected. The pressure in the system was increased stepwise until reaching the maximum allowed pressure. Once a pressure step was reached, the sample was kept in the cell for 72 hours while flowing the fluid from the inlet cylinder to the outlet cylinder at a rate of 0.03 ml/min. The outlet pressure cylinder was filled with nitrogen gas to maintain the back pressure at a slightly lower value than the inlet pore pressure. This is done to prevent any gas from flowing to the sample. The fluid samples were then collected every 24 hours through the sampler shown in Figure 3.25 and analyzed with the ICP-AES technique.

Figure 3.25: Sampler used to collect fluid from the triaxial stress experimental setup.

At the end of the pressure step period, the permeability of the fracture was measured, assuming that the flow going through the core matrix is negligible. Water permeability is not affected either by the gas slippage or by the inertial resistance of the fluid, because of the lower compressibility, higher density and higher viscosity of the liquid (Padín 2016).

Therefore, Darcy's Law can be used directly to calculate permeability. For this purpose, the flow area ($A$) is obtained by multiplying the fracture height ($h$) by the fracture width ($w_f$) (Equation 3.7). In this case, the fracture height is represented by the diameter of the core sample. Since the fracture width is unknown during the experiment, the conductivity ($k_f w_f$) is calculated using Equation 3.8, which is obtained by multiplying both sides of Equation 3.7 by $w_f$.

$$k_f = \frac{q\mu l}{w_f h \Delta p} \tag{3.7}$$

$$k_f w_f = \frac{q\mu l}{h \Delta p} \tag{3.8}$$

# CHAPTER 4

# RESULTS AND DISCUSSION

In this chapter, the results of the experimental investigation on Niobrara core samples are presented and discussed. Fluid chemistry, dynamic and static moduli, and core imaging illustrate a relationship between chemical and mechanical changes taking place in the rock. A conductivity test in the Niobrara is also compared to a previous experiment in the Vaca Muerta Formation performed under similar conditions.

## 4.1 Sample Analysis and Characterization

Two Niobrara Shale samples were used in this study. The mineralogy of these samples can be seen in Figure 4.1. Sample 1 was used as a crushed rock and whole core sample for fluid interactions and mechanical variations, respectively. Sample 2 contained a thick calcite-fill fracture and was used for triaxial cell experiments. Based on XRD, both samples are composed primarily of calcite, quartz, mica/illite, and dolomite.

XRF results are shown in Figure 4.2 and Figure 4.3 Data is split into two categories: main elements, reported in weight percent (wt.%), and trace elements, reported in parts per million (ppm). The main elements from XRF confirm XRD results where calcite, quartz, mica/illite, and dolomite are the primary minerals. Trace elements show the presence of elements related to organic matter, including chromium, copper, nickel, vanadium, and zinc.

FE-SEM yields two image types, BSE and EDS, shown in Figure 4.4. BSE shows the presence of specific elements as well as their shape and distribution whereas EDS shows a colored spectrum of the chemical elements and their distribution in the surface of the core. These elements are associated with the minerals present in the rock, notably the calcite-dominated matrix ($Ca^{+}$) and localized quartz ($Si^{+}$), clay ($Al^{+3}$, $Si^{+}$), pyrite ($Fe^{+2}$, $S^{+}$), and dolomite ($Mg^{+2}$).

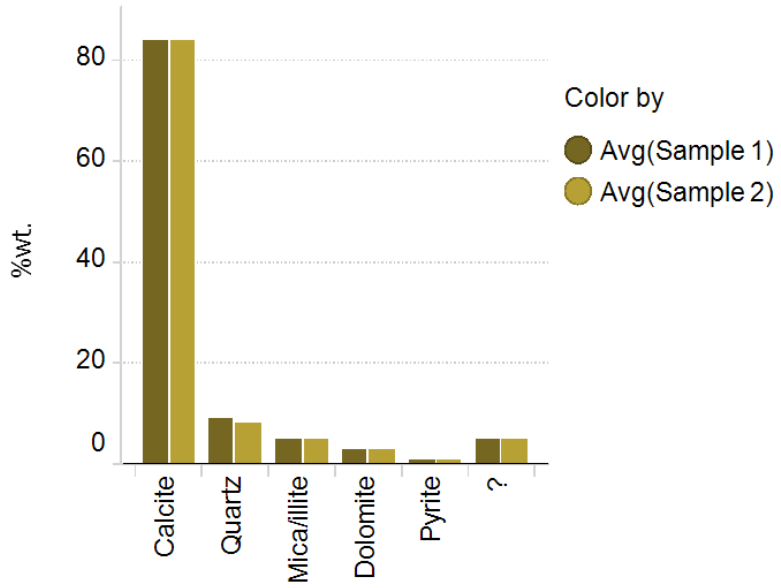


Figure 4.1: Mineralogical composition of the two Niobrara core plugs reported in weight percentage (wt.%).

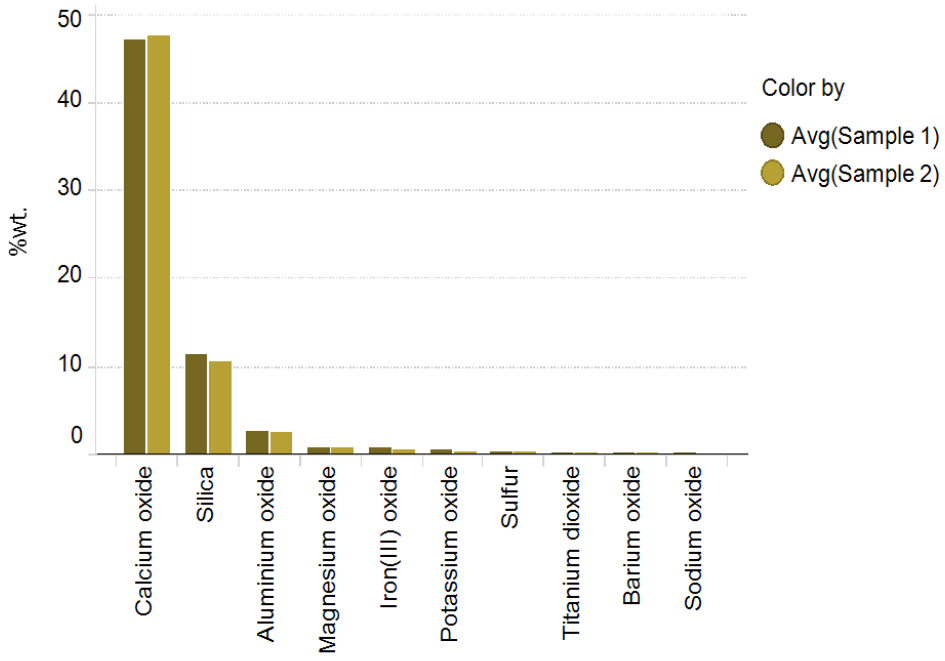


Figure 4.2: XRF results for the main elements present in two Niobrara samples reported in weight percentage (wt.%).

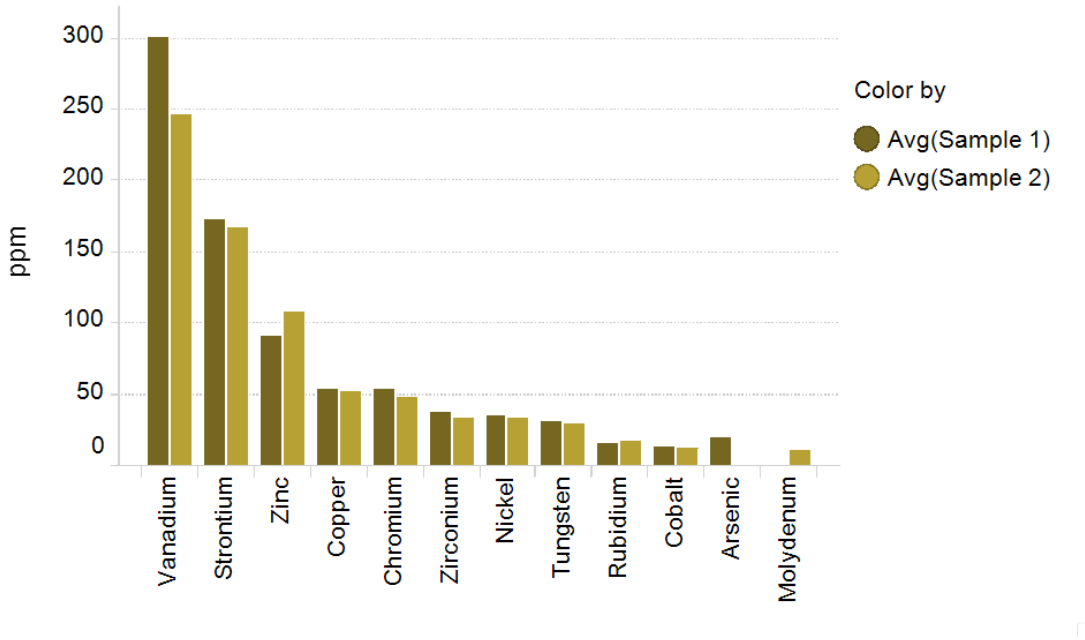


Figure 4.3: XRF results for the trace elements present in two Niobrara samples reported in parts per million (ppm).

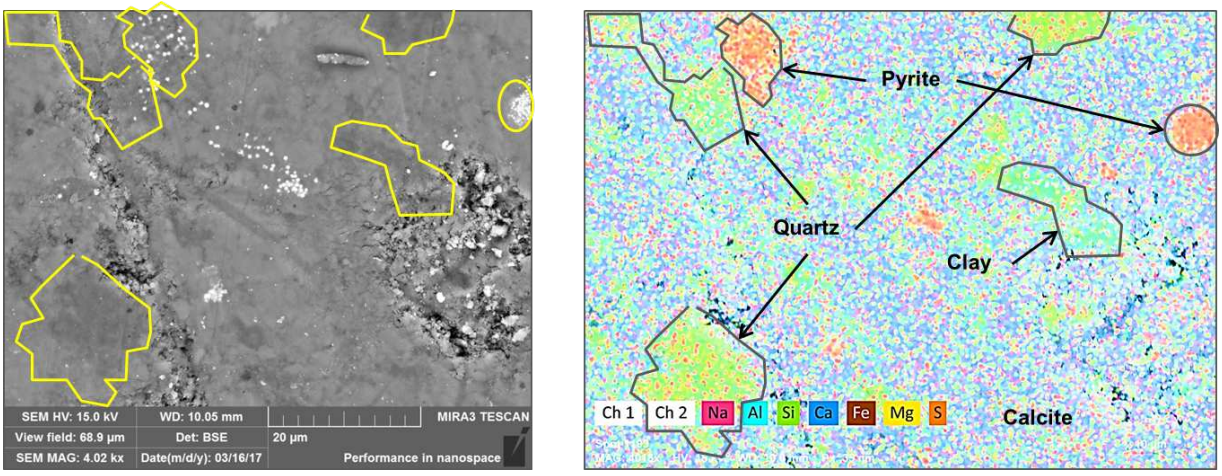


Figure 4.4: BSE (left) and EDS (right) images showing the calcite distribution along the matrix of the sample and some localized quartz, clay and pyrite.

Helical CT scans (Figure 4.5) show rock samples representative of Sample 1 are relatively homogeneous with limited calcite-filled fractures. CT scans for the triaxial stress samples (Nio-3.1 and Nio-2.1) are shown in Figure 4.6 where presence of the primary fracture (calcite-filled with internal cavities) and a natural fracture can be identified.

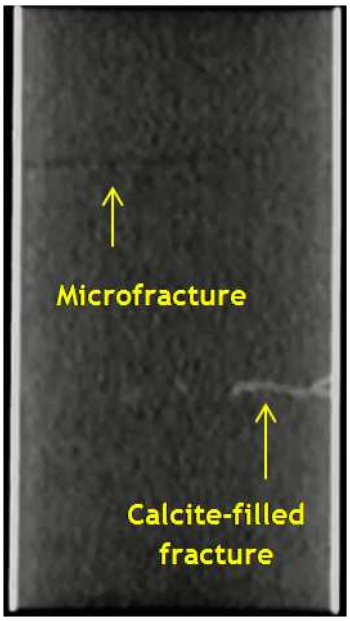


Figure 4.5: CT Scan of Sample 1, used for the chemical and mechanical variations tests, showing the presence of micro-fractures, some of which have been naturally filled with calcite.

## 4.2 Chemical Interactions with Rock and Proppant

The ICP-AES analysis report displays concentration per chemical element analyzed in each fluid sample. Table 4.1 shows a list of the chemical elements reported and their corresponding detection limit. The results show the elemental concentration in fluids before contact with the sample ($C_{initial}$) and after sample immersion for two or four weeks ($C_{after}$). The change in concentration ($C_{change}$) was then calculated using Equation 4.1.

$$\%C_{change} = \left(C_{after} - C_{initial}\right) / C_{initial} \tag{4.1}$$

The high content of potassium ($K^{+}$) or magnesium ($Mg^{+2}$) in the 2% and 6% brines caused the concentration of other elements to be undetectable. Therefore, these samples were diluted

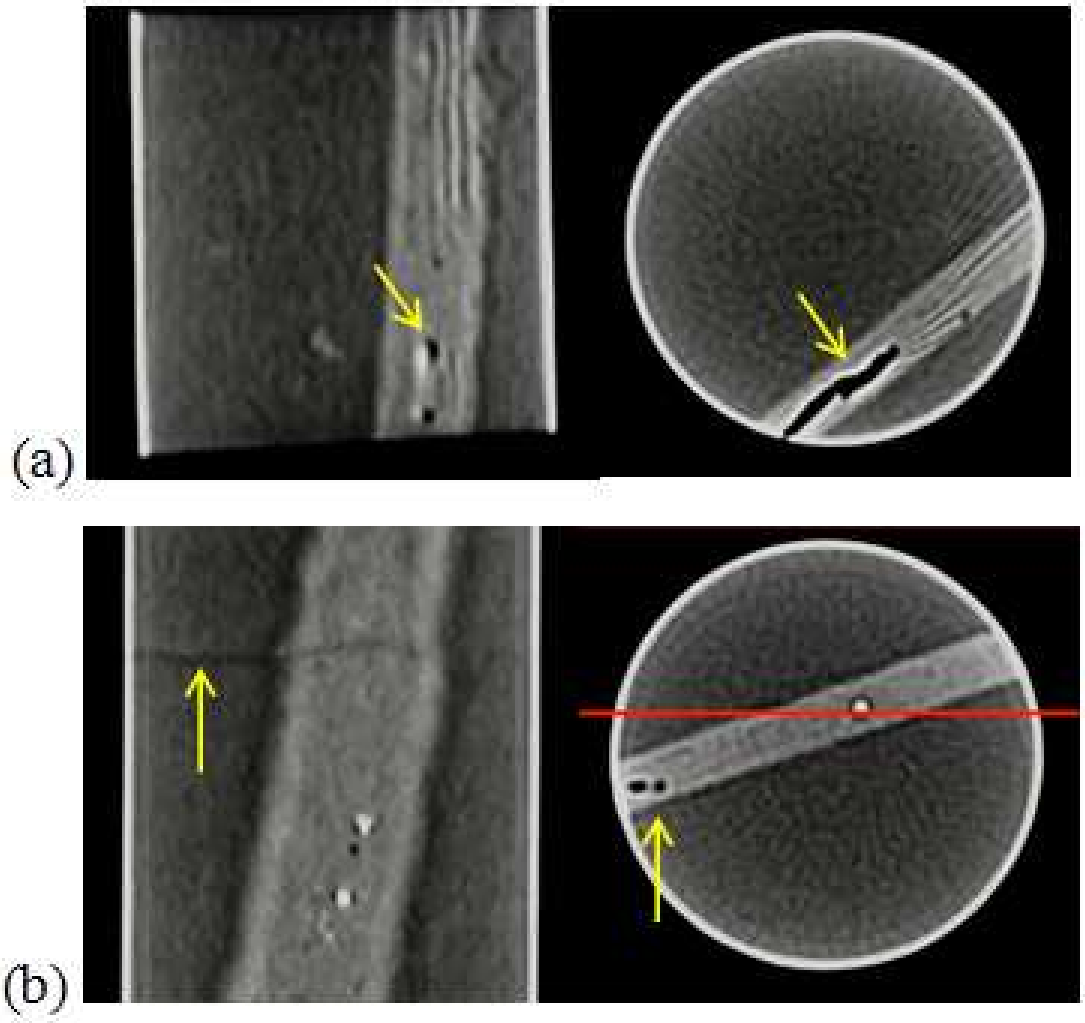


Figure 4.6: Cross-sectional (left) and top view (right) of the CT-Scan took on the core plugs Nio-3.1 (a) and Nio-2.1 (b) showing the presence of the main calcite-filled fracture with cavities and a natural fracture.

10x for 2% brines and 40x for 6% brines.

Table 4.1: ICP-AES analysis elements reported and their detection limits.

| Analyte | Name | Detection Limit (ppm) |
|---|---|---|
| Al | Aluminum | 0.0205 |
| As | Arsenic | 0.0047 |
| B | Boron | 0.0459 |
| Ba | Barium | 0.0001 |
| Be | Beryllium | 0.0002 |
| Ca | Calcium | 0.0064 |
| Cd | Cadmium | 0.0001 |
| Co | Cobalt | 0.0002 |
| Cr | Chromium | 0.0003 |
| Cu | Copper | 0.0011 |
| Fe | Iron | 0.0003 |
| K | Potassium | 0.0323 |
| Li | Lithium | 0.0014 |
| Mg | Magnesium | 0.0014 |
| Mn | Manganese | 0.0000 |
| Na | Sodium | 0.1345 |
| Ni | Nickel | 0.0005 |
| P | Phosphorus | 0.0106 |
| Pb | Lead | 0.0020 |
| S | Sulfur | 0.0276 |
| Se | Selenium | 0.0100 |
| Si | Silicon | 0.0114 |
| Sr | Strontium | 0.0001 |
| Tl | Thallium | 0.0018 |
| V | Vanadium | 0.0008 |
| Zn | Zinc | 0.0003 |
| Sn | Tin | 0.0017 |
| Mo | Molybdenum | 0.0010 |
| Sb | Antimony | 0.0051 |
| Ti | Titanium | 0.0002 |

To overcome dilution effects, the reported concentration of these samples was later multiplied by the dilution factors. The dilution procedure may have also introduced uncertainty on the ICP-AES analysis by reducing the concentration of a particular element below the detection limit of the testing equipment. In fact, when evaluating the results of the 6% brines,

most element analysis indicated either very high values or values close to zero as shown in Figure 4.7. We assume results from 6% brines are not reliable; therefore, the focus of the analysis will be on the data obtained from distilled water and 2% brines. The concentration of the two samples taken per fluid type has been averaged for an easier understanding of the figures presented in this section. An error bar is displayed in each of the charts to account for the error introduced by this calculation.

Figure 4.7 shows a bar chart per element with an average concentration change (%) per fluid type. This figure clearly illustrates the uniqueness of each element's behavior with the different fluids.Therefore, some elements were grouped according to their similar reaction behavior and its related damage mechanism.

### 4.2.1 Elements Related to Mechanical Properties

After evaluating each element separately, it was observed that silicon and iron are mostly dissolved by distilled water. This can be seen in summarized analysis results shown in Figure 4.9. Iron is potentially released from the reaction of pyrite (sulfur dissolution has a similar trend) while silicon is associated with the quartz. These elements could be used as a proxy for strength loss from cation substitution. Moon and Jayawardane (2004) found that the geochemical changes in the early stages of weathering do not appear to reflect a major change in the mineralogy, but indicate subtle changes in the structure of the minerals which is caused by the loss of $Ca^{+2}$, $Mg^{+2}$, and $Fe^{+2}$ ions from the crystal lattice. The authors suggested that the replacement of $Mg^{+2}$, $Ca^{+2}$, or $Fe^{+2}$ with $H^{+}$ or $Al^{+3}$ involves a weakening of the crystal structure and hence a loss of strength of the crystals. This is due to the replacement cations have different valences from the original cations, creating a charge imbalance; and the ionic radii of the replacement cations are smaller than those of the original cations. Graf (2008) suggested that the production of sulfuric acid from pyrite oxidation has the potential to dissolve silicate minerals. This explains why the iron and silicon have similar behavior.

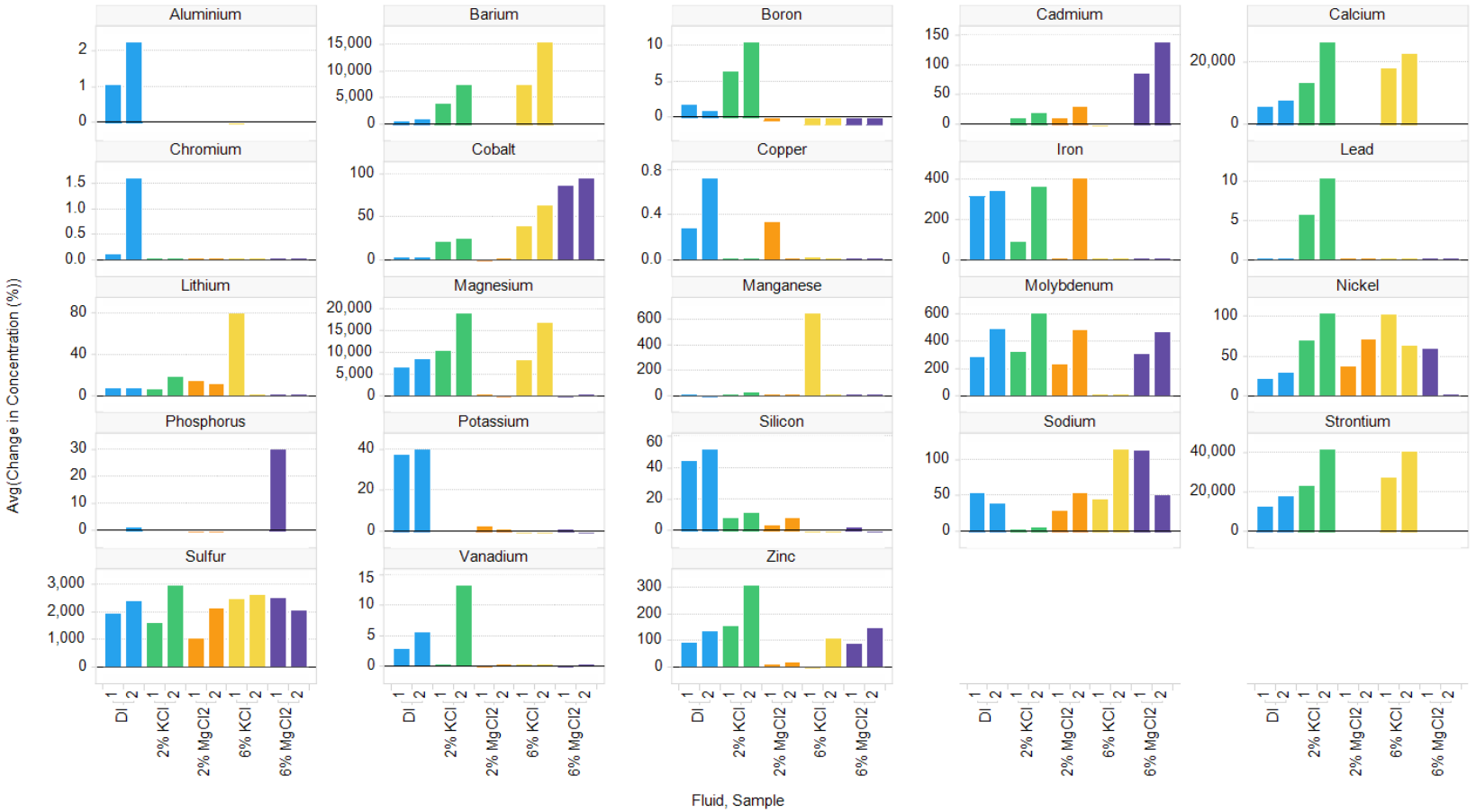


Figure 4.7: Element concentration change (%) per fluid type and sample number obtained from the beakers containing crushed rocks.

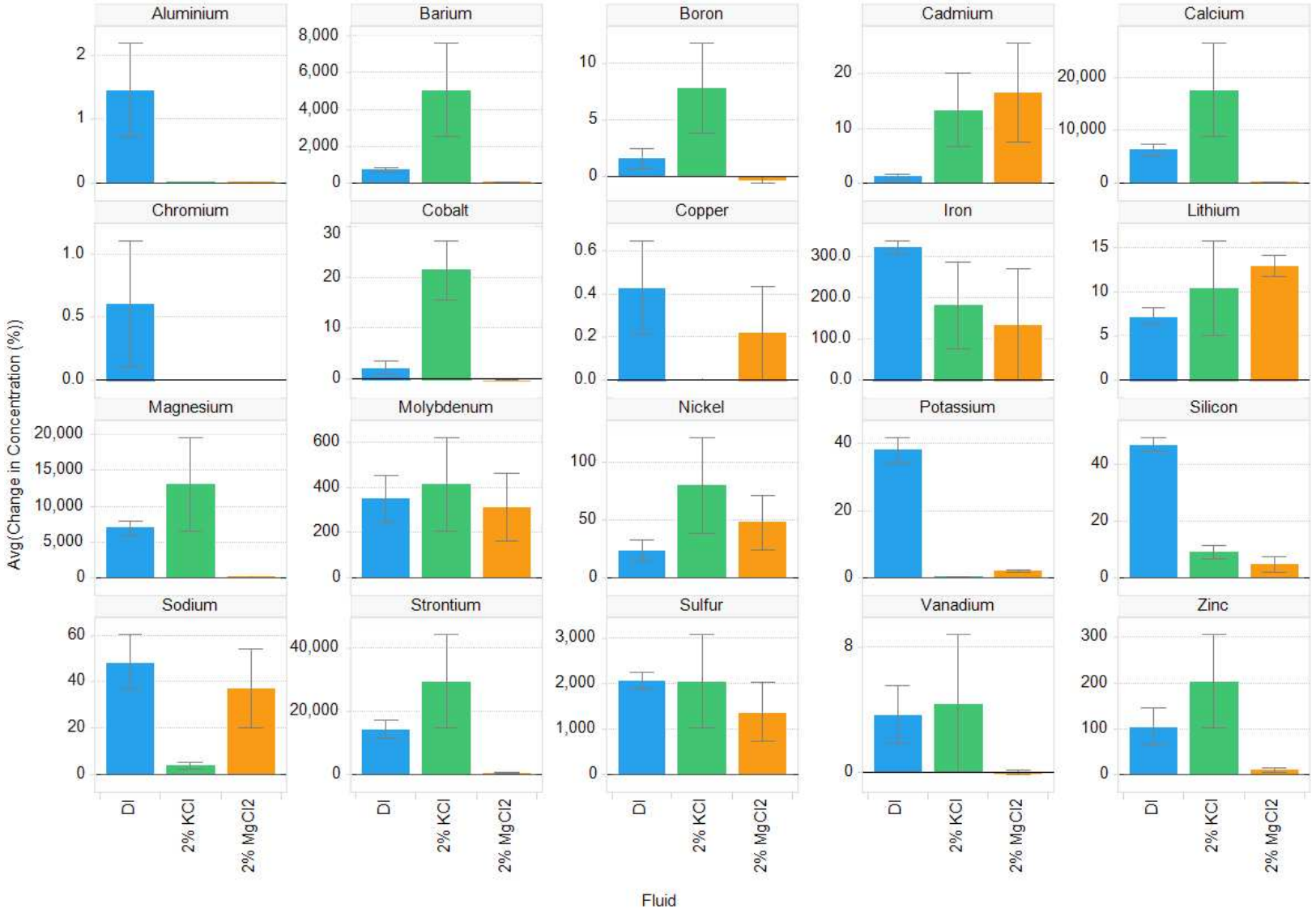


Figure 4.8: The average change in concentration (%) can be seen for the respective elements above. Each column represents a different fluid type obtained from the beakers containing crushed rock.

FE-SEM images of the core samples before and after fluid saturation are shown in Figure 4.4 and Figure 4.10 through Figure 4.12. It can be observed that the core saturated with distilled water was the only sample that did not indicate any trace of pyrite ($FeS_2$). This observation confirms the results obtained from the fluid analysis that show that distilled water dissolves most of the iron present in the rock compared to the other fluid tested.

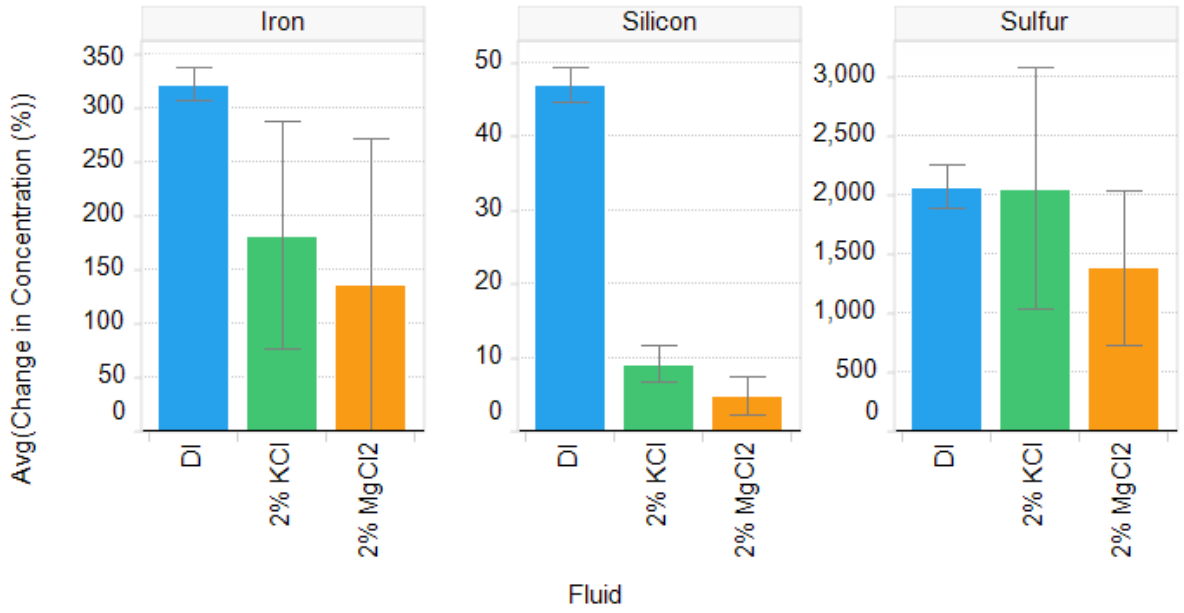


Figure 4.9: Iron, sulfur and silicon concentration change per fluid type after exposure to crushed rock.

### 4.2.2 Elements Related to Precipitates and Scales

Barium, calcium, lead, sodium, strontium, and sulfur are dissolved most readily by the 2% brines, especially 2% KCl, as shown in Figure 4.13. These elements could be the source for scales, fines migration, and/or other types of undesired precipitations (Table 4.2). Dissolution of calcite may also cause structural instability in adjacent minerals resulting in fines migration and pore collapse (Lessenger et al. 2016). Sulfate and carbonate scales can precipitate as a result of pressure changes and sodium chloride scales (halite) form with large temperature drops (Crabtree et al. 1999).

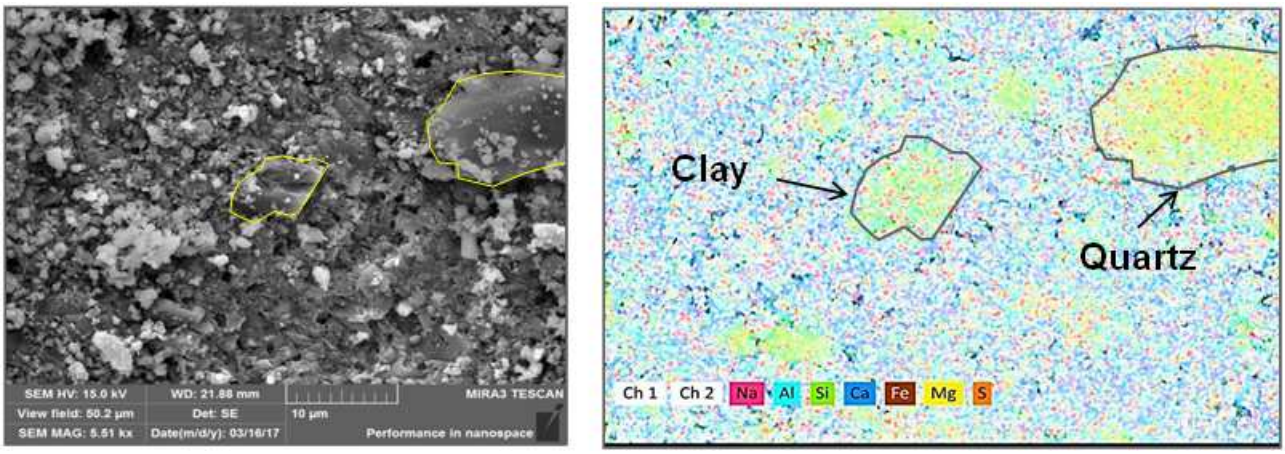


Figure 4.10: BSE images (left) and EDS images (right) of the core after being saturated with distilled water. The calcite distribution along the sample and localized quartz and clay.

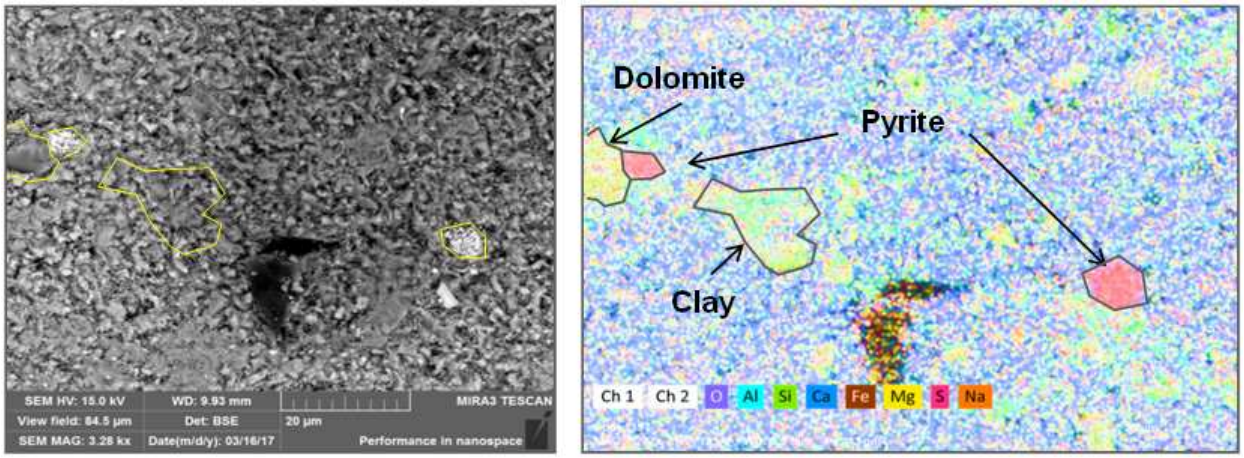


Figure 4.11: BSE images (left) and EDS images (right) of the core after being saturated with 2% KCl. The calcite distribution along the sample and localized quartz and clay.

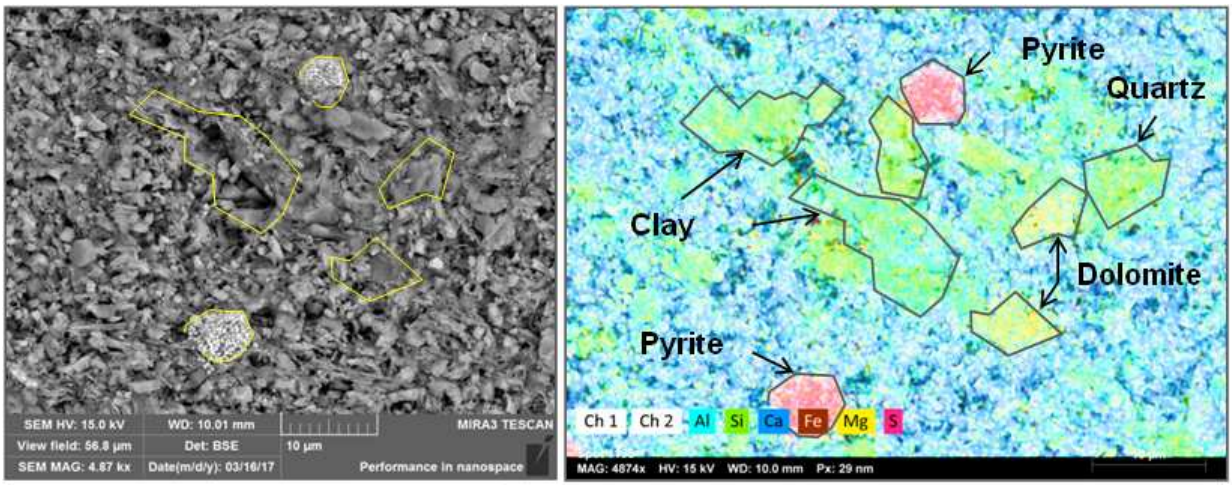


Figure 4.12: BSE images (left) and EDS images (right) of the core after being saturated with 2% $MgCl_2$. The calcite distribution along the sample and localized quartz and clay.

Table 4.2: List of common mineral scales found in oil and gas production facilities.

**TABLE 9.1—OILFIELD MINERAL SCALES**

| Mineral | Formula |
|---|---|
| Calcite | $CaCO_3$ |
| Aragonite | $CaCO_3$ |
| Vaterite | $CaCO_3$ |
| Anhydrite | $CaSO_4$ |
| Gypsum | $CaSO_4$ |
| Barite | $BaSO_4$ |
| Celestite | $SrSO_4$ |
| Mackinawite | FeS |
| Pyrite | $FeS_2$ |
| Halite | NaCl |
| Fluorite | $CaF_2$ |
| Sphaerlite | ZnS |
| Galena | PbS |

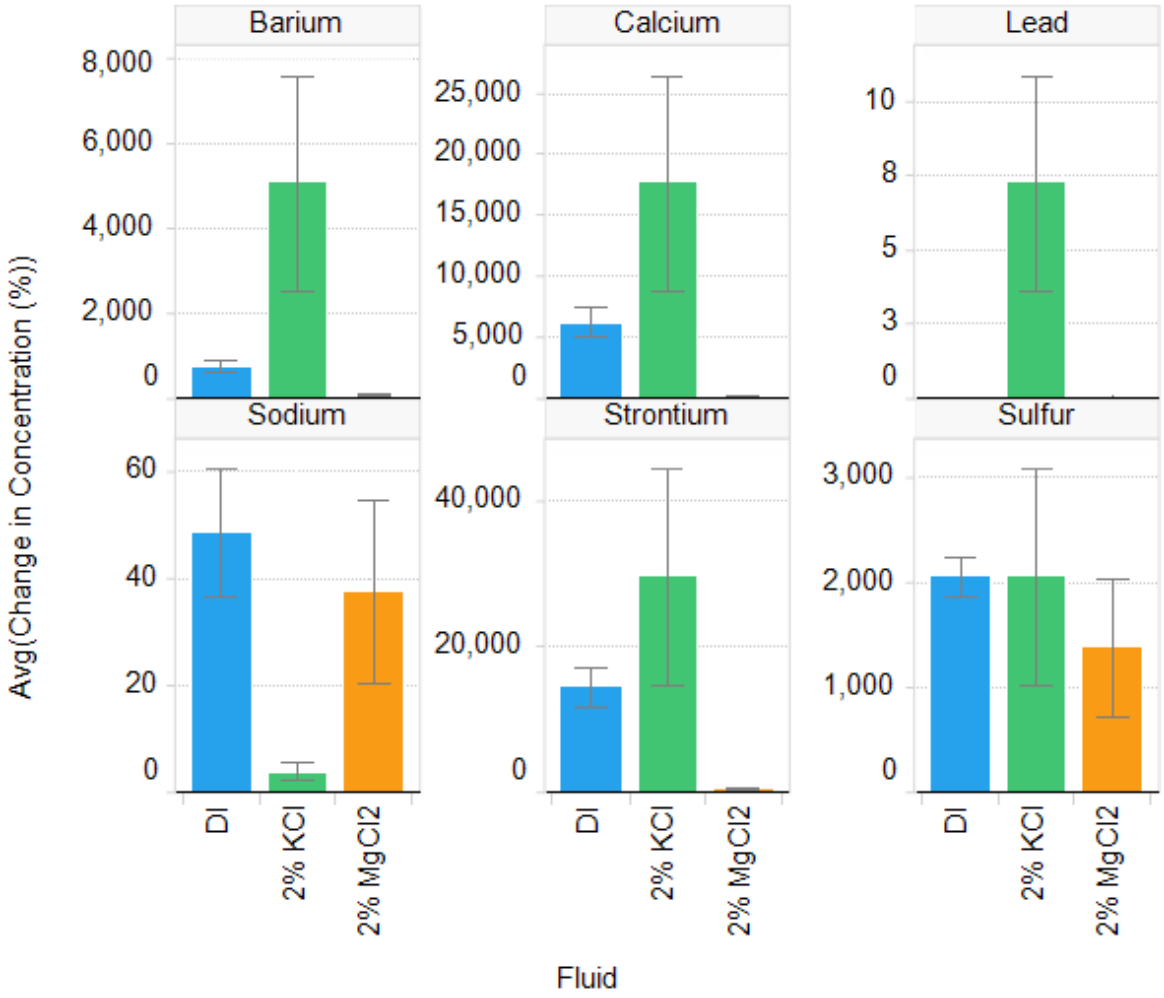


Figure 4.13: Barium, calcium, lead, strontium, sulfur and zinc concentration change per fluid type after exposure with crushed rock.

### 4.2.3 Elements Related Organic Matter

The change in organic element concentration is shown in Figure 4.14.Most of the dissolution is taking place with the 2% KCl solution. Tribovillarda et al. (2006) emphasize that nickel and copper abundance can serve as a marker for relatively high organic matter and may be retained within the sediment in association with pyrite ($FeS_2$). Additionally, there is evidence that organic matter surfaces interact with water and ions, similar to clay surfaces, due to the effect of the charge-bearing part of the surface (Mayer 1993). This is also because of the presence of amine-silicate interactions and weaker interactions such as hydrogen-bonding and van der Waals bonding (Padín 2016).

### 4.2.4 Elements Related to Proppant Reactions

Proppants are not inert materials and will also have interactions with the fluids to which they are exposed. Proppants undergo chemical reactions leading to porosity formation within the minerals and can result in loss of fracture conductivity (Weaver and Rickman 2010). The results of the fluid analysis obtained from the crushed rock beakers (Figure 4.15) show a similar behavior for each element when compared to the crushed rock results. The 2% brines have the highest impact in the chemical interactions, especially 2% KCl. The exceptions are potassium ($K^+$) and silicon ($Si^+$), where distilled water has the greater change in their concentration. LaFollette and Carman (2010) found most of the silica contained in 40/70 ISP was extracted from the grains and redeposited on the outside of the surface of the grains which also resulted in a significant loss in tensile strength of the material.

## 4.3 Geomechanics Variations in Intact Core Samples

Static and dynamic mechanical properties were measured before and after the saturation of the rock with fluids. This was performed to understand the effect of rock-fluid interactions on the geomechanical properties of the Niobrara Formation.

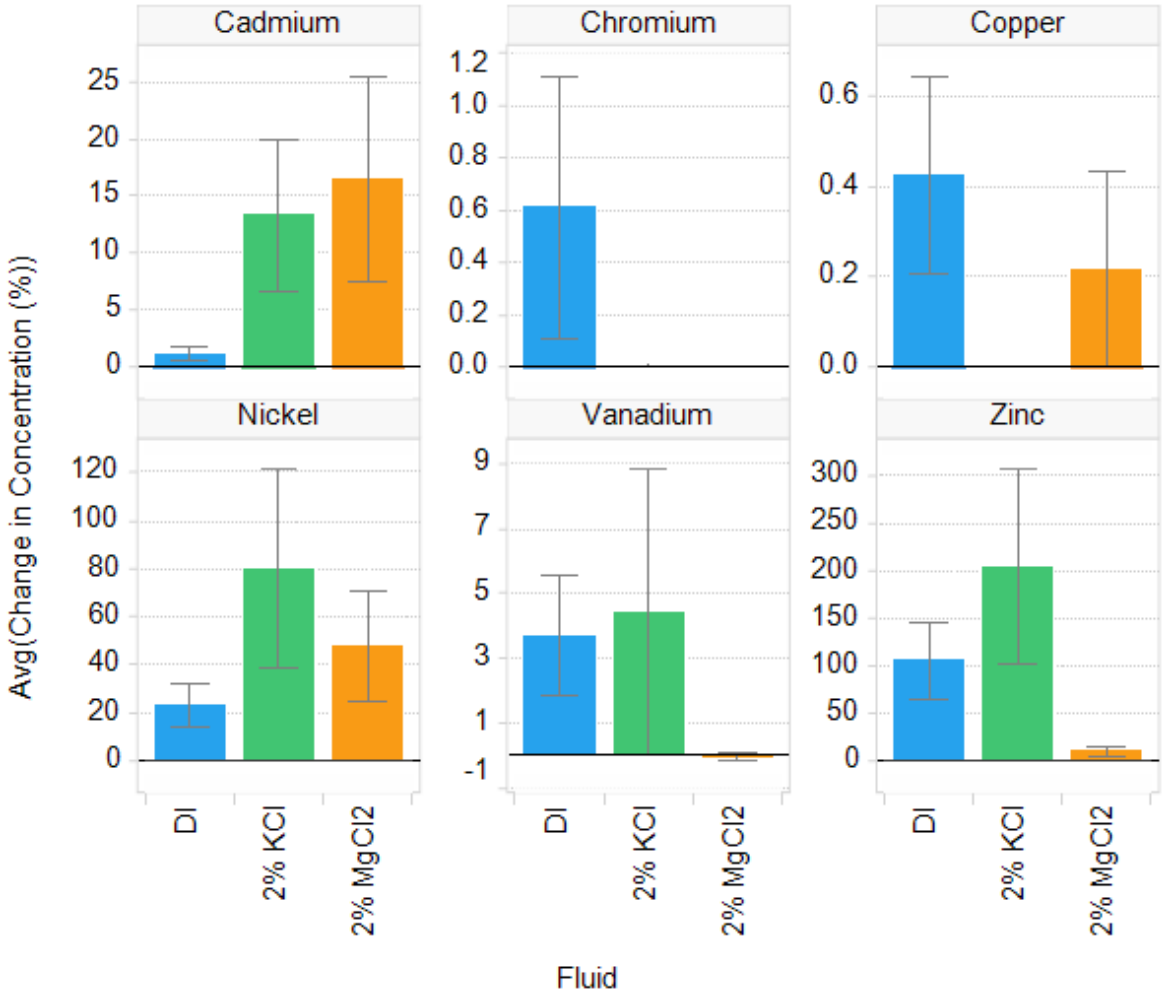


Figure 4.14: Cadmium, chromium, copper, nickel, vanadium and zinc concentration change per fluid type after exposure with crushed rock.

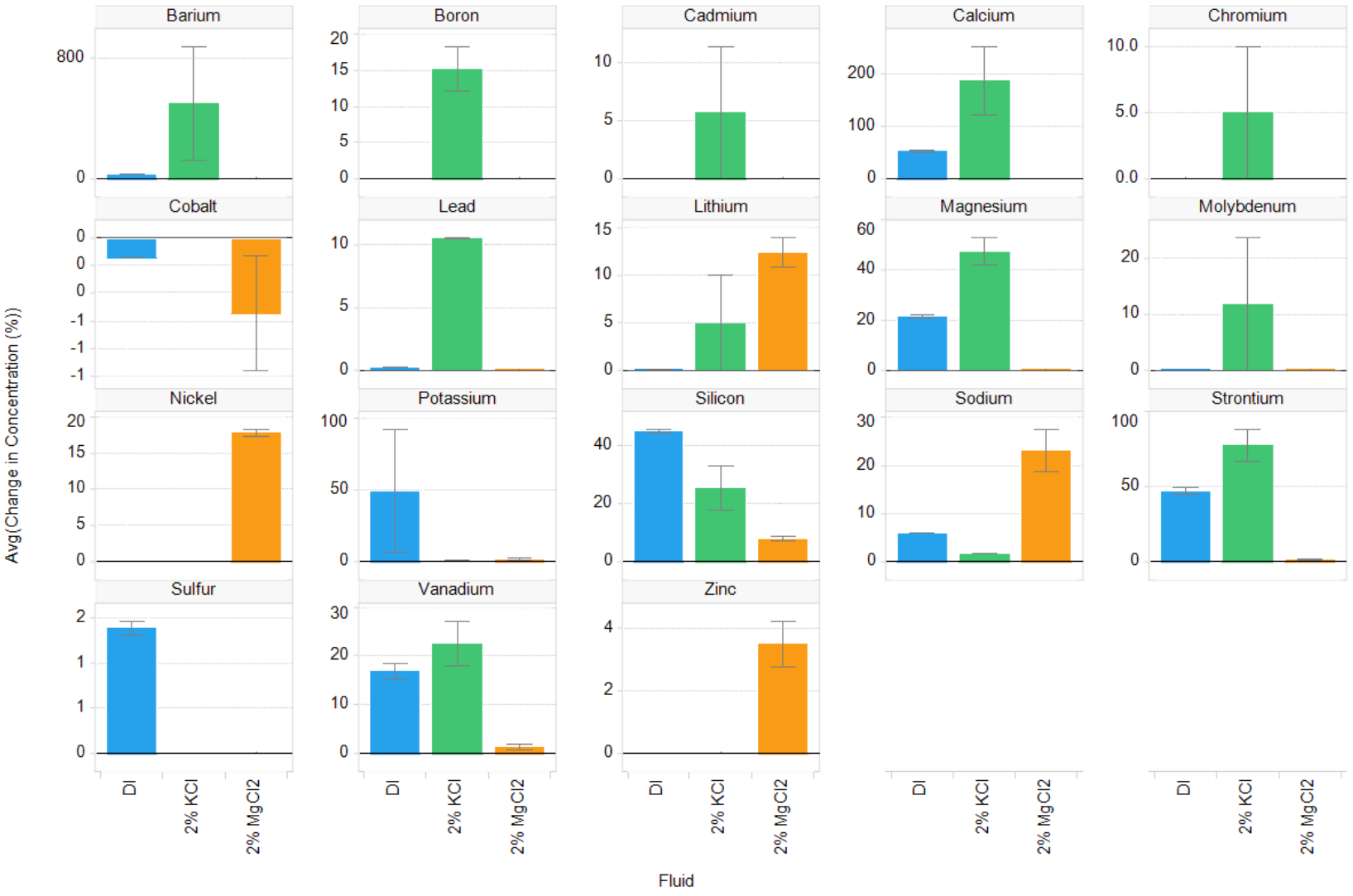


Figure 4.15: Element concentration change (%) averaged per fluid type obtained from the beakers containing proppant.

### 4.3.1 Effect of Fluid Saturation in Wave Velocities

The compressional ($V_p$) and shear ($V_s$) wave velocities of the core plugs pre- and post-treatment are shown in Figure 4.16. The uncertainty associated with the selection of the arrival time of the acoustic waves is assumed to be 1% for P-waves and 5% for S-waves. Both compressional and shear wave velocities decrease after saturation with the fluids, where the sharpest reduction is observed on the S-waves. Tutuncu et al. (2016) state that these acoustic property changes will strongly impact the velocity models in microseismic data analysis, thus, reducing the precision of the epicenter location. They emphasize that the formation frictional characteristics as well as the compressional, shear, and tensile fracture characteristics and fluid composition will be altered with the associated fluid pressure and geochemical changes.

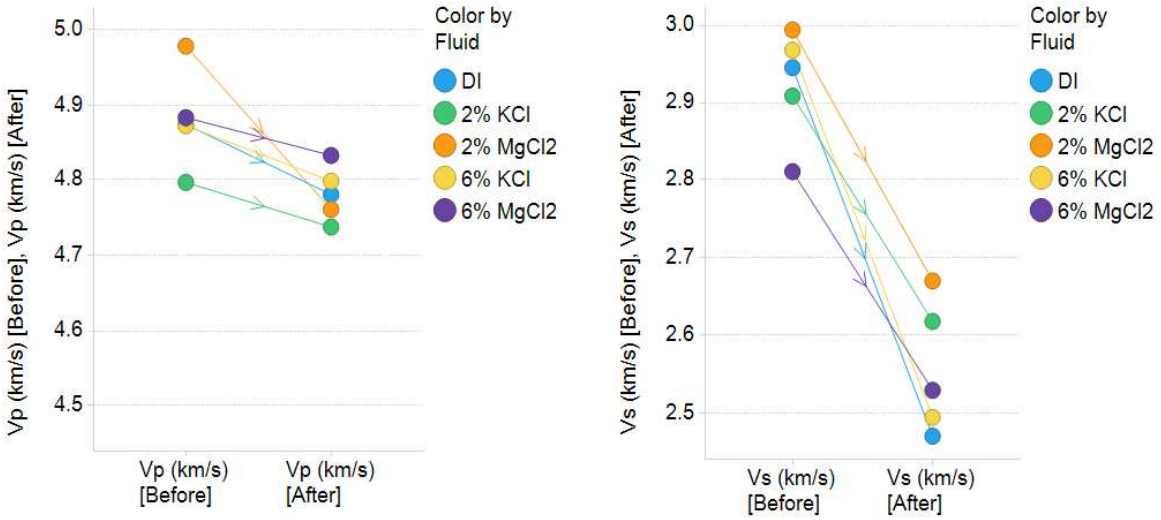


Figure 4.16: Ultrasonic P- (left) and S-wave (right) velocities measured before and after saturating the core sample with various fluids for 30 days.

### 4.3.2 Effect of Fluid Saturation in Dynamic Mechanical Properties

Previous studies have shown that only a small degree of water saturation is needed to mobilize the water weakening effect (Schroeder et al. 1998). Compressional and shear wave velocities, along with the density, provide sufficient information to determine dynamic elastic moduli when assuming isotropy (Simmons and Brace 1965). The changes in the dynamic

geomechanical properties of the rock were calculated by subtracting the initial value to the post-treatment value and dividing it by the initial value. This normalization process provided the percentage change of dynamic Young's modulus and Poisson's ratio that are shown in Figure 4.17. The figure also displays the errors bars driven by the uncertainty in acoustic wave arrival time.

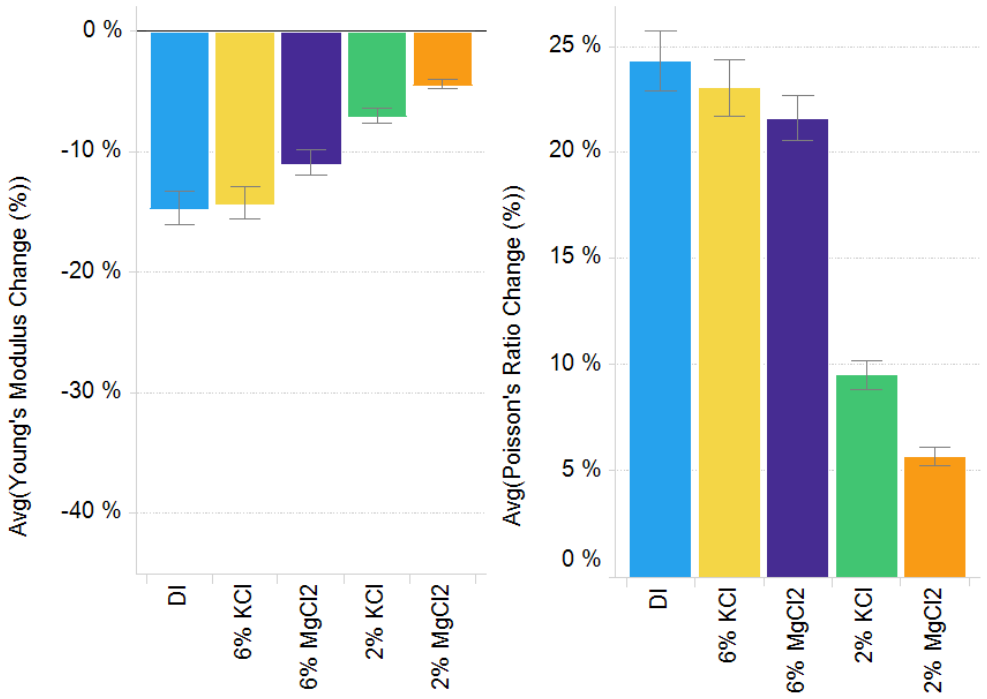


Figure 4.17: Post-treatment change in dynamic Young's modulus (left) and Poisson's ratio (right) per fluid type.

As expected, distilled water has a major impact on the loss of stiffness in the rock. Two-percent brines resulted in the smallest change in stiffness; additionally, 2% $MgCl_2$ had the smallest effect of all the fluids. Unexpectedly, 6% brines yielded values between those obtained from distilled water and 2% brines contrary to the expectation that fluids with higher salinity would have the smallest impact on the elastic moduli. The similarity of the 6%-brine measurements to distilled water measurements suggest full, uniform saturation was not accomplished for these samples. In addition, these experiments were performed at room temperature which may cause the salt ions to cluster and create imperfect crystallites.

These solid bridges may act as a semi-permeable membrane for nano-size pore throats and affect fluid flow characteristics. In such a case, the early blockage of the salt molecules can cause the fluid filtrating to have a lower concentration of the salt alternating the saturation behavior. While this scenario may explain the observation for 6% brines lagging behind 2% brines, no salt precipitation was observed within the saturation cell.

Static measurements were performed using a uniaxial stress load frame to confirm the behavior observed on the dynamic measurements. In order to calculate the static Young's modulus, a stress versus strain plot was generated for each core as shown in Figure 4.18. Each graph yields a very strong fit to a second order polynomial curve ($y = ax^2 + bx + c$). In this case, the derivative of the curve is $2ax + b$ and the slope of that linear function represents the Young's modulus of the sample.

The percentage change in Young's modulus was obtained using the same method as the dynamic moduli; results are shown in Figure 4.19. Geomechanical measurements of static moduli indicate a formation-softening trend similar to the dynamic measurements. Distilled water shows the greatest change in Young's modulus followed by the 6% and 2% brines, respectively. When comparing these geomechanical changes to the chemical elements dissolution, silicon and iron dissolution in the fluid have the same trend as the geomechanical properties changes. The largest changes are observed in the cores saturated with distilled water, followed by 2% KCl, then 2% $MgCl_2$. Therefore, these elements may be used as a proxy for rock strength loss.

A relationship between dynamic Young's modulus and static Young's of the samples is shown in Figure 4.20. The correlation shows how values of both moduli are affected by the different conditions under which the tests are performed, static measurements causing deformation of the sample and dynamic measurements being a non-destructive test. Loading uniaxial tests can cause the closing of microfractures which leads to the growth of deformation, and consequently, to the decreasing of the elastic constant (Mockovčiaková and Pandula 2003).

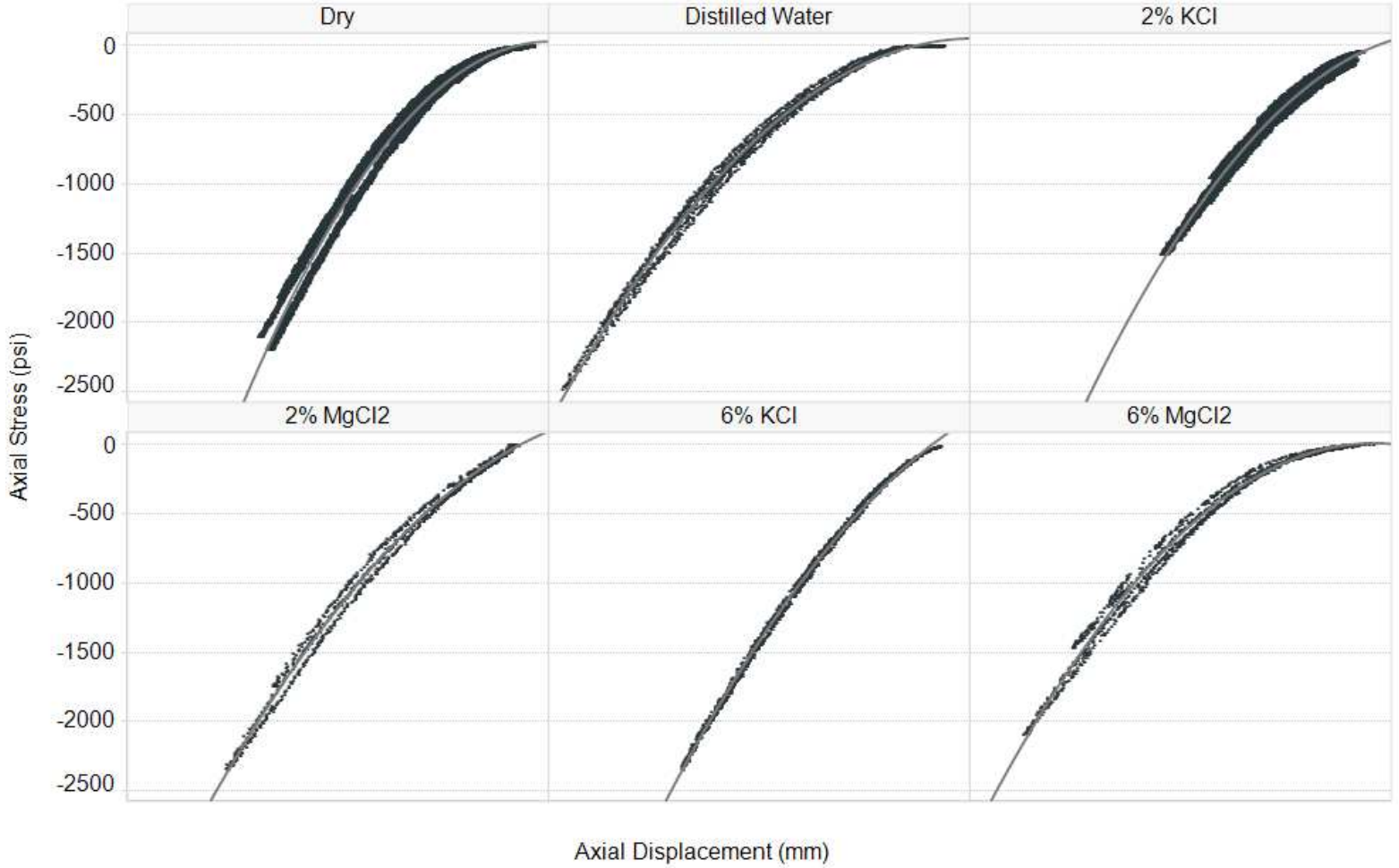


Figure 4.18: Axial stress versus axial deformation per fluid type obtained during the uniaxial stress test used to calculate the static Young's modulus.

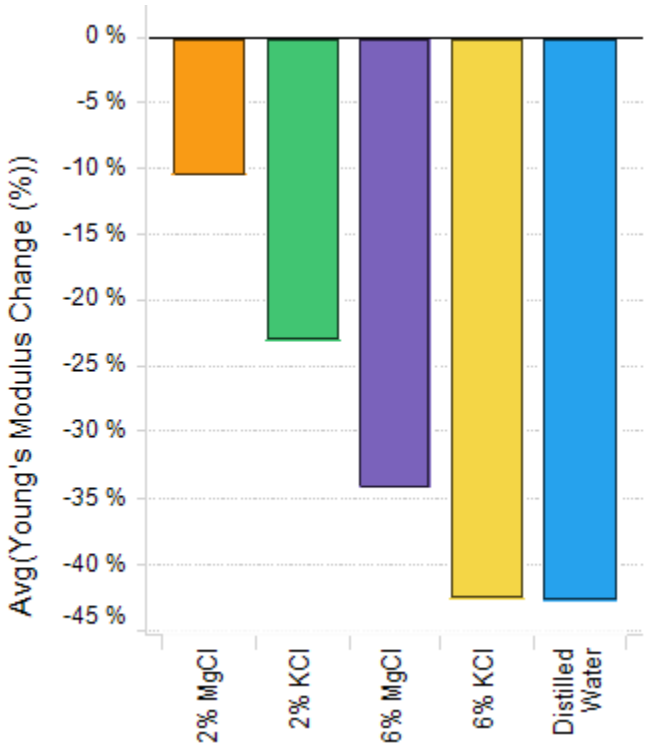


Figure 4.19: Post-treatment change in static Young's modulus per fluid type.

## 4.4 Chemical and Dynamic Moduli Monitoring under Triaxial Stress Conditions

Chemical and mechanical changes were monitored on a fractured and propped core to understand the formation, proppant, and fluid interactions under reservoir conditions using a triaxial stress test assembly. To achieve this, fluid chemistry, dynamic and static moduli, and conductivity measurements were performed.

### 4.4.1 Effect of Fluid Saturation and Stress Wave Velocities

Cores were saturated with distilled water as the first step for triaxial stress testing. During this process, the pressure in the system was increased while maintaining a constant effective stress of 100 psi with exception of the first pressure step where the effective stress was 50 psi and the rock was still dry since the pore pressure was yet to be introduced. The pressure at each step was maintained until the volume change in the system was negligible

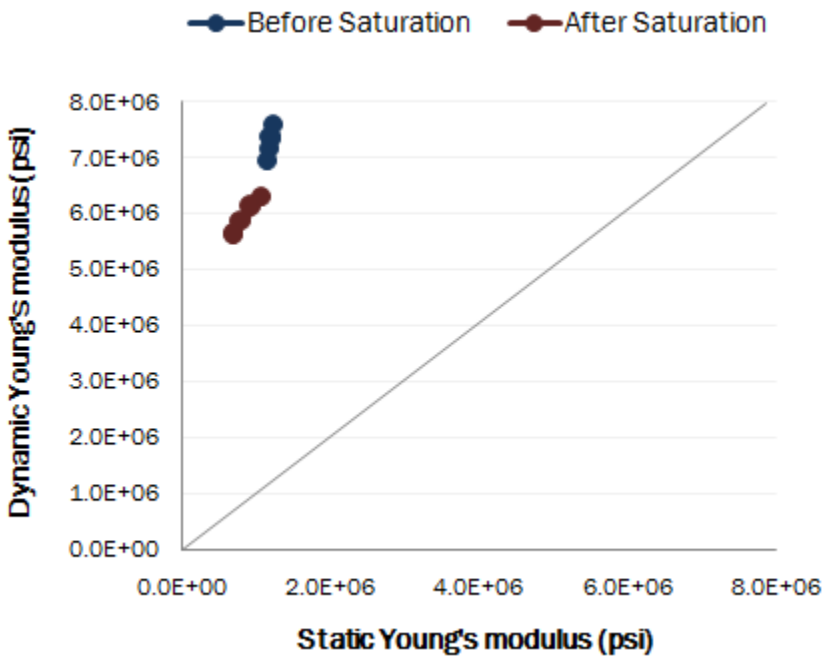


Figure 4.20: Relationship between dynamic and static Young's modulus for samples before and after saturation.

and the total saturation time was 15 days.

Ultrasonic P- and S-wave velocities acquired at each effective stress, pore pressure step, and time during this process are shown in Figure 4.21. The sample was placed in the cell in a way that the S-wave polarization was normal to the proppant filled fracture. Both P- and S-wave velocities increased with increasing pressure and effective stress. The greatest change is observed for the first step of the experiment where the effective stress was increased and the rock was exposed to the saturating fluid for the first time. The increasing values suggest that wave propagation in the sample at this stage of the experiment is affected more by the pressure changes rather than the saturation of the rock with the fluid. The saturation effective stress was kept at low level, approximately 100 psi, to prevent any deformation in the rock.

The flow test was initiated once the saturation process was completed. Ultrasonic P- and S-wave velocities recorded during the triaxial flow test at each pressure step are presented

in Figure 4.22. In this specific experiment, the P-wave velocities show an increasing trend with the effective stress, while the S-waves are rather constant or increasing slowly. This behavior can be related to the natural fractures closing and the propped fracture width being reduced creating a denser medium for improved P-wave transmission. The change in P-wave behavior due to the presence of a single or multiple fractures was reported by Tutuncu et al. (1993) and Pyrak-Nolte et al. (1990). They reported that the P-wave spectral amplitudes for fractured samples are much lower than those for intact samples at the same stress levels, indicating that higher energy loss occurred in fractured samples.

### 4.4.2 Propped Fracture Conductivity Tests

Fracture conductivity was calculated using the recorded flow rate and pressure gradient at each effective stress during the flow test using Equation 3.8. The calculated apparent fracture conductivity was then plotted against the fluid rate as shown in Figure 4.23. The departure from a straight-line fit shows the presence of non-Darcy flow regime. This non-linearity is accounted for in Forchheimer's method presented in Chapter II. The reciprocal apparent conductivity determined from Darcy's Law is plotted against the fluid rate, and a linear relationship is obtained as displayed in Figure 4.24. Then, the conductivity is determined by calculating the inverse of the intercept of the y-axis.

Long-term fracture conductivity was calculated at each pressure step as shown in Figure 4.25. The error bars indicate the uncertainty in the values related to the flow rate variations during the test and the variation in the fracture length related to the rough surface. The sharpest decline in conductivity is observed at the lower pressure regimes (50-1500 psi), while the higher pressure steps show more stable values. Although the same behavior is observed on the Vaca Muerta samples studied by Hegazy (2016), those samples have steeper conductivity decay. This can be explained by the proppant embedment observed in the samples shown in Figure 4.26. The high clay content present in the rock corresponds to the high embedment observed in the sample (Hegazy 2016). Conversely, Niobrara samples showed little-to-no proppant embedment in the fracture wall (Figure 4.27). This may be due

to the high strength of the calcite-filled fracture where the proppant is placed.

### 4.4.3 Effect of Stress and Flow on Fluid Chemical Interactions

The results obtained from the ICP-AES analysis of the daily fluid samples taken from the triaxial cell flow test are reported in Figure 4.28. The fluid sample results indicate that highest physicochemical dissolution of most of the elements is observed at the early contact of the fluid with the rock. The element dissolution then decreases as a function of time at the same pressure regime stabilizing when equilibrium is reached until the pressure is increased and the dissolution increases with it. This observation is a result of how the solubility of the chemical elements increases with increasing pressure.

Calcium shows the highest concentration change and a continuous dissolution in the effluent fluid. This behavior is correlated to the rock mineral composition since the core was fractured along the calcite-filled natural fracture. This happens even when the fluid pH is greater than 8 and increasing with time and pressure as shown in Figure 4.29. Lessenger et al. (2016) suggests this may due to the ferroan nature of authigenic calcite. Lessenger et al. (2016) highlight that although clays such as illite and kaolinite have been shown to cause fluid sensitivity problems, any unstable mineral can cause problems. The formation of carbonate scales due to the pressure drop in the perforations can lead to matrix scale. This effect is overridden near wellhead pressures due to lower temperatures thus reducing scale formation within the tubing (Crabtree et al. 1999). This effect could be misleading to the scale precipitation happening downhole and potentially plugging the fracture permeability near the wellbore.

The elements showing the highest dissolution after calcite are sulfur, sodium, potassium, magnesium and silicon. Again, this appears to be related to the mineralogy present in the fracture wall. The concentrations observed during this test are lower than the ones obtained from the crushed rock, as expected, due to the higher surface area of the crushed rock allowing more fluid interactions.

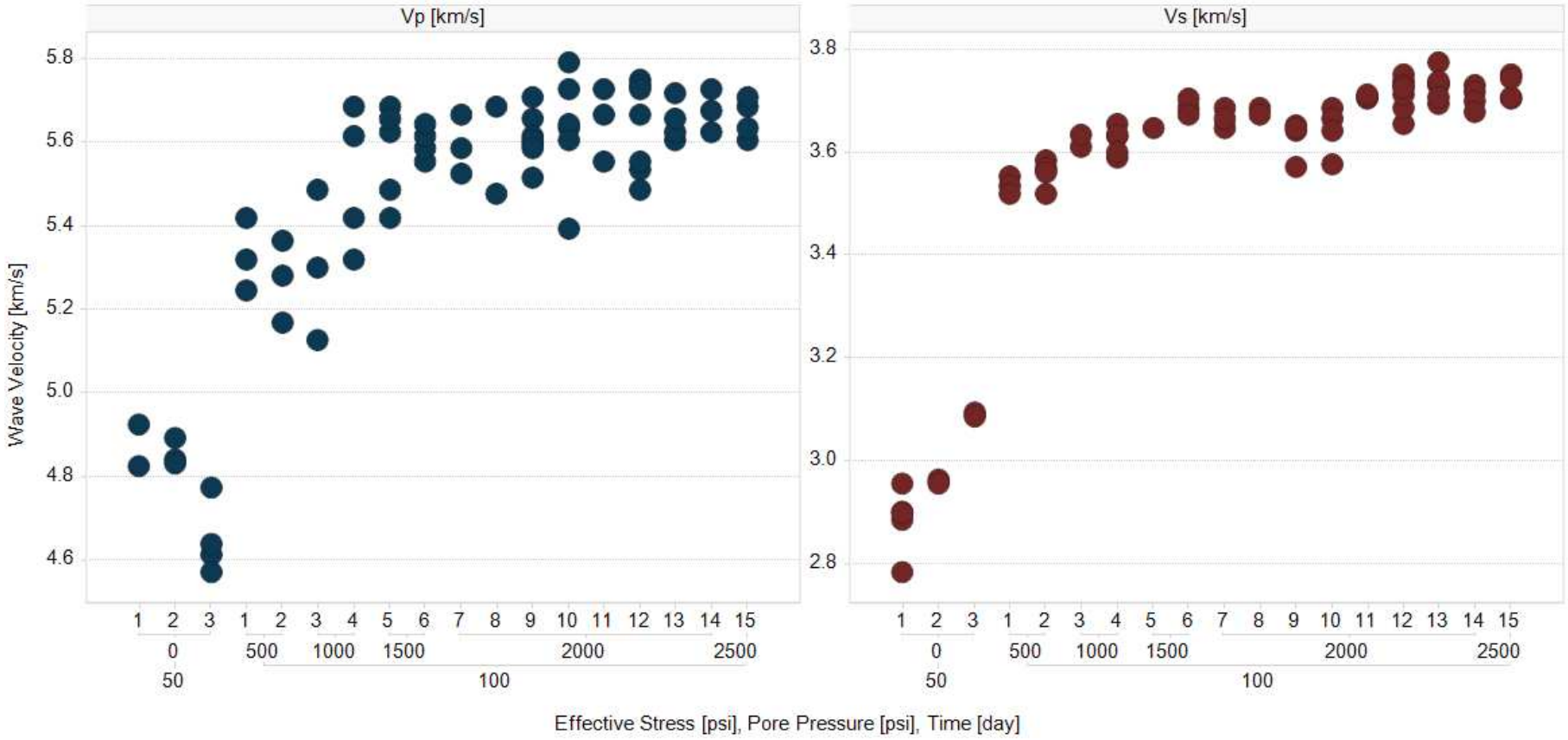


Figure 4.21: Ultrasonic P- and S-wave velocities recorded as a function of effective stress, pore pressure and time during the distilled water saturation in the triaxial.

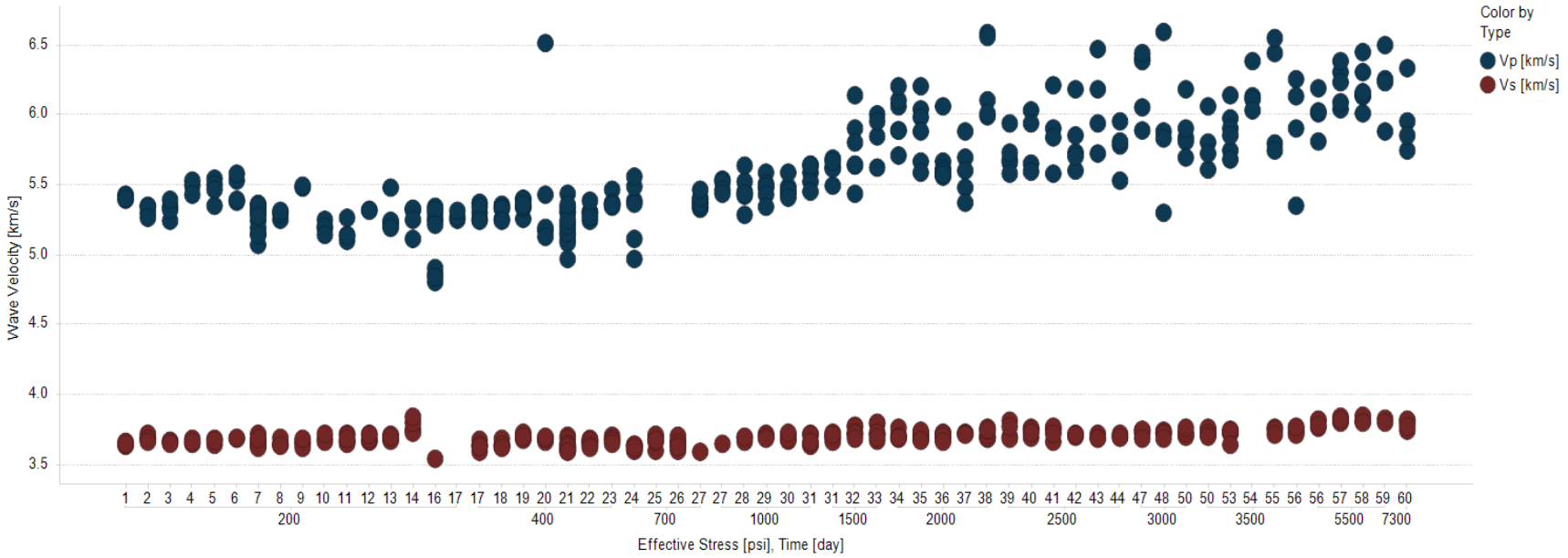


Figure 4.22: Ultrasonic P- and S-wave velocities recorded during the triaxial flow test at each effective stress and time step.

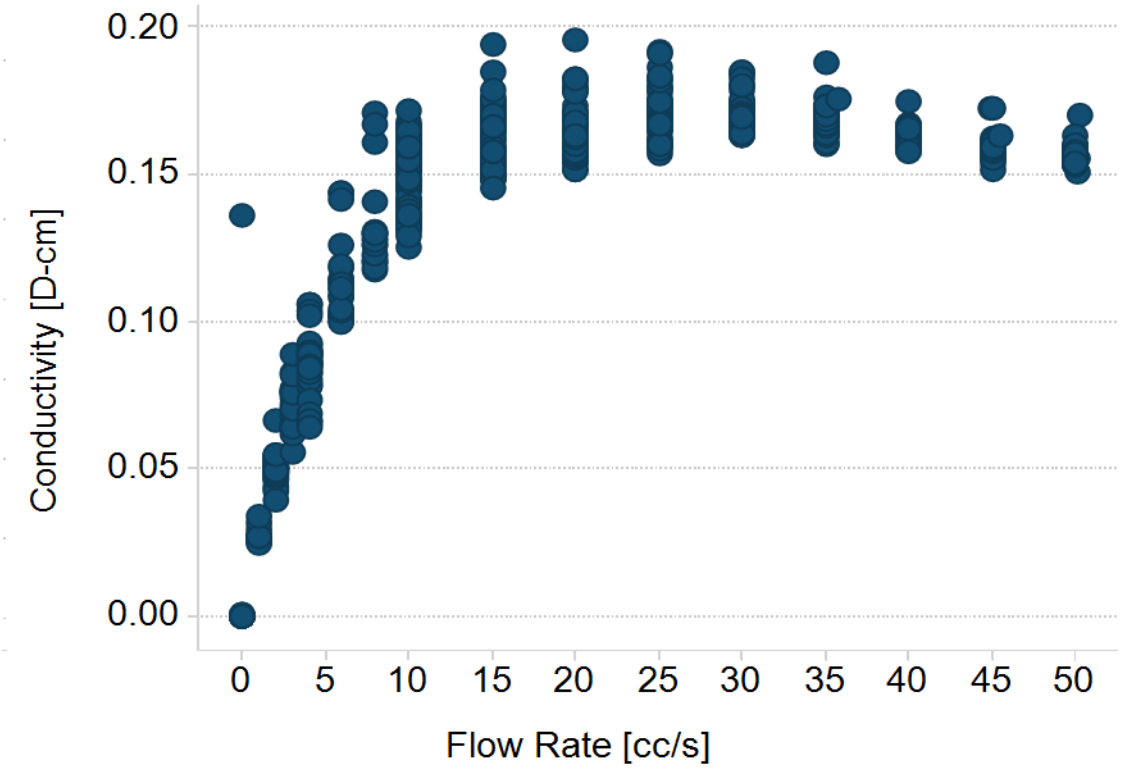


Figure 4.23: Apparent fracture permeability determined from Darcy's Law and fluid rate in the fracture.

There are no particular elements that could be specifically isolated from the dissolution reaction of the distilled water with the proppant. This is due to the fact that the fluid samples obtained from the distilled water and proppant breakers only show significant changes in potassium and silicon concentrations, which are also observed for the fluid samples from the rock alone. The temperature in the system could be a limitation on this test since the chemical reactions taking place within the proppant have only been observed on previous experimental studies performed at high temperatures (200-300°F) (Osholake et al. 2011; Raysoni and Weaver 2012; Weaver et al. 2007; Weaver and Rickman 2010).

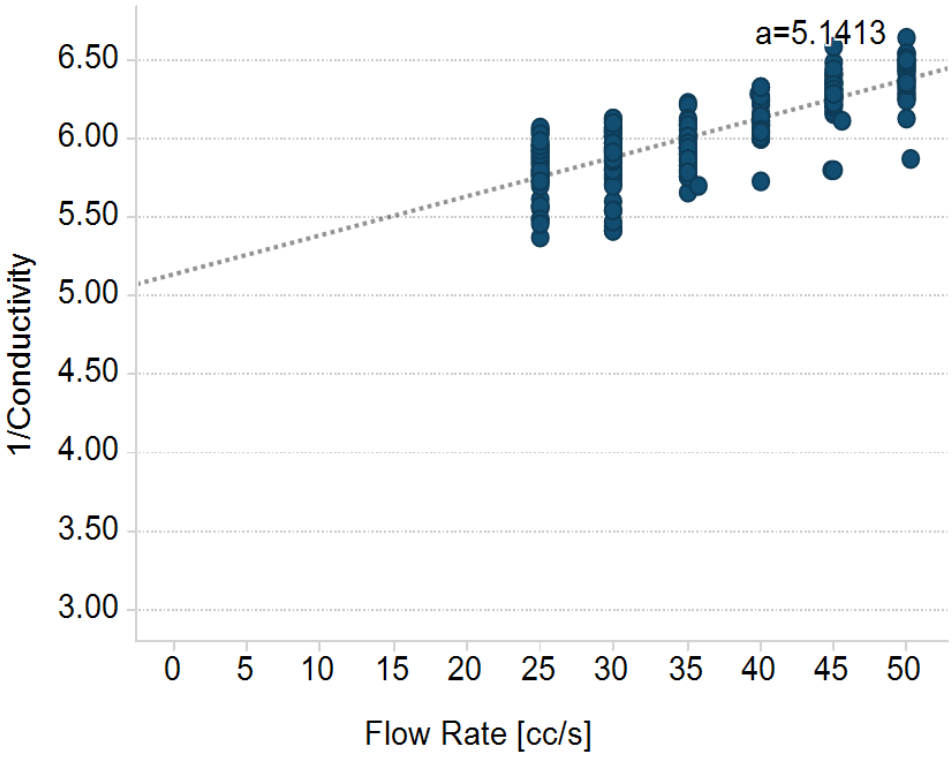


Figure 4.24: Determination of the absolute fracture permeability based on Forchheimer's Equation.

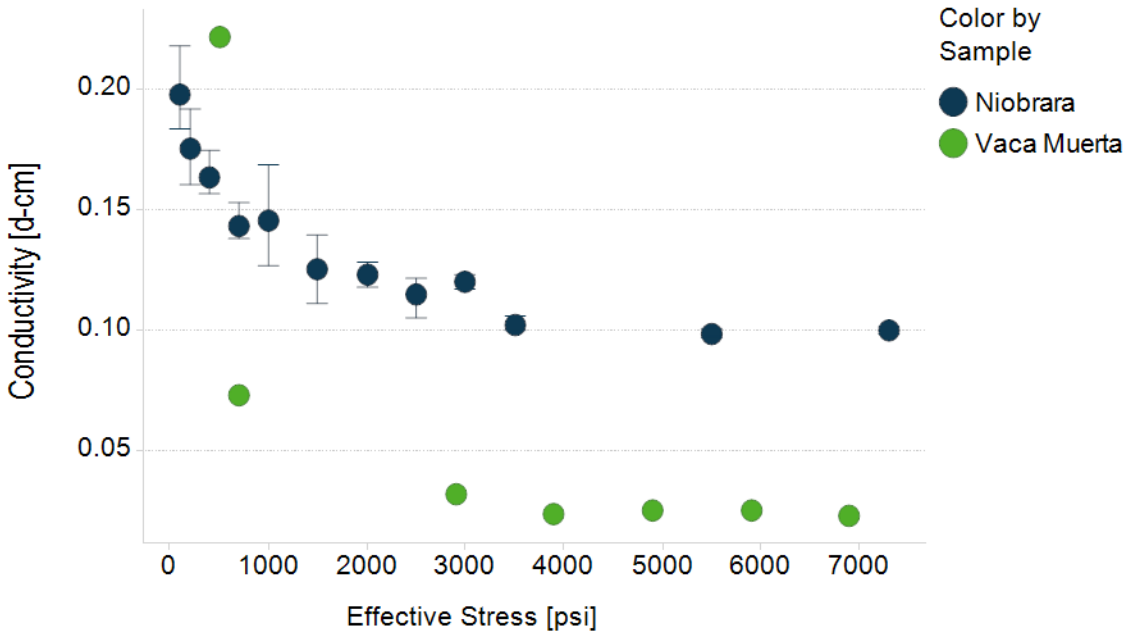


Figure 4.25: Effective stress dependence of the proppant filled fracture permeability.

Figure 4.26: Vaca Muerta core sample showing the high level of indentation in the rock from proppant embedment after the triaxial stress conductivity experiment.

Figure 4.27: Niobrara core sample shown little to none proppant embedment after the triaxial stress conductivity experiment.

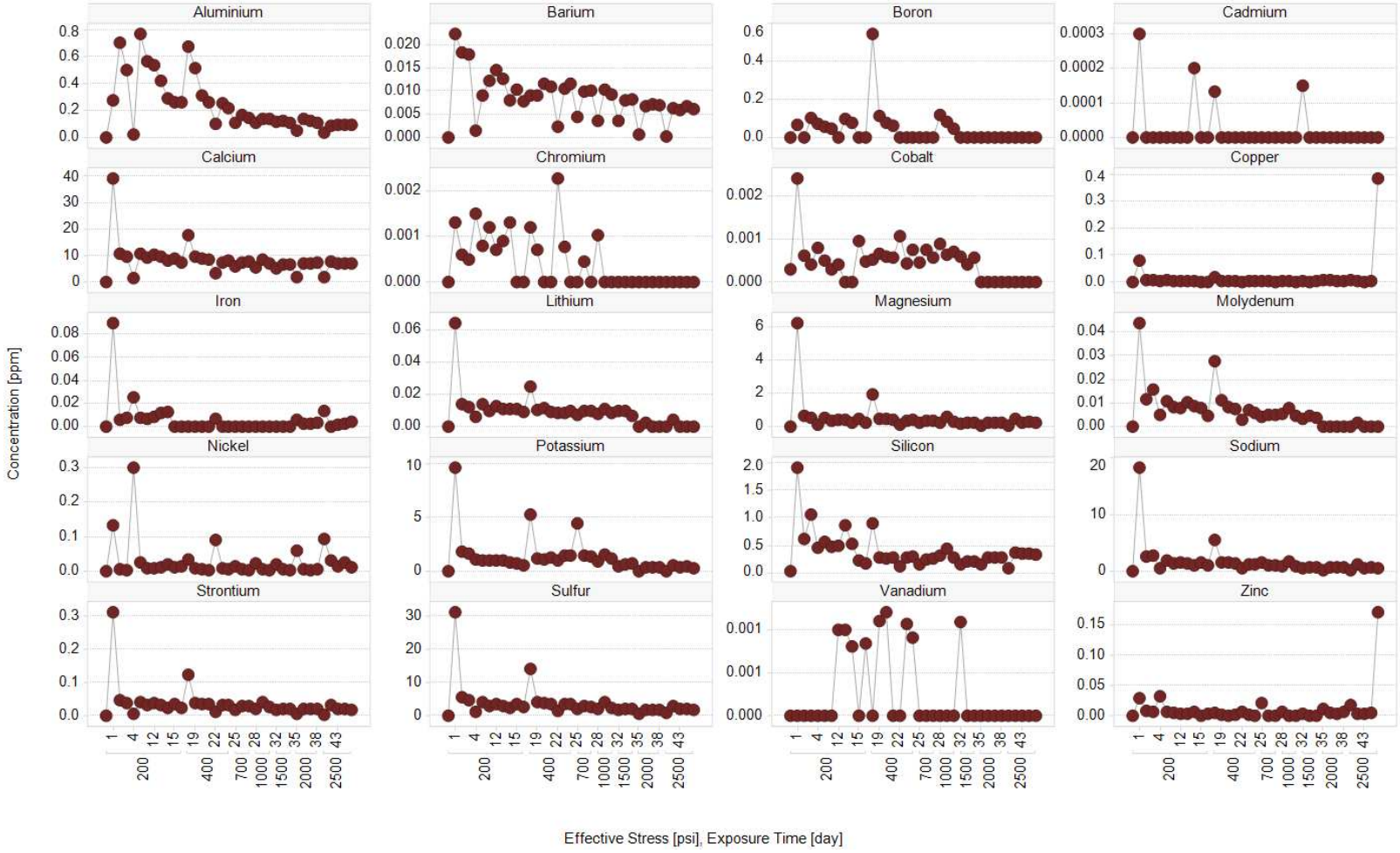


Figure 4.28: Concentration of various elements versus exposure time and their respective effective stress for fluid samples obtained from the triaxial flow test.

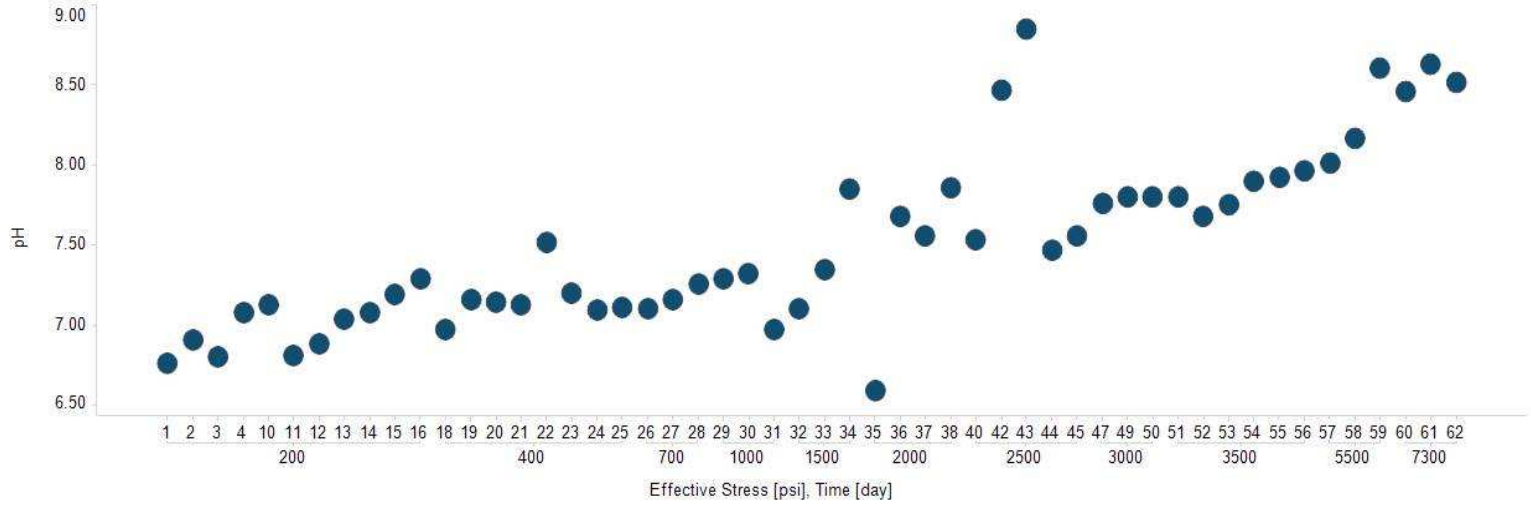


Figure 4.29: pH of the triaxial cell effluent fluid versus exposure time and its corresponding effective stress.

# CHAPTER 5

# CONCLUSIONS AND RECOMMENDATION

The role of fluid composition on changes in rock formation properties has been investigated. Fluid chemical interactions, mechanical and acoustic properties, and fracture conductivity of the Niobrara Formation have been evaluated under reservoir stress conditions using a coupled triaxial apparatus. The following conclusions have been obtained from the investigative study discussed in this research:

- Each fluid composition yields unique interactions with the rock samples. Distilled water is more prone to dissolve elements related to the strength of the rock whereas 2% brines, especially 2% KCl, dissolve elements that could be the source of scales, fines migration,other types of undesired precipitations, and elements related to organic matter.

- Laboratory measurements of ultrasonic wave velocities through saturated rock indicate that both P-wave and S-wave velocities are affected by the presence of fluid and the fluid-rock interactions. As a result of these interactions, the dynamic and static Young's moduli decrease up to 15% and 42%, respectively, and the dynamic Poisson's ratio increased up to 24% when the rock was saturated with distilled water. The smallest geomechanical changes were observed in core plugs saturated with 2% brines. Two-percent $MgCl_2$ was found to be the least chemically reactive with the Niobrara samples and the fluid with causing the lowest geomechanical changes. This confirms that these changes are related to not only the fluid type, but also the type of cation present (monovalent or divalent) and their concentration used in saturating the core samples.

- Comparison of dynamic and static elastic moduli and fluid chemistry data pre and post- treatment indicate that there is a correlation between the formation softening

and the chemical interactions taking place between the fluids used in this study and the Niobrara rock. The FE-SEM images further strengthen this interpretation. Iron ($Fe^+$) and silicon ($Si^+$) dissolution may be used as a proxy for predicting the variations in stiffness in the rock, showing that matrix bulk mineralogy and mineral distribution play a critical role in water surface interactions.

- Stress-dependent, long-term fracture conductivity shows the sharpest decline in the early stages of the experiment. The associated fluid sample analysis indicates that the highest physicochemical dissolution of most of the elements is happening at the early contact of the fluid with the rock. A comparison with the conductivity measurements performed on the Vaca Muerta samples shows a similar behavior, yet a steeper initial decay than the observed in the Niobrara samples. The difference observed between the two samples is related to the mineralogy of the formation and the high proppant embedment observed in the Vaca Muerta samples. The lack of proppant embedment in the Niobrara samples is attributed to the high strength of the calcite-filled fracture where the proppant is placed. This illustrates how conductivity damage effects vary not only with mineralogy of the rock, but also with the mineral distribution and where the fracture is located within the formation.

- Calcium ($Ca^+$) dissolution can take place in the rock when high pH fluids are used. The highest physicochemical dissolution is observed at the early contact of the fluid with the rock and is later enhanced by the pressure increase in the system. In general, mineral dissolution decreases with exposure time and stabilizes when equilibrium is reached.

- Long periods of time are required to determine the compatibility of the fluids in a triaxial cell at reservoir conditions. A more simple approach can be followed by mixing crushed core and proppant samples with various fluid formulations to understand the potential dissolution of fundamental elements in the formation. This can improve

fluid selection, which could help prevent the formation stiffness reduction and/or the precipitation or migration of fines.

In future studies, additional fluid compositions could be tested including other solutes or in combinations, as well as testing various additives used in fracturing operations in the field like friction reducer and biocide. This could help improve the fluid selection and design of hydraulic fracturing jobs in the Niobrara Formation. Similar experiments in other shale formations with different mineralogy (clay-rich or quartz-rich) will also provide deeper insight into compatible fracturing fluid selection and use for well integrity and longer production life. It would be helpful to also include a measurement of the electrical conductivity of the fluid and complex resistivity of the core samples during the triaxial measurements to allow monitoring of the changes in solute concentration and formation resistivity as a function of time. Future work could be also focused on looking at acoustic waves related to microseismic events in the laboratory and how they are influenced by the presence of different fracturing fluid compositions in the rock.

# REFERENCES CITED


Akrad, O. M., Miskimins, J. L., and Prasad, M. 2011. The Effects of Fracturing Fluids on Shale Rock Mechanical Properties and Proppant Embedment. Presented at the SPE Annual Technical Conference and Exhibition, 30 October-2 November, Denver, Colorado, 30 October-2 November. SPE-146658-MS. https://doi.org/10.2118/146658-MS.

Al-Sadhan, N. 2014. *Prediction of Short-Term and Long-Term Baseline Conductivity Degradation for Proppants of Different Types and Sizes.* Phd thesis, Colorado School of Mines, Golden, Colorado (May 2014).

Alramahi, B. and Sundberg, M. 2012. Proppant Embedment and Conductivity of Hydraulic Fractures in Shales. Presented at the 46th U.S. Rock Mechanics/Geomechanics Symposium, 24-27 June, Chicago, Illinois. ARMA-2012-291.

Barree, R. D., Cox, S. A., Barree, V. L., and Conway, M. W. 2003. Realistic Assessment of Proppant Pack Conductivity for Material Selection. Presented at the SPE Annual Technical Conference and Exhibition, Denver, Colorado, 5-8 October. SPE-84306-MS. https://doi.org/10.2118/84306-MS.

Boss, B. and Fredeen, K. J. 2004. *Concepts, Instrumentation and Techniques in Inductively Coupled Plasma Optical Emission Spectrometry.* Shelton, CT: PerkinElmer, Inc., 3rd edition.

Britt, L. K. and Schoeffler, J. 2009. The Geomechanics of a Shale Play: What Makes a Shale Prospective. Presented at the SPE Eastern Regional Meeting, Charleston, West Virginia, 23-25 September. SPE-125525-MS. http://doi.org/10.2118/125525-ms.

Collin, M. D. 2012. *Natural Fractures in The Niobrara Formation, Boulder to Lyons, Colorado.* MS Thesis, Colorado School of Mines, Golden, Colorado (March, 2012).

Corapcioglu, H., Miskimins, J., and Prasad, M. 2014. Fracturing Fluid Effects on Young's Modulus and Embedment in the Niobrara Formation. Presented at the SPE Annual Technical Conference and Exhibition, Amsterdam, The Netherlands, 27-29 October. SPE-170835-MS. http://doi.org/10.2118/170835-ms.

Crabtree, M., Eslinger, D., Fletcher, P., Miller, M., Johnson, A., and King, G. 1999. Fighting Scale—Removal and Prevention. *Schlumberger Oilfield Review*, **11**(3).

Davis, G. H., Reynolds, S. J., and Kluth, C. F. 1996. *Structural Geology of Rocks and Regions.* New York: John Wiley, 2nd edition.

Dong, T., Harris, N. B., Ayranci, K., and Yang, S. 2007. *The Impact of Rock Composition on Geomechanical Properties of a Shale Formation: Middle and Upper Devonian Horn River Group Shale, Northeast British Columbia, Canada*, volume 101 (2): 177–204. AAPG Bulletin. https://doi.org/10.1306/07251615199.

Duenckel, R. J., Conway, M. W., Eldred, B., and Vincent, M. C. 2011. Proppant diagenesis - integrated analyses provide new insights into origin, occurrence, and implications for proppant performance. *SPE Production & Operations*, **27**(2). SPE-139875-PA. https://doi.org/10.2118/139875-PA.

ElGhonimy, R. S. 2015. *Petrophysics, Geochemistry, Mineralogy, and Storage Capacity of the Niobrara Formation in the Aristocrat PC H11-07 Core, Wattenberg Field, Denver Basin, Colorado.* MS Thesis, Colorado School of Mines, Golden, Colorado (May, 2017).

Ewalds, H. L. and Wanhill, R. J. H. 1984. *Fracture Mechanics*. London : E. Arnold ; Delft, Netherlands : Delftse Uitgevers Maatschappij.

Finn, T. M. and Johnson, R. C. 2005. *Niobrara Total Petroleum System in the southwestern Wyoming province, in Petroleum Systems and Geologic Assessment of Oil and Gas in the Southwestern Wyoming Province, Wyoming, Colorado, and Utah.* U.S. Geological Survey Digital Data Series DDS– 69–D.

Fjar, E., Holt, R., Raaen, A., Risnes, R., and Horsrud, P. 2008. *Petroleum Related Rock Mechanics*, volume 53. Amsterdam, The Netherlands: Elsevier Science, 2nd edition.

Forchheimer, P. 1914. *Hydraulik*. Berlin, Germany: Teubner.

Freeman, E. R., Anschutz, D. A., Rickards, A. R., and Callanan, M. J. 2009. Modified API/ISO Crush Tests With a Liquid-Saturated Proppant Under Pressure Incorporating Temperature, Time, and Cyclic Loading: What Does It Tell Us? Presented at the SPE Hydraulic Fracturing Technology Conference, The Woodlands, Texas, 19-21 January. SPE-118929-MS. https://doi.org/10.2118/118929-MS.

Ghosh, S., Rai, C. S., Sondergeld, C. H., and Larese, R. E. 2014. Experimental Investigation of Proppant Diagenesis. Presented at the SPE/CSUR Unconventional Resources Conference – Canada, Calgary, Alberta, Canada, 30 September–2 October. SPE-171604-MS. https://doi.org/10.2118/171604-MS.

Gong, H. 2008. Elemental Analyses by ICP-AES. Penn State. http://www.unn.ru/chem/ism/files/applecture21(2).pdf (accessed 12 March 2017).

Graf, G. J. 2008. *Mineralogical and Geochemical Changes Associated with Sulfide and Silicate Weathering in Natural Alteration Scars, Taos County, New Mexico.* MS Thesis, New Mexico Institute of Mining and Technology (May, 2008).

Hegazy, D. A. 2016. *An Experimental Study to Investigate the Effects of in Situ Stress State and Rock-Fluid Interactions on Propped Fracture Conductivity in the Vaca Muerta Formation.* MS Thesis, Colorado School of Mines, Golden, Colorado (January, 2017).

Hyne, N. J. 2012. *Nontechnical Guide to Petroleum Geology, Exploration, Drilling & Production.* Tulsa, Oklahoma: PennWell Corporation, 3rd edition.

Katsuki, D., Gutierrez, M., and Tutuncu, A. 2014. Effects of Stress and Intrinsic Anisotropy on the Development of Shear Fractures in Shale Formations. Presented at the 48th U.S. Rock Mechanics/Geomechanics Symposium, Minneapolis, Minnesota, 1-4 June. ARMA-2014-7502.

King, G. E. 2010. Thirty Years of Gas Shale Fracturing: What Have We Learned? Presented at the SPE Annual Technical Conference and Exhibition, Florence, Italy, 19-22 September. SPE-133456-MS. https://doi.org/10.2118/133456-MS.

Kullman, J. 2011. The Complicated World of Proppant Selection. Http:// images.sdsmt.edu/learn/speakerpresentations/Kullman.pdf.

Lacy, L., Rickards, A., and Bilden, D. 1998. Fracture Width and Embedment Testing in Soft Reservoir Sandstone. *SPE Drilling & Completion*, **13**(1). SPE-36421-PA. https://doi.org/10.2118/36421-PA.

LaFollette, R. F. and Carman, P. S. 2010. Proppant Diagenesis: Results So Far. Presented at the SPE Unconventional Gas Conference, Pittsburgh, Pennsylvania, 23-25 February. SPE-131782-MS. https://doi.org/10.2118/131782-MS.

LaFollette, R. F. and Carman, P. S. 2011. Long Term Stability of Proppants Exposed To Harsh Shale Reservoir Conditions. SPE Hydraulic Fracturing Technology Conference, The Woodlands, Texas, 24-26 January. SPE-140110-MS. https://doi.org/10.2118/140110-MS.

Lee, D., Elsworth, D., Yasuhara, H., Weaver, J., and Rickman, R. 2009. An Evaluation of the Effects of Fracture Diagenesis On Fracture Treatments: Modeled Response. 43rd U.S. Rock Mechanics Symposium & 4th U.S. - Canada Rock Mechanics Symposium, Asheville, North Carolina, 28 June-1 July. ARMA-09-104.

Lessenger, M., Sullivan, B., Woolf, K., and Burton, D. 2016. *Fluid Sensitivity Analyses in Tight Sandstones—When Rocks Behave Badly in Imaging Unconventional Reservoir Pore Systems.* United Kingdom: AAPG Memoir 112.

Matthews, V. 2011. Colorado's New Oil Boom — The Niobrara. *CGS RockTalk*, **13**(1).

Mayer, L. M. 1993. *Organic Matter at the Sediment-Water Interface in Organic Geochemistry*, volume 11. Walpole, Maine: Plenum Press.

Mockovčiaková, A. and Pandula, B. 2003. Study of the Relation between the Static and Dynamic Moduli of Rocks. *CMS Metalurgija*, **42**. (1): 37-39.

Moghadasi, J., Jamialahmadi, M., Müller-Steinhagen, H., and Sharif, A. 2008. Formation Damage Due to Scale Formation in Porous Media Resulting From Water Injection. Presented at the SPE International Symposium and Exhibition on Formation Damage Control, Lafayette, Louisiana, 18-20 February. SPE-86524-MS. https://doi.org/10.2118/86524-MS.

Moon, V. and Jayawardane, J. 2004. Geomechanical and Geochemical Changes during Early Stages of Weathering of Karamu Basalt, New Zealand. *Engineering Geology*, **74**: 57–72. Http://doi.org/10.1016/j.enggeo.2004.02.002.

Murray, R., Miller, D., and Kryc, K. 2000. Analysis of Major and Trace Elements in Rocks, Sediments, and Interstitial Waters by Inductively Coupled Plasma-Atomic Emission Spectrometry (ICP-AES). ODP Technical Note 29. http://www-odp.tamu.edu/publications/tnotes/tn29/TNOTE$_2$9.$PDF(accessed23March2017)$.

Mustapha, H., de Langavant, L., and Giddins, M. A. 2015. Darcy and non-Darcy Flows in Fractured Gas Reservoirs. SPE Reservoir Characterisation and Simulation Conference and Exhibition, Abu Dhabi, UAE, 14-16 September. SPE-175596-MS. https://doi.org/10.2118/175596-MS.

Osholake, T. A., Wang, J. Y., and Ertekin, T. 2011. Factors Affecting Hydraulically Fractured Well Performances in the Marcellus Shale Gas Reservoirs. North American Unconventional Gas Conference and Exhibition, The Woodlands, Texas, 14-16 June. SPE-144076-MS. https://doi.org/10.2118/144076-MS.

Padin, A., Torcuk, M. A., Katsuki, D., Kazemi, H., and Tutuncu, A. N. 2016. Experimental and Theoretical Study of Water-Solute Transport in Organic-Rich Carbonate Mudrocks. SPE Annual Technical Conference and Exhibition, Dubai, UAE, 26-28 September. SPE-181585-MS. https://doi.org/10.2118/181585-MS.

Padín, A. 2016. *Experimental and Theoretical Study of Water and Solute Transport Mechanisms in Organic-Rich Carbonate Mudrocks*. PhD Thesis, Colorado School of Mines, Golden, Colorado (December, 2015).

Pagels, M. 2014. Rock/fluid interactions in unconventional reservoirs. Geoconvention 2014: FOCUS. http://www.geoconvention.com/archives/2014/070$_g$c2014$_r$ock$_f$luid$_i$nteractions$_i$n$_u$nconventional$_r$eservoir

Penny, G. 1987. An Evaluation of the Effects of Environmental Conditions and Fracturing Fluids Upon the Long-Term Conductivity of Proppants. SPE Annual Technical Conference and Exhibition, Dallas, Texas, 27-30 September. SPE-16900-MS. https://doi.org/10.2118/16900-MS.

Pyrak-Nolte, L. J., Myer, L. R., and Cook, N. G. W. 1990. Transmission of Seismic Waves Across Single Natural Fractures. *Journal of Geophysical Research: Solid Earth*, **95**(B6): 8617–8638. Http://dx. doi.org/10.1029/jb095ib06p08617.

Raysoni, N. and Weaver, J. D. 2012. Long-Term Proppant Performance. SPE International Symposium and Exhibition on Formation Damage Control, Lafayette, Louisiana, 15-17 February. SPE-150669-MS. https://doi.org/10.2118/150669-MS.

Reinicke, A. 2010. *Mechanical and Hydraulic Aspects of Rock–Proppant Systems—Laboratory Experiments and Modelling Approaches*. PhD Thesis, helmholtz centre potsdam, potsdam, germany (october, 2009).

Ritzma, H. R. 1955. *Guidebook to the Geology of Northwest Colorado*. Salt Lake City, Utah: Intermountain Association of Geologists 6th Annual Field Conference and Rocky Mountain Association of Geologists Annual Field Conference.

Scheuerman, R. F. and Bergersen, B. M. 1990. Injection-Water Salinity, Formation Pretreatment, and Well-Operations Fluid-Selection Guidelines. *Journal of Petroleum Technology*, **42**(7). SPE-18461-PA. https://doi.org/10.2118/18461-PA.

Schroeder, C., Bois, A.-P., Maury, V., and Halle, G. 1998. Water/Chalk (or Collapsible Soil) Interaction: Part II. Results of Tests Performed in Laboratory on Lixhe Chalk to Calibrate Water/Chalk Models. SPE/ISRM Rock Mechanics in Petroleum Engineering, Trondheim, Norway, 8-10 July. SPE-47587-MS. https://doi.org/10.2118/47587-MS.

Sharma, R., Prasad, M., Surve, G., and Katiyar, G. 2006. On the Applicability of Gassmann Model in Carbonates. 2006 SEG Annual Meeting, New Orleans, Louisiana, 1-6 October. SEG-2006-1866. http://dx.doi.org/10.1190/1.2369889.

Simmons, G. and Brace, W. F. 1965. Comparison of Static and Dynamic Measurements of Compressibility of Rocks. *Journal of Geophysical Research*, **70**(22): 5649–5656. Http://doi.org/10.1029/JZ070i022p05649.

Smith, M. B. and Shlyapobersky, J. 2000. *Fracturing Stimulation Book*. New York: John Wiley & Sons, 3rd edition.

Sonnenberg, S. A. 2012. The Niobrara Petroleum System, A Major Tight Resource Play Rocky Mountain Region. *AAPG Search and Discovery*, (10355): 32. Http://www.searchanddiscovery.com/pdfz/documents/2012/80206 sonnenberg/ndx$_s$*onnenberg.pdf.html*.

Sookprasong, P. A. 2010. In-Situ Closure Stress on Proppant in the Fracture: A Controversial New Thinking. Tight Gas Completions Conference, San Antonio, Texas, 2-3 November. SPE-136338-MS. https://doi.org/10.2118/136338-MS.

Stein, S. and Wysession. 2003. An introduction to seismology, earthquakes, and earth structure. *Oxford: Blackwell Science*. URL `http://dx.doi.org/10.1017/S0016756803318837`.

Terracina, J. M., Turner, J. M., Collins, D. H., and Spillars, S. 2010. Proppant Selection and Its Effect on the Results of Fracturing Treatments Performed in Shale Formations. SPE Annual Technical Conference and Exhibition, Florence, Italy,19-22 September. SPE-135502-MS. https://doi.org/10.2118/135502-MS.

Tribovillarda, N., Algeob, T. J., Lyonsc, T., and Riboulleaua, A. 2006. Trace Metals As Paleoredox and Paleoproductivity Proxies: An Update. *Chemical Geology*, **232**(1-2): 12–32. Http://doi.org/10.1016/j.chemgeo.2006.02.012.

Tutuncu, A. N., Katsuki, D., Bui, B. T., Padin, A., and McDowell, B. 2016. Coupling Geomechanics and Petrophysical Measurements for Production Enhancement in Organic-Rich Shales. Presented at the Unconventional Resources Technology Conference, San Antonio, Texas, 1-3 August. URTEC-2461986-MS. https://doi.org/10.15530/URTEC-2016-2461986.

Tutuncu, A. N., Podio, A. L., and Sharma, M. M. 1993. Effect of Macrofractures on Acoustic Properties of Rocks. SEG Annual Meeting, Washington, DC, USA, 26-30 September. SEG-1993-0765. http://dx.doi.org/10.1190/1.1822611.

van Golf-Racht, T. 1982. *Fundamentals of Fractured Reservoir Engineering*, volume 12. Oslo, Norway. Elsevier Science, 1st edition.

Vincelette, R. and Foster, N. 1992. *Geological Studies Relevant to Horizontal Drilling—Examples from Western North America: Rocky Mountain Association of Geologists Guidebook*.

Volk, L. J., Raible, C. J., Carroll, H. B., and Spears, J. S. 1981. Embedment of High Strength Proppant Into Low-Permeability Reservoir Rock. SPE/DOE Low Permeability Gas Reservoirs Symposium, Denver, Colorado, 27-29 May. SPE-9867-MS. https://doi.org/10.2118/9867-MS.

Weaver, J. D., Parker, M., van Batenburg, D. W., and Nguyen, P. D. 2007. Fracture-Related Diagenesis May Impact Conductivity. *SPE Journal*, **12**(03). Https://doi.org/10.2118/98236-PA.

Weaver, J. D. and Rickman, R. D. 2010. Productivity Impact from Geochemical Degradation of Hydraulic Fractures. SPE Deep Gas Conference and Exhibition, Manama, Bahrain, 24-26 January. SPE-130641-MS. https://doi.org/10.2118/130641-MS.

Zhang, J., Kamenov, A., Hill, A. D., and Zhu, D. 2014. Laboratory Measurement of Hydraulic-Fracture Conductivities in the Barnett Shale. *SPE Production & Operations*, **29**(3). Https://doi.org/10.2118/163839-PA.

Zoback, M. D. 2010. *Reservoir Geomechanics*. Cambridge, United Kingdom: Cambridge University Press.

# APPENDIX A - EXPERIMENTAL SETUP

## A.1 Triaxial Cell Assembly

1. Make sure the hydraulic lines passing through the piston cylinders are clean by injecting soap, tap water and then deionized water. This procedure is repeated until the output water conductivity matches or is close to the injected deionized water.

2. Apply vacuum grease to the seals where the O-rings are located to ensure the proper pressure sealing.

3. Apply vacuum grease to the upper and lower pistons in the area that will be in contact with the rubber sleeve to ensure proper sealing.

4. Mark the direction of the S-wave polarization in the outer part of the cell and place the propped fracture sample on the lower piston, with the fracture perpendicular to the direction of S-wave polarization.

5. Case the sample with the rubber sleeve.

6. Close the nuts in the lower section of the cell. At this stage, the sample is in the cell.

7. Measure the remaining length in the cell and accordingly adjust the length of the axial piston to be slightly longer (5-10 mm) than the measured length.

8. Set up the triaxial cell and align the upper part of the piston to the marked direction of the S-wave propagation. Then, tighten the nuts for the upper section.

9. Pump mineral oil into the upper section of the cell and then to the lower section. While pumping oil in the lower section, apply vacuum pressure to the pore pressure ports to remove any air of the system.

10. Move the cell to the temperature controlled chamber and connect the lines. The lower chamber is connected to the cell or radial pressure pump and the upper chamber is connected to the axial pressure pump.

11. The chamber is kept closed. Apply the initial axial pressure of 67 psi and confining pressure of 50 psi and maintain them until the temperature in the chamber stabilizes. This is indicated when the fluid volume of the axial and confining pumps is no longer changing due to the oil expansion from temperature increase.

12. Before connecting the cell to the pore pressure lines, push air through these lines to remove any unwanted fluids.

13. Connect the inner pore pressure line with valve V8 and the outlet pore pressure line with valve V11 and apply vacuum through the sample for 24 hours. The vacuum pump is connected through V15, and vacuum is applied from V7 to V15.

14. Vacuum the fluid in the pistons connected to the injection pumps through V4 and V15 for further degassing. Refer to Figure 3.20 for further clarification on the valve location. V4 is closed and V5 is opened. The system is saturated by pumping fluid at very low rate 2 ml/min fluid from the injection pump, while still applying vacuum through V15. This process is stopped after 100 ml of fluid is pumped.

15. Flow deionized water the system to remove the syrup used to place the proppant in the fracture until the conductivity of the effluent fluid matches or is close to the injected deionized water. Close V11 and start the saturation of the sample by applying pore pressure using the inlet pump.

16. Once the volume change in the system is negligible at each pressure step, increase the pressure by maintaining the effective stress constant throughout the process.

17. Further test steps can now be started.

# APPENDIX B - TRIAXIAL STRESS TEST CONDITIONS

The axial, confining, and pore pressure values applied during the flow test and fluid sample collection (Table B.1), and the propped fracture conductivity experiments (Table B.2) performed in the triaxial test are presented below.

Table B.1: Triaxial stress test pressure conditions during the flow test and fluid samples collection.

| $\sigma_a(psi)$ | $\sigma_r(psi)$ | $P_a(psi)$ | $P_c(psi)$ | $P_{p-in}(psi)$ | $P_{p-out}(psi)$ | $P_p(psi)$ | $\sigma'_e(psi)$ |
|---|---|---|---|---|---|---|---|
| 50 | 50 | 67 | 50 | 0 | 0 | 0 | 50 |
| 100 | 100 | 133 | 100 | 50 | 50 | 50 | 50 |
| 150 | 150 | 200 | 150 | 50 | 50 | 50 | 100 |
| 210 | 210 | 280 | 210 | 10 | 10 | 10 | 200 |
| 400 | 400 | 533 | 400 | 200 | 200 | 200 | 200 |
| 600 | 600 | 800 | 600 | 200 | 200 | 200 | 400 |
| 900 | 900 | 1200 | 900 | 200 | 200 | 200 | 700 |
| 1200 | 1200 | 1600 | 1200 | 200 | 200 | 200 | 1000 |
| 1700 | 1700 | 2267 | 1700 | 200 | 200 | 200 | 1500 |
| 2200 | 2200 | 2933 | 2200 | 200 | 200 | 200 | 2000 |
| 2700 | 2700 | 3600 | 2700 | 200 | 200 | 200 | 2500 |
| 3200 | 3200 | 4267 | 3200 | 200 | 200 | 200 | 3000 |
| 3700 | 3700 | 4933 | 3700 | 200 | 200 | 200 | 3500 |
| 5700 | 5700 | 7600 | 5700 | 200 | 200 | 200 | 5500 |
| 7500 | 7500 | 10000 | 7500 | 200 | 200 | 200 | 7300 |

Table B.2: Triaxial stress test pressure conditions during the propped fracture conductivity experiment.

| $\sigma_a(psi)$ | $\sigma_r(psi)$ | $P_a(psi)$ | $P_c(psi)$ | $P_{p-in}(psi)$ | $P_{p-out}(psi)$ | $P_p(psi)$ | $\sigma'_e(psi)$ |
|---|---|---|---|---|---|---|---|
| 2200 | 2200 | 2933 | 2200 | 2000 | 2000 | 2000 | 200 |
| 2400 | 2400 | 3200 | 2400 | 2000 | 2000 | 2000 | 400 |
| 2700 | 2700 | 3600 | 2700 | 2000 | 2000 | 2000 | 700 |
| 3000 | 3000 | 4000 | 3000 | 2000 | 2000 | 2000 | 1000 |
| 3500 | 3500 | 4667 | 3500 | 2000 | 2000 | 2000 | 1500 |
| 4000 | 4000 | 5333 | 4000 | 2000 | 2000 | 2000 | 2000 |
| 4500 | 4500 | 6000 | 4500 | 2000 | 2000 | 2000 | 2500 |
| 5000 | 5000 | 6667 | 5000 | 2000 | 2000 | 2000 | 3000 |
| 5500 | 5500 | 7333 | 5500 | 2000 | 2000 | 2000 | 3500 |
| 7500 | 7500 | 10000 | 7500 | 2000 | 2000 | 2000 | 5500 |
| 7500 | 7500 | 10000 | 7500 | 200 | 200 | 200 | 7300 |